FliPASED
WWW.FLIPASED.EU

D3.9 Advanced wing integration and ground test completed

Authors: Fanglin Yu (TUM), Daniel Teubl (TUM), Szabolcs Tóth (SZTAKI), Nicolas Guérin (ONERA), Keith Soal (DLR)

GA number:	815058
Project acronym:	FLIPASED
Project title:	FLIGHT PHASE ADAPTIVE AEROSERVO-ELASTIC AIRCRAFT DESIGN METHODS
Funding Scheme: H2020	**ID:** MG-3-1-2018
Latest version of Annex I:	1.2 released on 13/12/2022
Start date of project: 01/09/2019	**Duration:** 46 Months

Lead Beneficiary for this deliverable:	DLR
Last modified: 30/06/2023	**Status:** Delivered
Due date: 08/05/2023	

Project co-ordinator name and organisation:	Bálint Vanek, SZTAKI
Tel. and email: +36 1 279 6113	vanek@sztaki.hu
Project website:	www.flipased.eu

Dissemination Level		
PU	Public	X
CO	Confidential, only for members of the consortium (including the Commission Services)	

“This document is part of a project that has received funding from the European Union’s Horizon 2020 research and innovation programme under grant agreement No 815058.”

Glossary

ASE	Aeroservoelastic
CAD	Computer-aided Design
CPACS	Common Parametric Aircraft Configuration Schema
DLM	Doublet Lattice Method
FEM	Finite Element Model
SW	Soft-ware
HW	Hard-ware
VV	Verification and Validation
GLA	Gust Load Alleviation
MLA	Manoeuvre Load Alleviation
MDO	Multidisciplinary Design Optimization
MLA	Manoeuvre Load Alleviation
PID	Proportional-Integral-Derivative
RCE	Remote Component Environment
HIL	Hardvare-in-the-loop
FCC	Flight Control Computer
TCL	Tool Command Language
GVT	Ground Vibration Test
EDBC	ICAO code of Cochstedt Airport
GCS	Ground Control Station
EDL	Engineering Data Link
FE	Finite Element
PSM	Phase Separation Method
UNV	Universal File Dataset Format

Table of contents

List of Figures

1 Executive Summary

This document contains results from the advanced wing ground testing. Due to the crash of the T-FLEX aircraft and subsequent rebuild of the P-FLEX aircraft, the advanced wing became the re-equipped -1 wing. The goal of this wing was to test the active flutter controllers in closed loop at the simulated flutter critical speed. In preparation for these tests the direct drive actuator was load tested to investigate the positional accuracy and temperature effects. Static tests were first simulated and then conducted on the wing to confirm the design goal. The remote control system was range tested and the telemetry system was also tested and improved. Finally a Ground Vibration Test (GVT) was performed to identify the dynamic characteristics of the structure. These results were used to update the flutter calculations as well as the model used by the active flutter controllers.

2 Direct Drive

2.1 Lessons learned during operation

To analyze the performance of the Direct Drive during flutter control, logparts were used which created loads close to, or above, the flutter speed. This is due to higher loads on the Direct Drive at higher speeds. Position accuracy and errors were calculated as the difference between commanded and measured position in each measurement point regardless of the frequency or shape of the signals. The Direct Drive's controller's temperature was also monitored, due to a performance reduction around 60 ℃, which could effect the position following. As can be seen in Table 1, the air cooling was sufficient.

Logpart	DD	Avg. Accuracy	Max Pos. Err.	Max defl.	Velocity	Temp
		[+-deg]	[+-deg]	[+-deg]	[m/s]	[℃]
1	Left	0.1971	2.1843	4.5	56-62	23.5
1	Right	0.2186	2.5681	5.6	56-62	19
2	Left	0.5027	2.8243	4.9	49-56	20.5
2	Right	0.4726	2.7709	6.6	49-56	15.8
3	Left	0.448	4.5235	7.5	54-60	20.5
3	Right	0.4087	3.9741	6.9	54-60	15.8
4	Left	0.2319	2.566	8.5	49-60	17.5
4	Right	0.1847	3.2368	8.5	49-60	12.5
5	Left	0.1879	3.8462	4.5	42-52	23.5
5	Right	0.1592	3.0943	4.1	42-52	17.5

Table 1: Direct Drive performance during flight tests

In conclusion the Direct Drive demonstrated sufficient performance during flutter control.

3 Static and Taxi Test

3.1 Static test of -1 wing

This chapter presents the airworthiness test performed on the -1 wing to verify its capacity to withstand the design load of 4 g. It encompasses an explanation of the arrangements made for both the hardware and simulation aspects, along with specific information about the execution of the test and its outcomes.

3.1.1 Preparation

During the airworthiness test, the wing's entire surface cannot be distributedly loaded as it would be in flight. Instead, sandbags are strategically positioned at specific locations on the wing to simulate the distributed load conditions experienced during flight. To ensure an effective distribution of the load and account for the wing skin's load-bearing capacity, the load application sections are chosen to align with the rib locations. Consequently, there are seven sections on each side of the wing, and there is no additional space available to accommodate extra sandbags. To determine the optimal weight of sandbags needed to accurately replicate the flight configuration, a simulation study must be conducted. The simulation model utilized for this purpose is illustrated in Figure 1.

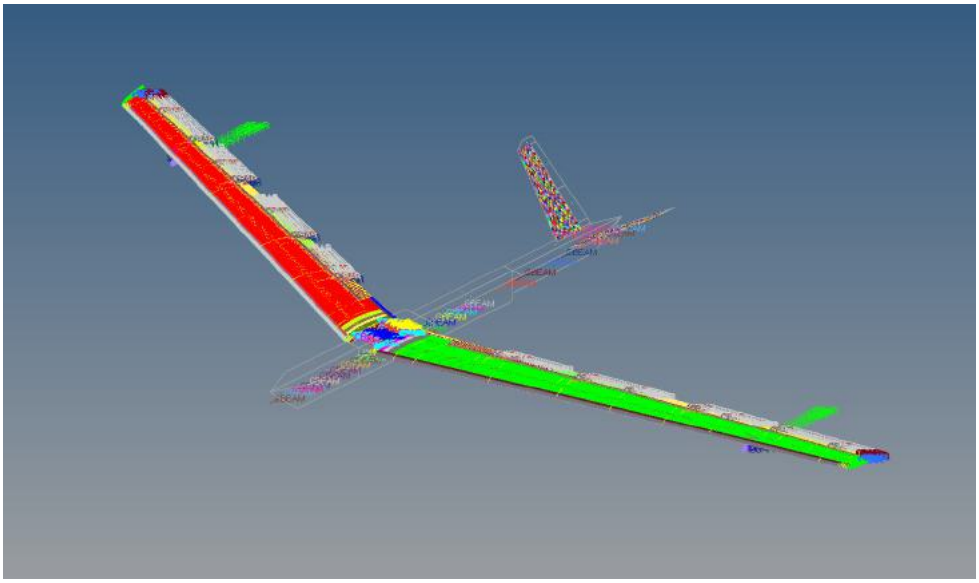

Figure 1: -1 wing FEM in trim analysis.

The first step of the simulation study involves performing a trim analysis to ascertain the aerodynamic loads acting on the aircraft and determine the flight shape of the wing. This trim analysis relies on the Nastran solution 144. The displacement obtained from the trim analysis is subsequently utilized as constraints in the static analysis to calculate the section loads (Figure 2).

The resulting loads and positions for each section are presented in Table 2. The sandbags are prepared according to the specified weights provided in Table 2.

3.1.2 Conduct

In order to ensure stability during the testing process, a wing stand was constructed and securely fastened to the ground. To replicate partial lift, the wing was positioned upside down, utilizing the force

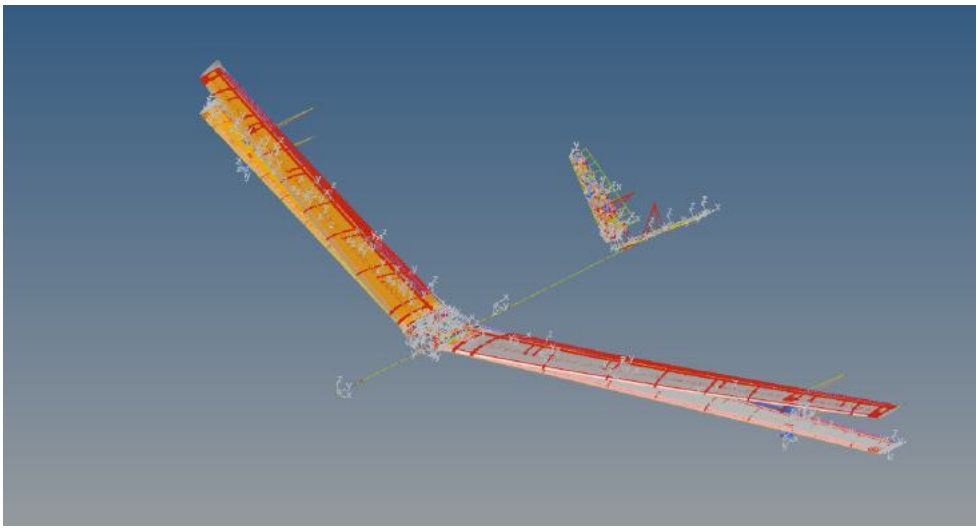

Figure 2: -1 wing static analysis.

Table 2: Sectional loads on -1 wing.

Section	Section force (N)	Sandbag weights (kg)	Distance (m)
1	86,20	8,79	0.5
2	164,34	16,75	0,87
3	112,15	11,43	1,39
4	98,79	10,07	1,79
5	67,57	6,89	2,20
6	46,96	4,79	2,54
7	23,97	2,44	3,38

of gravity. Instead of suspending the sandbags from the wing, they were placed directly on the wing surface. This approach increased the contact area and reduced localized pressure on the fragile -1 wing skin, addressing concerns regarding potential damage. Given the high flexibility of the -1 wing, subjecting it to a 4g load could lead to substantial deflection, causing the sandbags to slide off. In a worst-case scenario, the wing could flip over and suffer damage. To prevent such issues, a rubber mat was affixed to the wing and positioned beneath the sandbags. The entire setup can be seen in Figure 3.

Before applying the load to the wing, the distance between the wing tip and the ground was measured using a tape measure. Subsequently, the wing was loaded progressively from the inner section towards the outer section. Once the wing was fully loaded with a 4g force, the distance between the wing tip and the ground was measured again.

3.1.3 Results

The conclusion drawn from the airworthiness test conducted on the -1 wing is that the wing is capable of withstanding the specified load. According to the simulation results, the deflection observed under the 4g load is measured to be 0.32 m. However, when measured using a tape, the actual deflection is recorded as 0.24 m. It is important to note that the measurement of deflection with a tape may introduce some deviation in the results. Therefore, it is possible that part of the difference between the simulated and measured deflection values can be attributed to the measurement method itself.

Figure 3: -1 wing airworthiness test.

3.2 Remote Control System range test

3.2.1 Integrated system at EDBC

There are two types of range-test conducted with the P-flex aircraft.

- Stationary test
- Taxi test

During the stationary test, the aircraft is in an elevated position about 1.5-2m from the ground, in a fully assembled state and most subsystems are functional. The RC controllers are with one or two operators, and they are driving away from the aircraft. Although the aircraft orientation is fixed relative to the remote controller, it would be possible to change the aircraft orientation as well.

It would be possible to map out different orientations of the aircraft relative to the remote controllers, and module it via different distances. However, this does not give a real implication of the maximum possible range of a given system, it can give a realistic safe distance.

With our tests, the relative orientation of the aircraft was fixed into a not-ideal configuration, and we reached 700-800 metes with each RC system. These reseults meet the system requirements for the operational boundaries of the aircraft.

During normal taxi tests, the pilots drive the aircraft around and away from themselves, to validate the control ability of the system on the ground with different speed conditions. Conducting range-test while taxing, the pilots drive the aircraft slowly away from themselves in a controlled manner, normally up to 200-300 meters. The aim is to cover at least 2-3 times the normal takeoff distance on the ground, and demonstrate full control and ”acceptable” radio reception values during both directions and turning.

During our taxi range test, the RC system successfully passed the above-mentioned taxi test.

Furthermore, the backup remote control system reception characteristics were checked after each flight, to have a better understanding of the normal behaviour of the system. Figure 4 and 5 show the different measurement point distributions over distance.

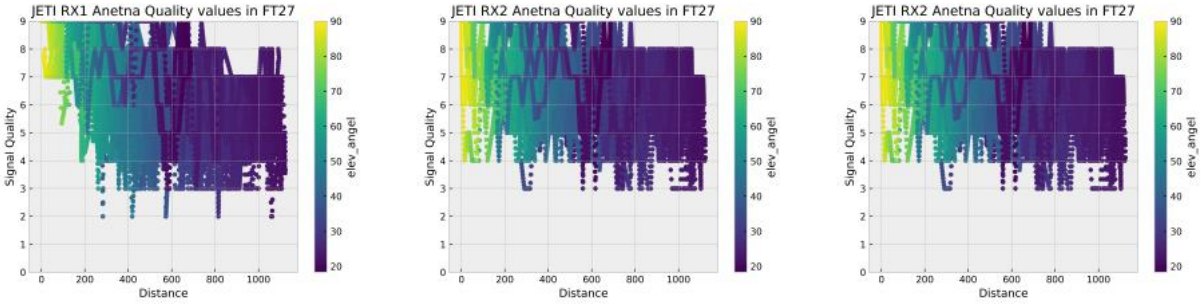

(a) RX1 (b) RX2 (c) RX3

Figure 4: JETI Antenna values by internal indicator, logged on the backup system.

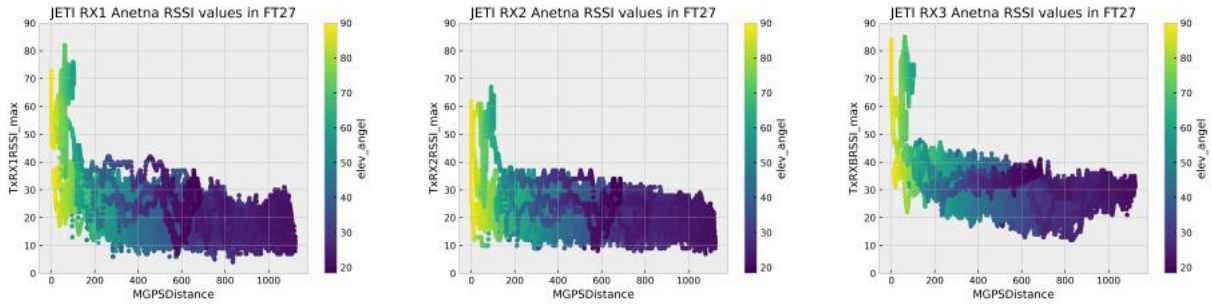

(a) RX1 (b) RX2 (c) RX3

Figure 5: JETI RSSI values logged on the backup system.

3.3 Telemetry system range test

As mentioned in [1], the telemetry system received major changes during the rebuild. As with any RC aircraft, it needed to be tuned and changed during operation, to reach an acceptable quality.

However, during the first flight-test campaign, significantly bad reception and data quality was experienced with both telemetry links. By changing the internal configuration of the 868Mhz module, and applying an additional power supply to it on the GCS side, the system behaviour became stable and usable on the 868Mhz data link.

Until the end of the first campaign, it was possible to reach data link quality similar to that observed during initial telemetry range testing with the clean mockup configuration [3].

After the first campaign, the 433 Mhz telemetry system was replaced by an 868 Mhz system. To avoid interference, the MisiPlanner(MP) telemetry module was now located under the belly of the aft of the landing gear. With that, potential interference between the three 868 MHz radio systems is minimized. The main reasoning behind the change, and location:

- The 433Mhz telemetry setup had slightly worse reception than in the previous configuration. The quality was highly dependent on the relative orientation of the plate to the Ground Control Station(GCS).
- The 868Mhz had acceptable reception, independent of the orientation of the plane

(a) 868Mhz telemetry module location for the MP

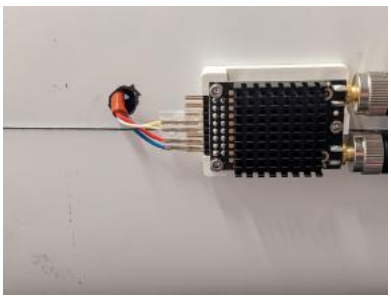

(b) 6 pin layout cabling for the telemetry module

Furthermore, the following changes were made during the flight test campaign in May 2023:

- Dedicated power supply modes were fabricated from a 5V power supply unit for the telemetry modules in the GCS. It was found that the USB cable extenders were not supplying enough power to the telemetry modules in the GCS, although both extension cables had dedicated power supply modules.
- The channel, frequency and communication speed were changed on each modem pair.
  - The usable frequencies were put to the two halves of the available spectrum, to eliminate possible interference.
  - Data communication speed base-frequencies were removed to the bare minimum needed to support the data stream. This normally helps eliminate package and data errors.
- The frequency and channel layout of the long-range communication system for the pilots were changed. It was found that they were interfering with each other and with the telemetry system as well.

During the final flight week, an unidentified error in the EDL telemetry stream was however still observed. At seemingly random times, the datastream stopped for 30 seconds. It was possible to identify, that the connection loss has nothing to do with orientation, distance, power supply or radio interference, so likely it is a software-related error. Since it was not possible to reliably reproduce the data loss, it was also not possible to fix the problem.

4 GVT

4.1 Introduction

Ground Vibration Testing (GVT) is used to evaluate the structural dynamic behaviour of aircraft. During a GVT, the aircraft is suspended from bungees and subjected to controlled vibrations generated by electrodynamic shakers. The aircraft response to these vibrations can be used to identify resonance frequencies, damping ratios and mode shapes on ground before first flight of a prototype. The results are used to validate and update the Finite Element (FE) model for further aeroelastic simulations. The GVT is an important part of the development process for new aircraft and is performed at various stages of the design.

4.2 Test Overview

The GVT of the FLIPASED aircraft was conducted by a team from ONERA and DLR at the DLR Institute of Aeroelasticity in Göttingen. The aircraft was suspended from soft bungee cords as shown in figure 7 in order to separate the elastic modes from the rigid body modes. The aircraft was then instrumented with approximately 150 lightweight accelerometers including uni-axial and tri-axial sensors. These provide the benefit of not mass loading the structure, while maintaining high accuracy even at low frequencies. Several electro-dynamic shakers were used to excite the structure with different custom designed input signals. A specialized test team consisting of a team leader, and engineers and computer scientists for data acquisition, signal processing, modal analysis and modal model correlation ensure high quality results, a plan of the work stations is depicted in figure 8.

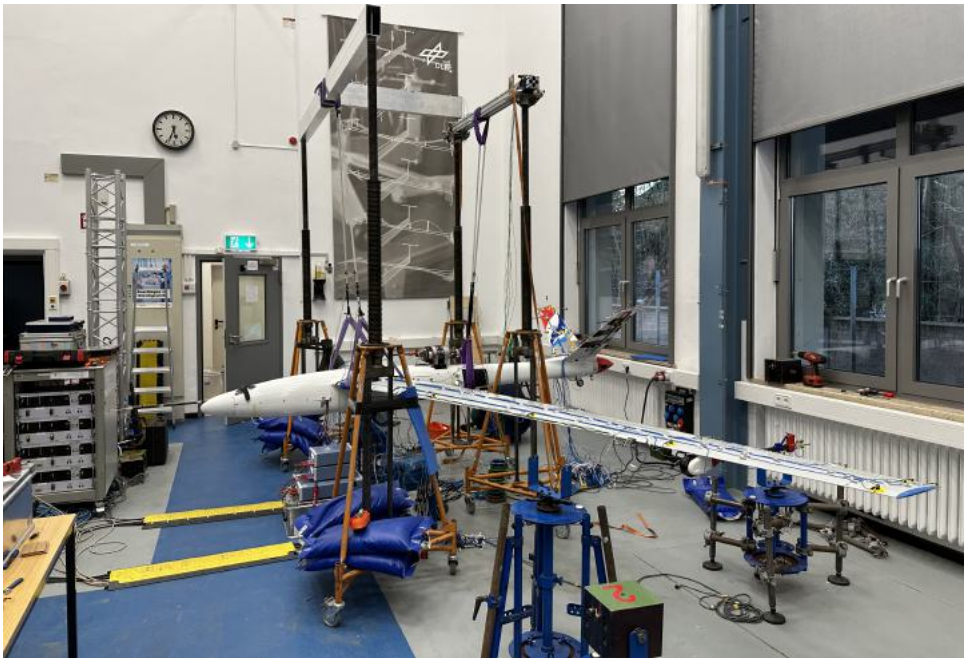

Figure 7: FLIPASED UAV suspended from bungees in lab.

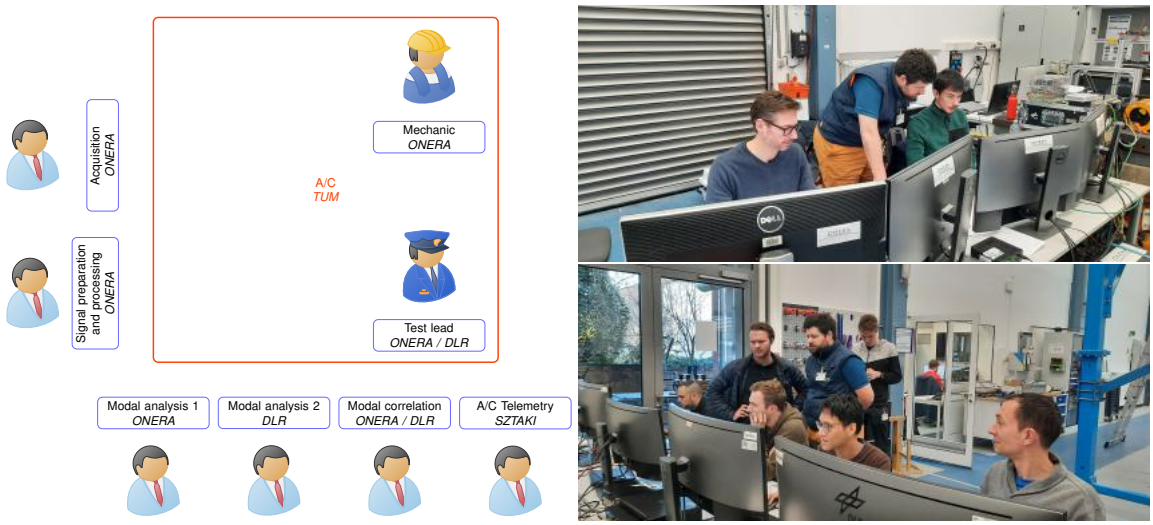

(a) Schematic organization with roles and *partner*.

(b) Pictures made during the GVT.

Figure 8: Test work stations.

4.3 Test Plan

The GVT described in this document is the second performed on this aircraft. The first test was carried out during the EU-FLEXOP project by DLR on the T-FLEX demonstrator [2]. The current GVT has been dedicated to the thorough analysis of the -1 wing set of the aircraft, as well as the new P-FLEX airframe given the crash of the T-FLEX just weeks before the initial planned GVT date. Given the expected unstable behavior of the aircraft equipped with this wing set, an extensive test plan was performed on the aircraft.

Three structural configurations were tested during this GVT campaign

- C1a : aircraft with flutter stopper masses in aft position (flutter-prone design point). This is the main configuration that was tested
- C1b : aircraft with flutter stopper masses in forward position (flutter-free design point). Three excitation runs were performed, all on the wings
- C1d : aircraft with flutter stopper rods removed. This configuration was not initially planned. It was performed as a fast verification point for the test instrumentation with a simpler aircraft structure.

4.4 Experimental setup

4.4.1 Aircraft configuration

During the test, the aircraft weighed 70 kg which included 10 kg of fuel load. During measurements, the canopy was closed, and additional masses were fitted onto the airframe in order to account for missing components that would be present during the flight test campaign. At the beginning of the test, all control surfaces (Flaps 1 to 3 and ailerons 4) on both sides of the aircraft were powered on and flight ready. The ailerons were subsequently powered off due to high electromagnetic noise levels.

4.4.2 Measurement setup

The aircraft instrumentation setup is illustrated in figure 9. The list of sensors and nomenclature used

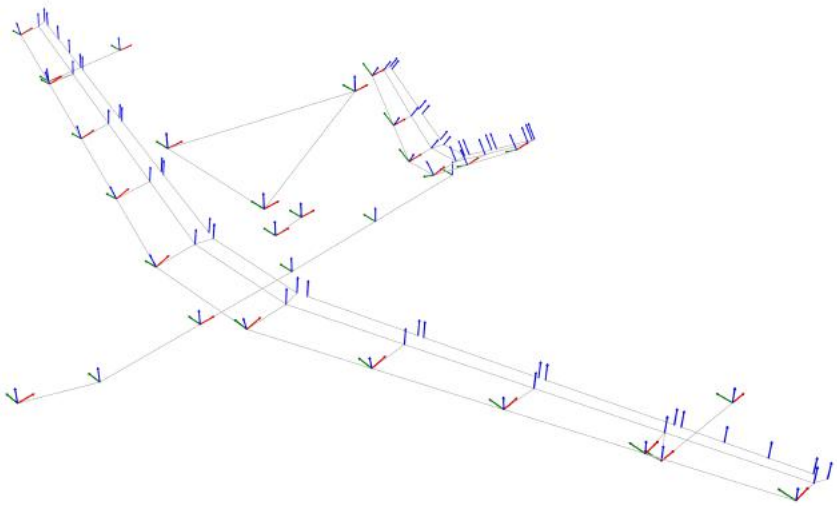

Figure 9: Aircraft sensor locations and directions. Local X (→), Y (→), Z (→) sensor directions.

is detailed in table 3. The aircraft was equipped with sensors on all main structural components and control surfaces, including wings, flutter stopper rods, v-tail, engine, fuselage and aero boom. The suspension bungees and supporting structure (sensors not represented or listed) were instrumented as well, which proved useful during the correlation of the modal data. The only massive component that was not instrumented is the landing gear which was considered relatively stiff. All sensors were positioned tangentially to the local surface.

The measurement setup was composed of a mixed instrumentation between ONERA and DLR hardware :

- ONERA: Wing, flutter stopper assemblies, and V-tail tri-axis acelerometers, shakers and related hardware (cabling, acquisition system, power amplifiers)
- DLR: Nose boom, fuselage and engine tri-axis sensors, all uni-axis sensors (very light sensors), related hardware (cabling, acquisition system)

Sztaki provided a ground control station with telemetry capabilities to control the aircraft state and record data using internal sensors for other partners.

4.4.3 Excitation points

5 excitation points were exploited on this aircraft :

- Inner wing Z excitation
- Inner wing X excitation

Component	Abbreviation	Number	Sensors	Channels
Left Wing	WNGL	01	6 XYZ + 7 Z	38
Left Aileron 1	AILL1	03	2 Z	
Left Aileron 2	AILL2	05	2 Z	
Left Aileron 3	AILL3	07	2 Z	
Left Aileron 4	AILL4	09	4 Z	
Left Direct Drive	DDL	17	1 XYZ	
Right Wing	WNGR	02	6 XYZ + 7 Z	38
Right Aileron 1	AILR1	04	2 Z	
Right Aileron 2	AILR2	06	2 Z	
Right Aileron 3	AILR3	08	2 Z	
Right Aileron 4	AILR4	10	4 Z	
Right Direct Drive	DDR	18	1 XYZ	
Left Stabilizer	VTLL	11	3 XYZ + 5Z	18
Left Elevator 1	ELEL1	13	2 Z	
Left Elevator 2	ELEL2	15	2 Z	
Right Stabilizer	VTLR	12	3 XYZ + 5Z	18
Right Elevator 1	ELER1	14	2 Z	
Right Elevator 2	ELER2	16	2 Z	
Fuselage	FUSE	19	1 XYZ + 4YZ	35
Engine	ENG	20	2 XYZ	
Nose Boom	NBOOM	21	1 XYZ	
Driving Points	DP	80	2 X + 1Y + 3 Z	
Suspension Device	SUSP	30	3 XYZ	

Table 3: List of sensors per aircraft structural components.

- Fuselage Y excitation
- Fuselage Z excitation

All excitation points were glued onto the aircraft structure, via interface parts. The wing X excitation points were glued through a 3D-printed conformal interface part.

4.4.4 Suspension

The aircraft was suspended using three bungees and slings, two fitted on the wing roots on each side of the fuselage, and one under the fuselage close to a fuselage web location. The suspension was equipped with tri-axis accelerometers, to avoid any miss interpretation between the suspension chord modes and the aircraft flexible modes. The suspension gantry was equipped with accelerometers as well, for surveillance purposes, and weighted to ensure its stability.

4.4.5 Excitation strategy

Most of the analyses were performed using the *Phase Separation Method* (PSM) under random or swept sine excitations.

(a) Rearview, Y direction excitation point.

(b) Side view, Z direction excitation point.

Figure 10: Fuselage excitation points, equipped with a 47 N ONERA shaker along with its sensing elements.

(a) Z direction.

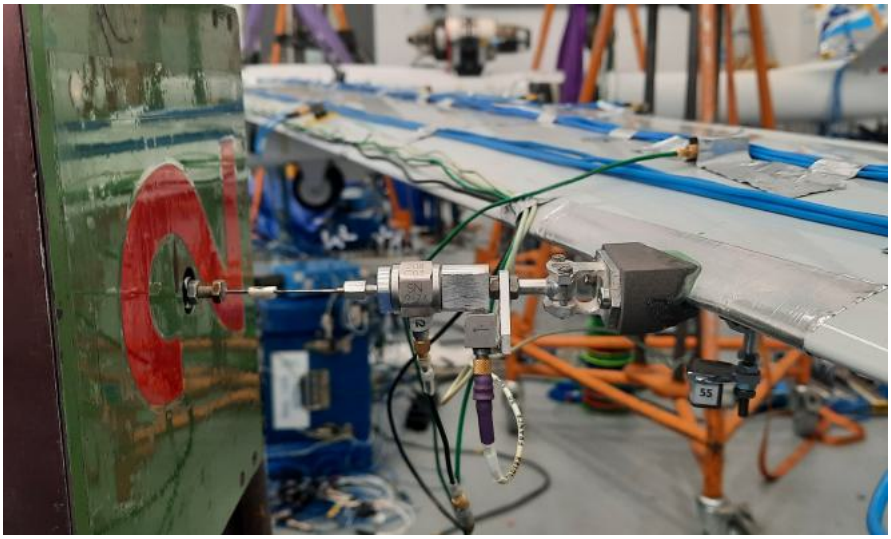

(b) X direction.

Figure 11: Wing excitation points.

4.5 Test Results

4.5.1 General comments

Rigid body modes of the aircraft identified during this campaign were not extensively identified. While the frequency and damping factors may be well identified, the generalized masses for these modes must be taken with precaution. This can be explained by the usage of lightweight sensors during this GVT to reduce perturbation of the aircraft structural behavior by the additional sensor masses. In fact, these sensors show poor sensitivity at low frequencies for technological reasons, leading to ill-identified

generalized masses. Finally, the rigid body roll mode could not be identified during this test, due to its very low frequency.

Some flexible mode modal masses also suffer from poor identification, in particular, the one of mode n°12 `flutterstop_bend_y-a` identified in C1b. While there is no obvious clue as to why this mode suffers from poor identification, the fact that it is a flutter stopper mode could indicate and influence of the flutter mass inside the flutter stopper rod. In fact there is some freeplay between the mass and the rod, potentially resulting in non linear phenomena such as friction and impacts.

As a final comment, the frequency, and therefore the damping and modal masses of a few modes, in particular the in-plane or so-called scissor mode, was without surprise difficult to ascertain. This particular mode stems from the flexibility of the linkage between the aircraft fuselage and wings. On this aircraft, this linkage is bolted. Such configurations are often prone to non-linear behavior due to the high sensitivity of local sliding or even separation between initially in contact components. This leads to complex structural behavior on which linear modal identification reaches its limits. This is generally true for most linkage related flexibilities. As an example, figure 12 displays the frequency response functions of the wing X direction accelerometers, in C1a, during three fuselage Y excitation runs at increasing excitation force levels. By comparing the frequency response function trends around

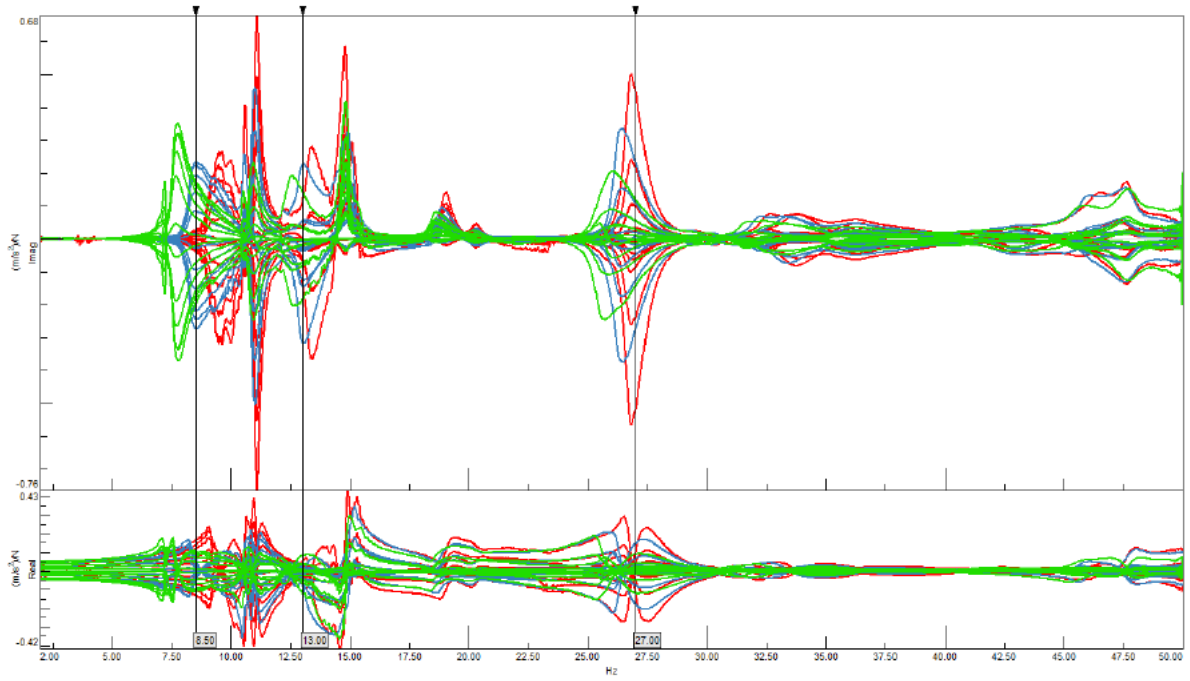

Figure 12: Frequency response functions of wing X direction accelerometer responses under fuselage Y excitation. Force voltage 0.25 V (—), 0.5 V (—), 1 V (—).

8.5 Hz, 13 Hz and 27 Hz, one can observe a frequency shift of the response amplifications towards lower frequencies, as well as variation of these amplifications. These observations are easily attributed to sliding phenomena in the aircraft structure. Given the identified modal data in table 4, one can link these nonlinear behavior with the scissor/inplane mode (mode shape in figure B.8), the V-tail rock mode (mode shape in figure B.12) and the first lateral fuselage bending (mode shape in figure B.21).

4.5.2 C1a

C1a modal results are gathered in table 4. For detailed information, please refer to the UNV file stored in appendix 2. The in-phase part (with respect to the normalization point) of the C1a identified mode shapes are plotted in section 2.

N°	Name	Damped Freq. [Hz]	Damping [%]	Gen. Mass [kg.m^2]	Norm. Point	MIF
1	ac_y_trans-S	0.867	0.83	284.99	8001905+Y	891
2	ac_pitch-S	0.888	5.14	12.57	2100101+Z	833
3	ac_x_trans-S	1.009	1.69	72.83	8000204+X	740
4	ac_z_trans-S	1.143	4.61	22.77	8001905+Z	928
5	ac_yaw-A	1.797	0.77	44.86	0100701+X	951
6	2n_wing_bend-s	2.938	1.10	5.08	0100704+Z	967
7	3n_wing_bend-a	7.220	0.79	3.24	0200704+Z	986
8	1n_wing_inplane-a	8.491	1.83	32.43	8001905+Y	898
9	wing_tors-s	10.744	0.95	0.65	0100405+Z	907
10	wing_tors-a	11.155	1.07	0.69	0200405+Z	930
11	4n_bending-s	12.023	0.72	3.12	0100704+Z	907
12	vtail_rock-a	12.501	3.36	0.64	1100304+Z	985
13	2n_wing_inplane-s	14.846	1.19	2.34	0100405+Z	960
14	flutterstop_right_y	16.702	2.97	0.44	0200405+Y	949
15	mass_lat-a	18.617	1.08	1.83	0200405+Y	847
16	mass_lat-s	19.298	1.41	6.85	0200405+Y	860
17	5n_wing_bend-a	20.383	1.78	1.57	0100704+Z	867
18	flutterstop_left_y	22.213	4.01	0.47	0100405+Y	987
19	2n_fus_vert-s	23.986	1.25	1.21	1200304+Z	972
20	6n_wing_bend-s	25.860	1.82	0.97	1200304+Z	922
21	2n_fus_lat-a	26.266	1.42	1.76	2100101+Y	902
22	2n_tail_bend-s	27.218	0.90	1.18	2100101+Z	779
23	7n_wing_bend-A	29.431	1.37	2.09	2100101+Y	888
24	2n_tail_bend-s?	29.466	1.10	1.40	2100101+Z	786
25	engine_x-s	32.172	0.74	2.86	2100101+Y	889
26	7n_wing_bend-A???	32.864	1.15	0.92	2100101+Y	863
27	2nd_wing_tors-a	33.350	3.45	0.74	2100101+Y	833

Table 4: Modal property table for FLIPASED – C1a.

4.5.3 C1b

C1a modal results are gathered in table 5. For detailed information, please refer to the UNV file stored in appendix 3. The in-phase part (with respect to the normalization point) of the C1b identified mode shapes are plotted in section 3.

4.5.4 C1d

C1a modal results are gathered in table 6. For detailed information, please refer to the UNV file stored in appendix 4. The in-phase part (with respect to the normalization point) of the C1d identified mode shapes are plotted in section 4.

N°	Name	Damped Freq. [Hz]	Damping [%]	Gen. Mass [kg.m^2]	Norm. Point	MIF
1	ac_pitch-s	1.309	4.78	25.89	1900501+Z	908
2	2n_wing_bend-s	2.952	1.35	4.86	0200704+Z	970
3	3n_wing_bend-a	7.327	0.76	3.07	0100704+Z	981
4	1n_wing_inplane-a	10.913	2.59	2.92	1200304+Z	985
5	4n_wing_bend-s	12.042	0.94	1.98	0100704+Z	955
6	2n_wing_torsion-s	12.756	0.71	0.57	0200405+Z	970
7	1n_wing_torsion-a	13.491	1.58	1.66	1100304+Z	844
8	vtail_rock-a	14.065	1.98	0.90	0200405+Z	632
9	2n_wing_inplane-s	16.005	0.61	4.46	0200701+X	966
10	5n_wing_bend-a	20.145	1.87	1.06	0200704+Z	977
11	2n_fus_vert-s	23.908	1.14	2.66	1200104+Z	953
12	flutterstop_bend_y-a	25.037	1.07	1148.28	0200405+Z	489
13	flutterstop_bend_y-s	25.396	1.24	3.83	1100304+Z	720
14	2n_tail_bend-s	25.984	1.67	1.44	1600304+Z	915
15	2n_fus_lat-a	26.686	1.60	0.57	2100101+Y	940
16	boom_bend_z-s	29.160	1.63	0.33	2100101+Z	761
17	boom_bend_y-a	30.219	1.41	0.08	2100101+Y	970
18	boom_bend_yz-a	32.469	1.55	0.12	2100101+Z	940
19	7n_wing_bend-a	35.580	2.48	11.08	0100405+Z	884
20	flutterstop_bend_z-a	39.249	3.36	0.30	0700304+Z	848
21	flutterstop_bend_z-s	42.313	2.61	2.41	0200405+Z	859

Table 5: Modal property table for FLIPASED – C1b.

N°	Name	Damped Freq. [Hz]	Damping [%]	Gen. Mass [kg.m^2]	Norm. Point	MIF
1	ac_x_trans-S	1.028	1.50	14.32	0100201+X	910
2	ac_pitch-S	1.353	6.77	20.70	1200101+Z	966
3	2n_wing_bend-s	3.081	1.18	4.89	1000704+Z	985
4	3n_wing_bend-a	7.491	0.77	3.00	1000704+Z	991
5	1n_wing_inplane-a	10.721	4.18	17.42	1100201+Z	962
6	4n_wing_bend-s	12.097	0.65	12.04	8000203+Z	928
7	vtail_rock-a	13.747	3.28	0.82	1200304+Z	991
8	2n_wing_inplane-s	15.369	0.82	16.09	0200401+X	981
9	5n_wing_bend-a	20.311	1.73	5.93	0200701+Z	831
10	2n_wing_torsion-s	22.808	1.03	3.08	0100702+Z	892
11	1n_wing_torsion-a	23.601	1.28	2.71	1000404+Z	960
12	vtail_bend-s	25.087	1.56	1.32	1100301+Z	954
13	2n_fus_lat-a	27.418	1.76	1.12	2100101+Y	862
14	6n_wing_bend-s	27.940	1.56	14.61	1600204+Z	816
15	2n_fus_vert_s	29.559	1.66	13.70	0100701+Z	742
16	boom_bend_lat-a	30.481	1.02	0.19	2100101+Y	953
17	boom_bend_vert-s	32.291	2.00	0.33	2100101+Z	870
18	7n_wing_bend-a	33.111	1.51	36.98	1000404+Z	596
19	3n_wing_torsion-a	34.959	1.10	2.89	3000101+X	535

Table 6: Modal property table for FLIPASED – C1d.

4.5.5 Comparison between configurations

Given the specific design point of the -1 wing set of this aircraft, with flutter masses designed to allow transitioning from flutter–prone to flutter–free behavior, it was of utmost importance to assess the actual effect of these masses on the aircraft behavior.

A list of common mode shapes identified in the three structural configurations mentioned in 4.3 was assembled and their frequency and damping properties were compared. As a recall, only configuration C1a was extensively analysed, and in C1b and C1d only wing excitations were performed.

Figure 13 depicts the qualitative orderding of modal families in each configuration. Unsurprisingly, some

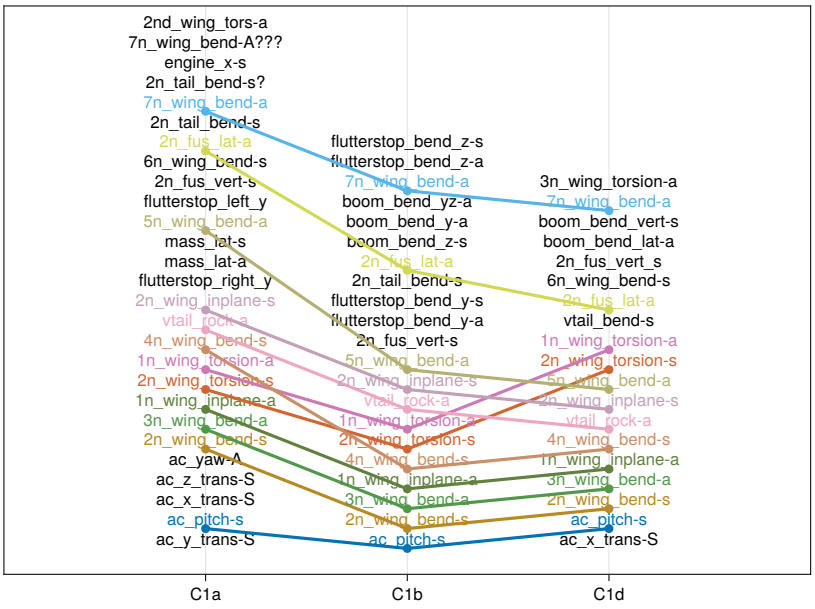

Figure 13: Frequency organization of modal families identified in C1a, C1b and C1d.

modes identified in C1a are not found in C1b and C1d due to the lower amount of excitations exploited. However, the main observation that can be formulated here is the effect of the flutter stopper assemblies on the torsion modes. In fact, in C1b — flutter stopper masses moved in front position, closer to the torsion line — a clear reordering of modes is obtained, with the first symmetric and antisymmetric torsions moving above the 4 node wing bending mode. In the same conditions, bending modes seem to be very little impacted, as designed, by the mass position modification.

A quantitative comparison of modal frequencies (respectively dampings) is performed in figure 14 (respectively figure 15). A clear trend can be observed in terms of frequencies, where almost only the first torsion modes are influenced by the position, or even the presence, of the flutter stopper devices. Two other modes are influenced by the flutter stopper settings. First, the pitch mode, which is shifted due to the variation in overall mass distribution, which in turns modifies the pitch inertia. Second, the inplane antisymmetric bending mode or so-called scissor mode. This mode is probably affected by the flutter stopper setting because it shows non-planar movement close to a torsion, as shown in picture B.8. There is also a much larger effect of the flutter stopper removal than that of the flutter stopper mass position, meaning that the flutter stopper design, might be optimized to reduce the mass of the flutter stopper deviced to obtain a better flutter mass weight/flutter stopper weight. In terms of damping, there is no obivous variation worth commenting.

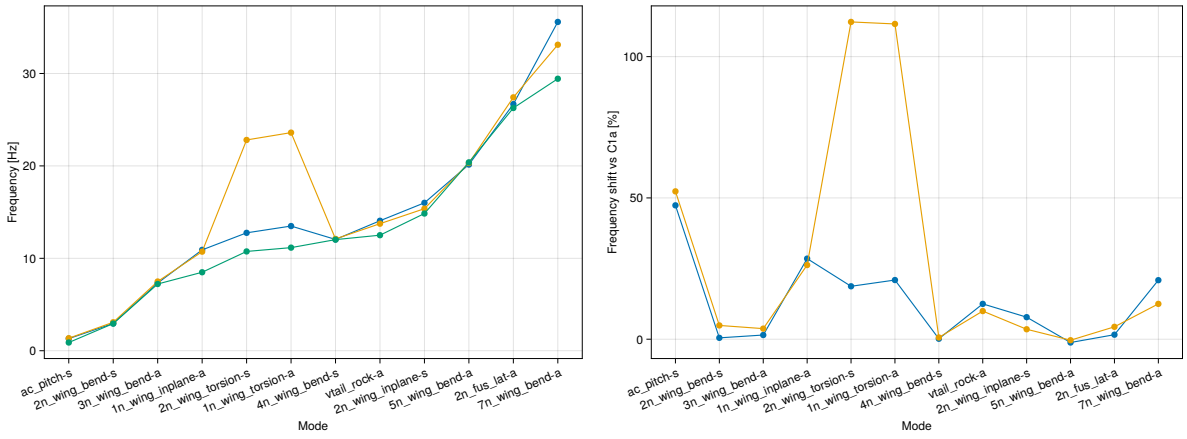

(a) Absolute values

(b) Relative shift w.r.t C1a.

Figure 14: Comparison of frequency properties of common modes identified in C1a (●●●), C1b (●●●) and C1d (●●●).

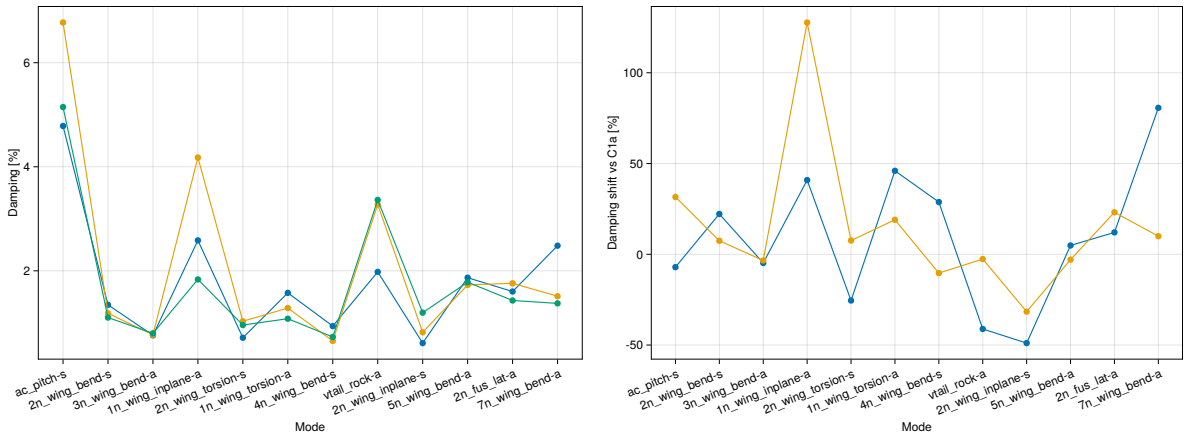

(a) Absolute values

(b) Relative shift w.r.t C1a.

Figure 15: Comparison of damping properties of common modes identified in C1a (●●●), C1b (●●●) and C1d (●●●).

5 Summary

5.1 GVT objectives

This GVT campagin reached its main objective : characterizing the structural dynamic behavior of the P-FLEX aircraft. An analysis was carried out in the main configuration of interest, the flutter–prone configuration, as well as two secondary confgurations designed to be flutter–free. This campaign allowed to charaterize the efficiency of the flutter stopper design to act on the dyanmic properties of the aircraft. A susbsequent step of this analysis to understand the behavior of the aircraft in flight, is to use the modal identification data from the GVT to perform a flutter simulation. This work is detailed in deliverable [3] of the FLIPASED project.

5.2 Lessons learned

While this GVT in itself was not of an extreme complexity, some lessons have been learned in terms of testing both very light and active structures.

5.2.1 Light structures

Testing light structures is relatively complex on its own. In fact, these structures are easily influenced by the surrounding measurement or excitation instrumentation. The use of very light sensors, in order to reduce the intrusivity of the sensor masses lead to the use of non TEDS sensors, which in turn lead to the late detection of instrumentation mis-cabling. It could prove interesting to possess a TEDS capability for very light sensors.

5.2.2 Expectation bias

The expected dangerous behavior of the aircraft with the tested wing set, made the test team expect some exceptional phenomena, which mislead us at some points during the test campaing. It should be noted that despite the aspect ratio of this aircraft and its *exotic* features, it still possesses quite a standard behavior. The assumption of exotism of this aircraft lead us to mis-identify an instrumentation problem, which generated slight delays and more important some additional data management tasks.

5.2.3 Time constraint bias

Every structural configuration should be excited with several excitation points. Due to time constraints, C1b and C1d were only little explored, leaving some questions on hold. A very minimal and common set of excitations to be performed in each structural configuration should be defined, to make structural configuration comparison more straighforward and comprehensive.

5.2.4 Active control systems

The presence of very active systems on board the aircraft although not changing radically its behavior had numerous negative side effects.

The presence of custom-made high bandwidth actuators and electronics lead to noticeable electro-magnetic compatibility problems. The only feasible solution was then to cut the power to the aileron 4 actuators on both sides of the aircraft. Fortunately the stopping torque and relative low inertia of the ailerons were such that no free motion was observed during the tests.

The presence of high bandwidth actuators also makes the noise analysis more difficult. Indeed, if an actuator is designed to work in the same domain as the one the modal analysis is performed in, some

unconventional behavior may be observed. This led to some delays during this camapaign as some of the heavy noise seen on some measurements was initially attributed to the instrumentation setup, while it was actually due to the actuators of the aircraft. In order to assess the presence of noise during the test of such aircraft, a preliminary step of recordings during the power-up of the aircraft systems should be performed systematically, to determine a noise picture and potentially isolated a problematic aircraft system.

This step was eventually performed on the P-FLEX aircraft at the end of the GVT. Several effects were evaluated : sensor cabling modification, sensor replacement, sensor connection, sensor separation from the structure. None of these effects showed any relevant influence on the large noise level observed. Finally, a full power-up sequence of the Direct Drives was recorded with the following sequence

1. $t = 0$ s Start recording of the GVT channels, as for a standard GVT measurement
2. $t = 10$ s Start power-up sequence of the Direct Drive controllers and actuators
3. $t = 28$ s A noise coming from the Direct Drive actuators was noticeable
4. $t = 43$ s Power-down the Direct Drive controllers and actuactors
5. $t = 62$ s Stop recording

The accelerometer signals recorded during that test are plotted in figure 16. There is an obvious and drastic increase in noise levels, starting from $t = 43$ s coincident with the noise noticed coming from the actuators. This noise can definetly be attributed to electromagnetic pulses emitted by the Direct Drive controller or actuator, as no shaker excitation is performed during this measurement run. As stated above, a measurement was even performed without a sensor connected onto a channel which led to similar observations. Though all sensors showed a specific noise pattern at the power-up of the direct drives, the light triaxis sensors were the most sensitive to this phenomenon, as depicted in figure 16d. On the contrary, the bigger, therefore maybe better shielded Kistler triaxis sensors we less affected, see figure 16b.

Furthermore, testing an aircraft with several and large-bandwidth controllers can lead to a vast increase in test complexity. This is mostly due to the large amount of structure and controller state combinations to test. Also, the aircraft state has to be fully known at each time during the GVT in order to ensure identified data quality. The test planning should account for all of these configurations very precisely. Finally, controller readiness should be considered as critical as airframe readiness and the GVT should be performed only once all controls systems acting on flight or airframe dynamics are in airworthy.

The amount of freeplay and friction in the control surfaces actuation systems led to very complex behavior in the high frequency domain. Though this domain was of little interest for this particular project, it must be recalled that such effects may have very negative consequences on the aircraft lifecycle. In fact, such effect may lead to controller efficiency problems, increased structural fatigue or even unstable dynamic phenomena.

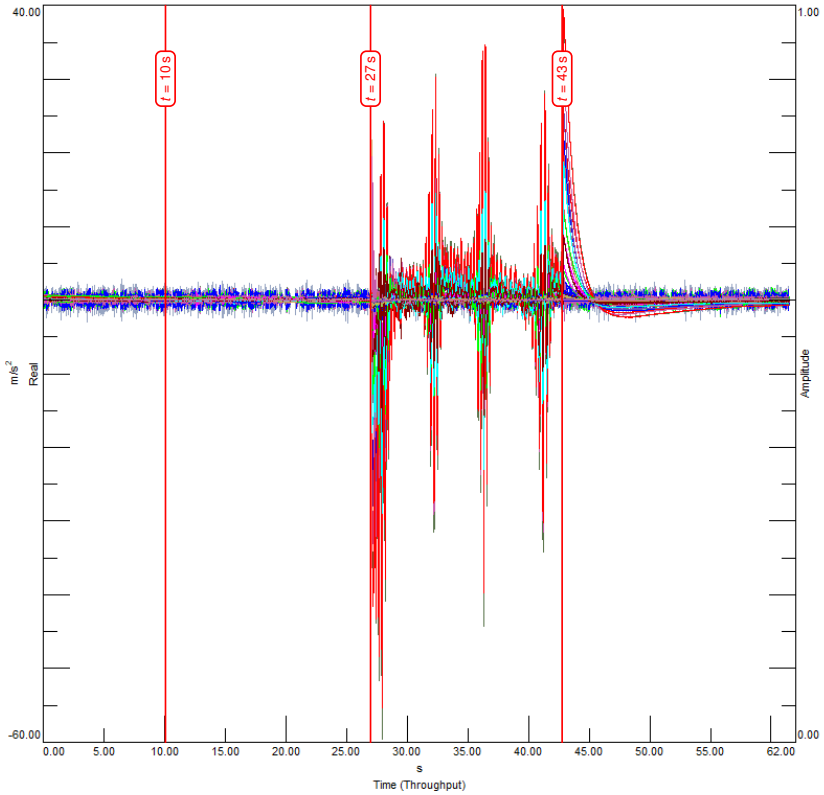

(a) All accelerometers.

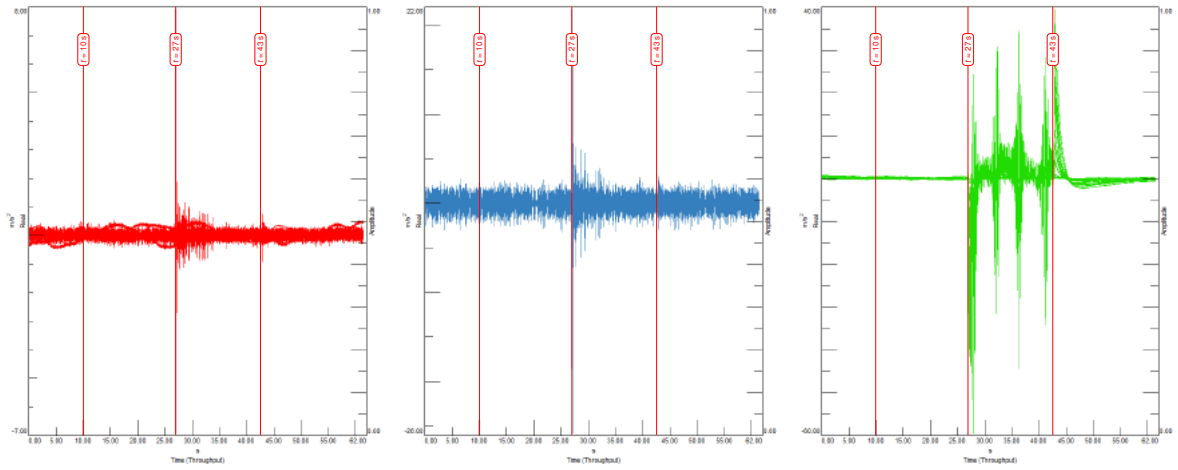

(b) Kistler triaxis sensors.

(c) Light uniaxis sensors.

(d) Light triaxis sensors.

Figure 16: Time signals of aircraft accelerometers during the power-up test of the Direct Drives. Time keypoints (|).

6 Conclusion

Successful ground testing activities were conducted by TUM, SZTAKI, ONERA and DLR. The direct drive was tested at different load equivalent velocities and demonstrated satisfactory performance regarding positional errors and temperature effects. A static test of the wings was first simulated in Nastran and then measured in the laboratory. The aircraft was able to sustain the 4g static load as per the design requirements. The measured static deflection was 0.1 m less than simulated indicating a stiffer wing, and required updates to the FE model. The remote control system was range tested with both stationary and taxi tests. The system showed acceptable signal strength within the operational boundaries of the flight box. The telemetry system was also re-designed and range tested. Modification to the frequency, antenna layout and software showed improvements, however dropouts were still experienced and showed no clear trend. A GVT was successfully conducted to determine the equivalent modal models of the aircraft in three different configurations. Investigations into non-linearities and the effect of the flutter stopper masses on the flutter critical modes were also performed. The results from the GVT were used to update the simulation models both for the flutter calculations and well as for tuning the active flutter controllers. Finally, the ground testing provided valuable information for the final flight test campaigns of the P-FLEX aircraft.

7 Bibliography

[1] Daniel Teubl, Szabolcs Toth, and Balint Vanek. Flipased D3.7 manufacturing advanced wing and fuselage finalized. Technical report, TUM, 2023.

[2] Szabolcs Tóth, László Gyulai, Dániel Balogh, Mihály Nagy, Bálint Vanek, Daniel Teubl, Sebastian Köberle, Julius Bartasevicius, Christian Rößler, Yves Govers, Keith Soal, Yasser M. Meddaikar, Johannes Dillinger, Jurij Sodja, Panos Georgopoulos, and Christos Koimtzoglou. D4.2: Vehicle ground test report including hils results. Technical report, DLR, 2019.

[3] Fanglin Yu, Daniel Teubl, Szabolcs Tóth, Nicolas Guérin, Keith Soal, Thiemo Kier, and Özge Süelözgen. Flipased D3.10 flight readiness review demonstrator with advanced wing. Technical report, TUM, 2023.

Appendix A

GVT Experimental data

1 Experimental setup geometry

Geometry UNV file
Geometry MAP file

2 Configuration C1a modal data

C1a modal data UNV file

3 Configuration C1b modal data

C1a modal data UNV file

4 Configuration C1d modal data

C1a modal data UNV file

Appendix B

GVT mode shapes

1 Configuration C1a

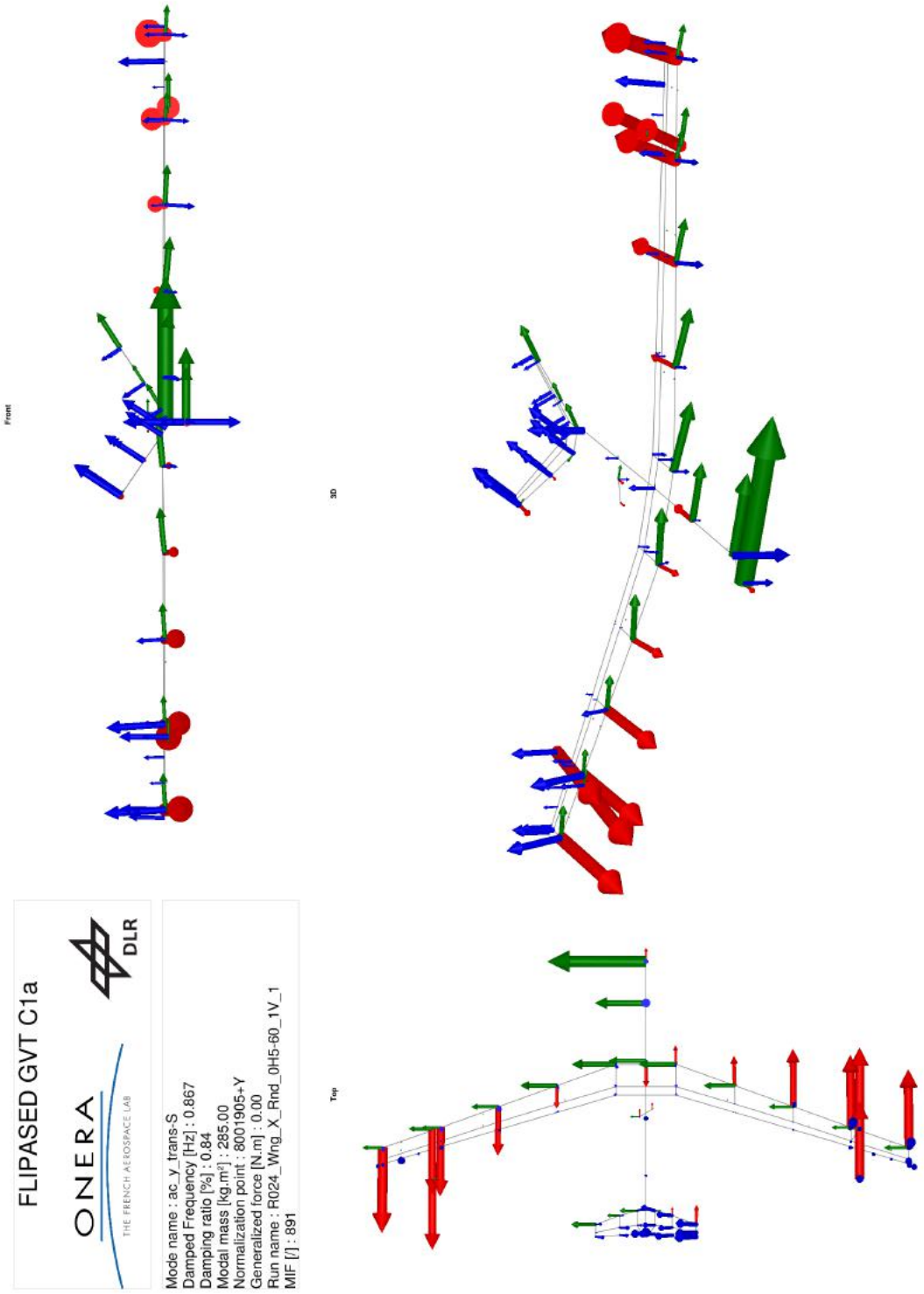

Figure B.1: Mode shape and properties of mode ac_y_trans-S identified in C1a.

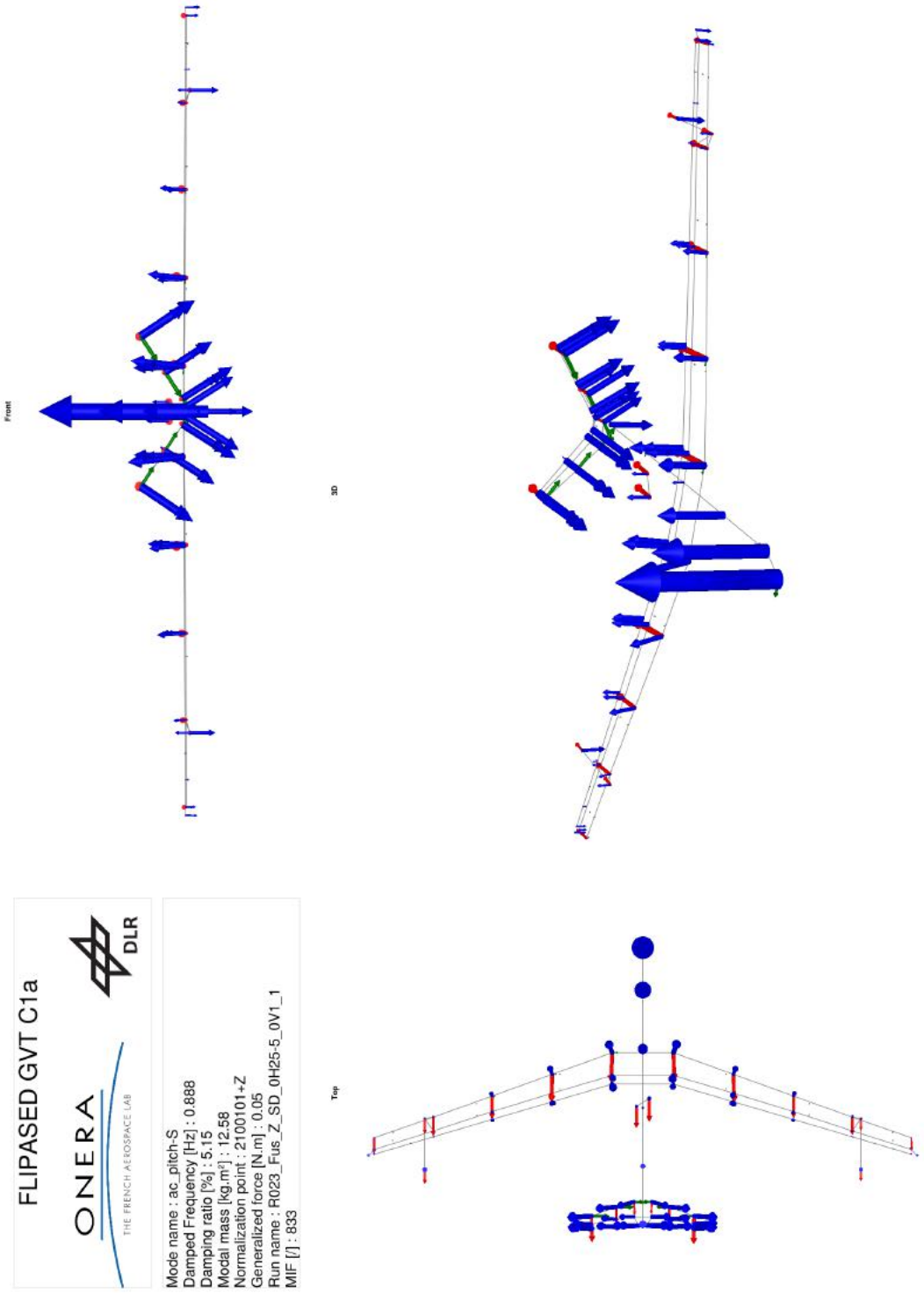

Figure B.2: Mode shape and properties of mode ac_pitch-S identified in C1a.

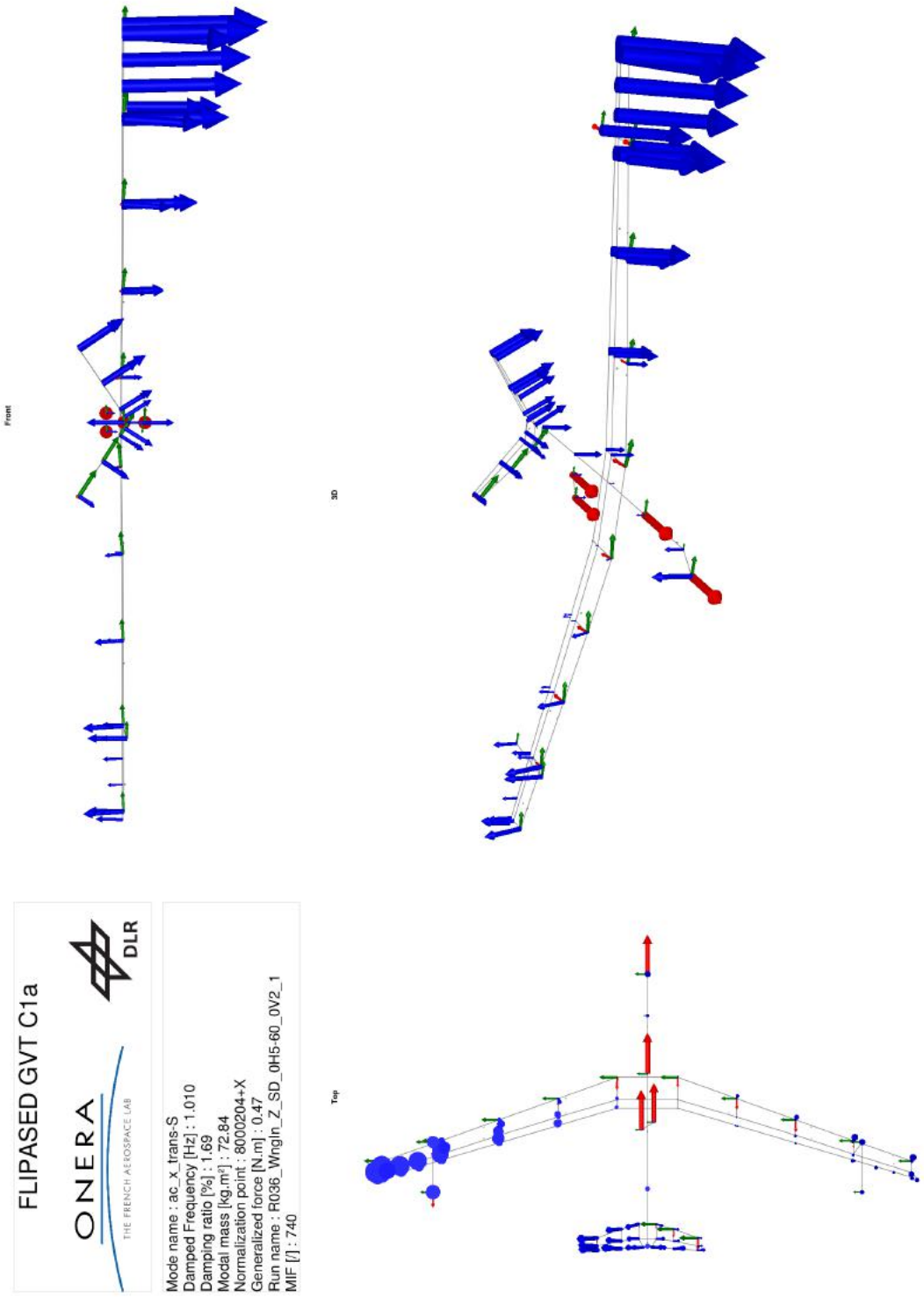

Figure B.3: Mode shape and properties of mode ac_x_trans-S identified in C1a.

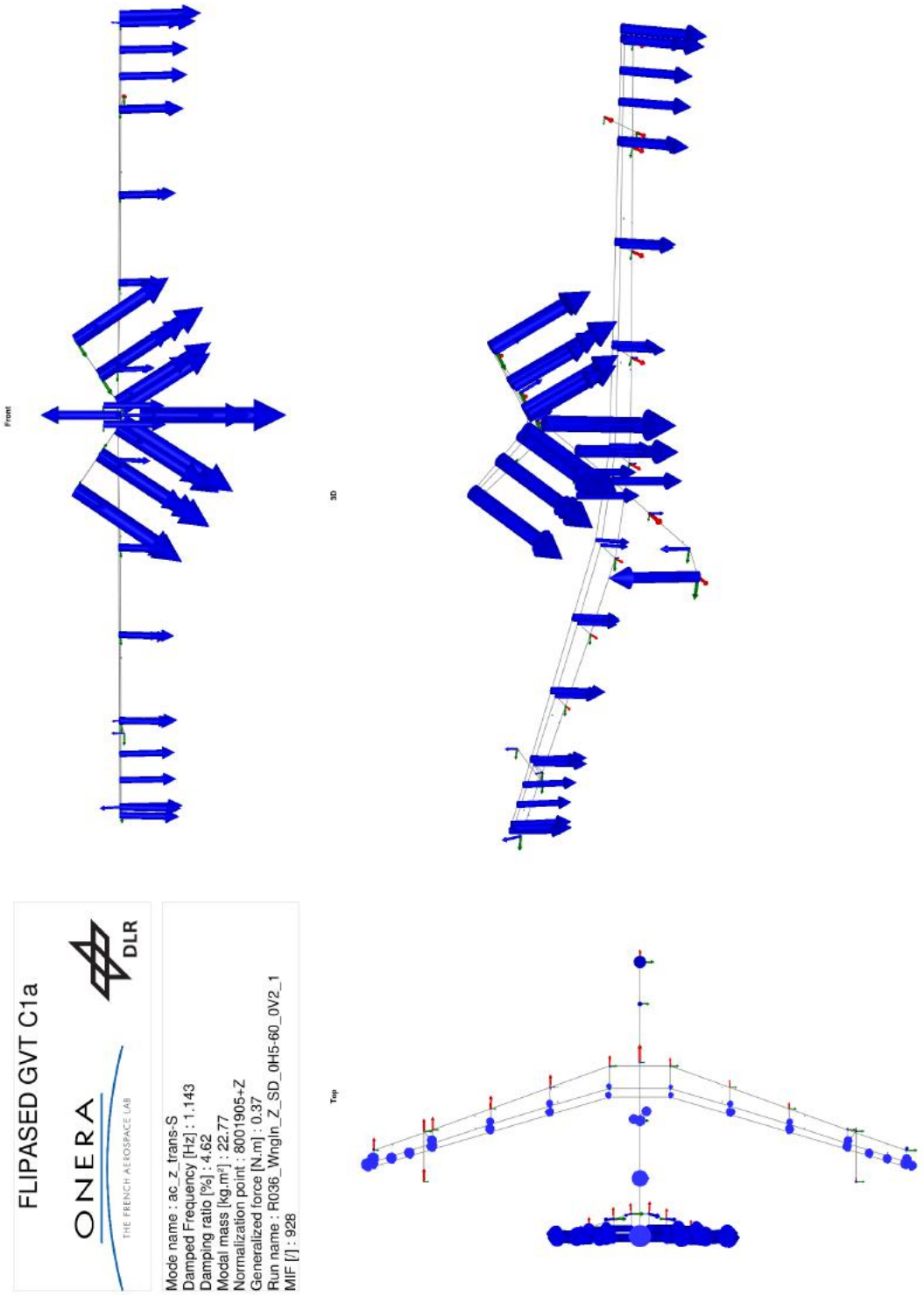

Figure B.4: Mode shape and properties of mode ac_z_trans-S identified in C1a.

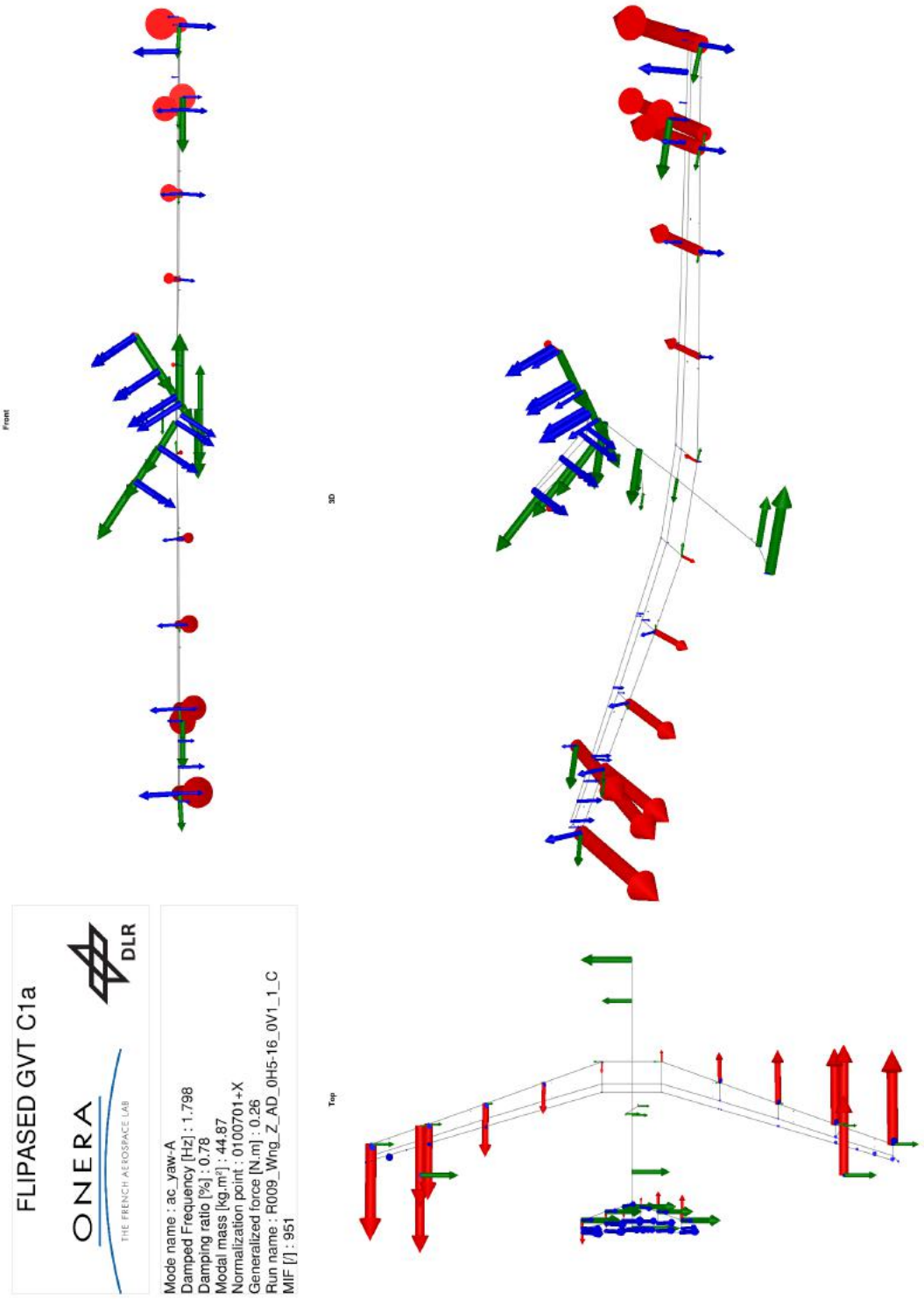

Figure B.5: Mode shape and properties of mode ac_yaw-A identified in C1a.

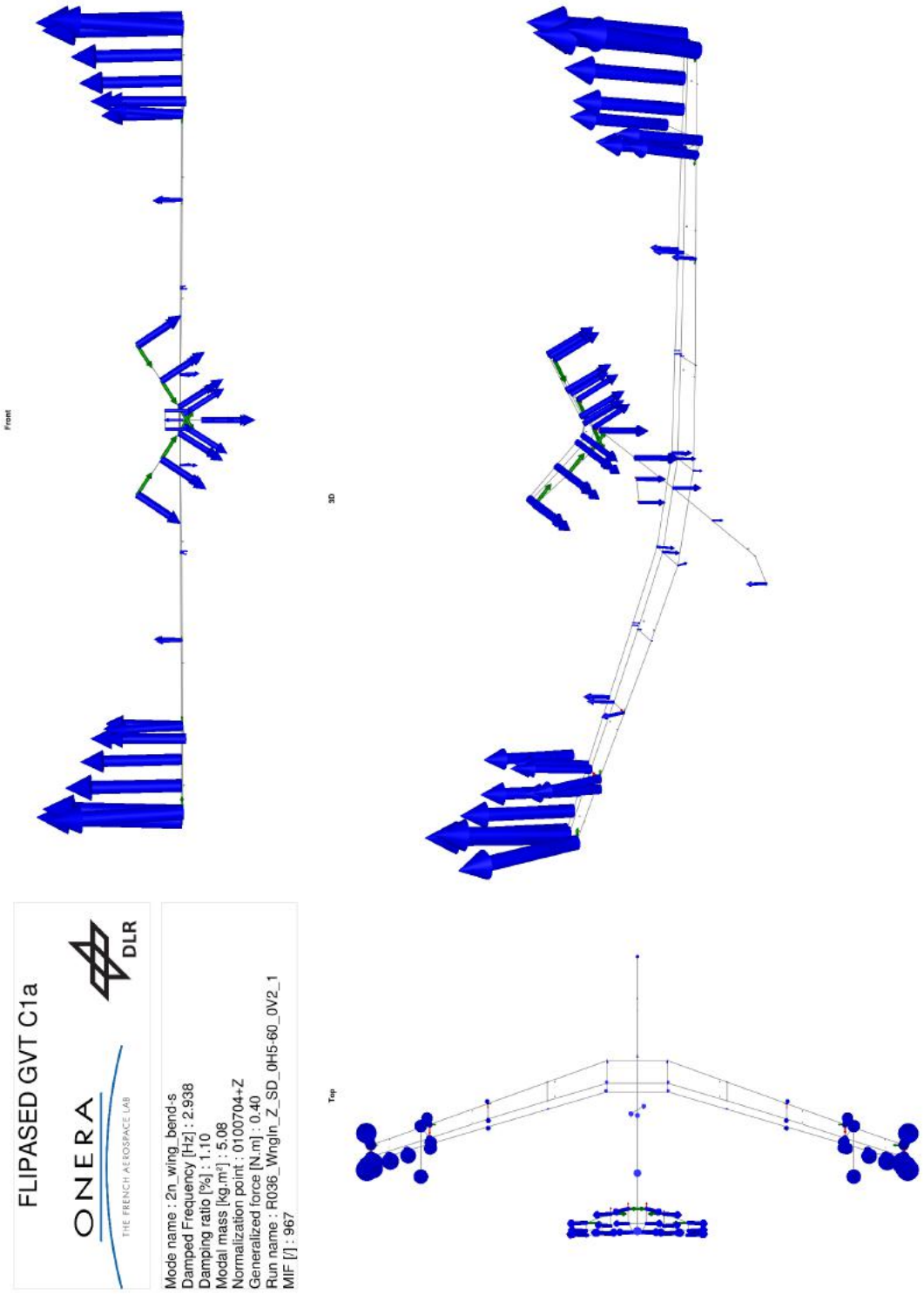

Figure B.6: Mode shape and properties of mode 2n_wing_bend-s identified in C1a.

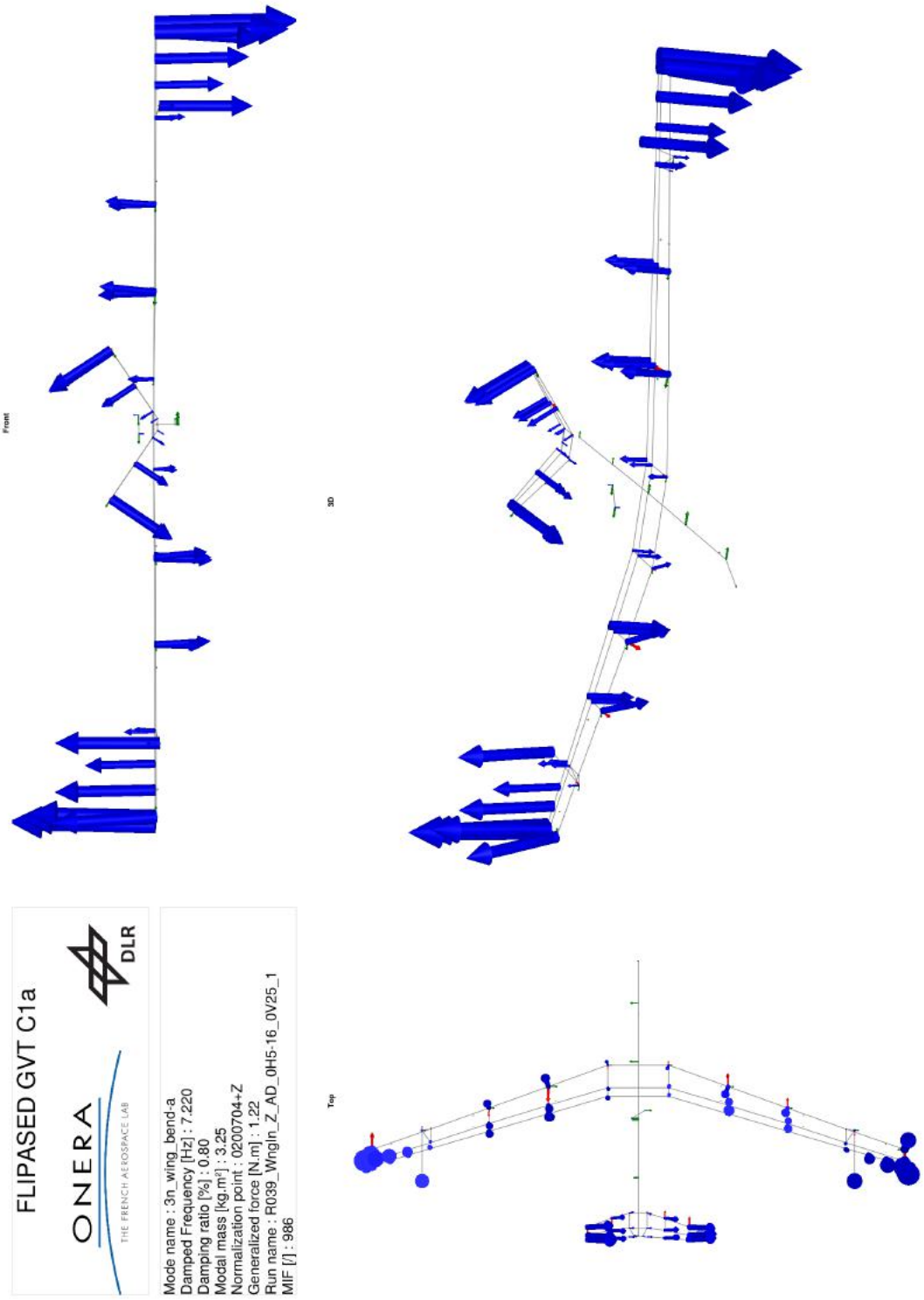

Figure B.7: Mode shape and properties of mode 3n_wing_bend-a identified in C1a.

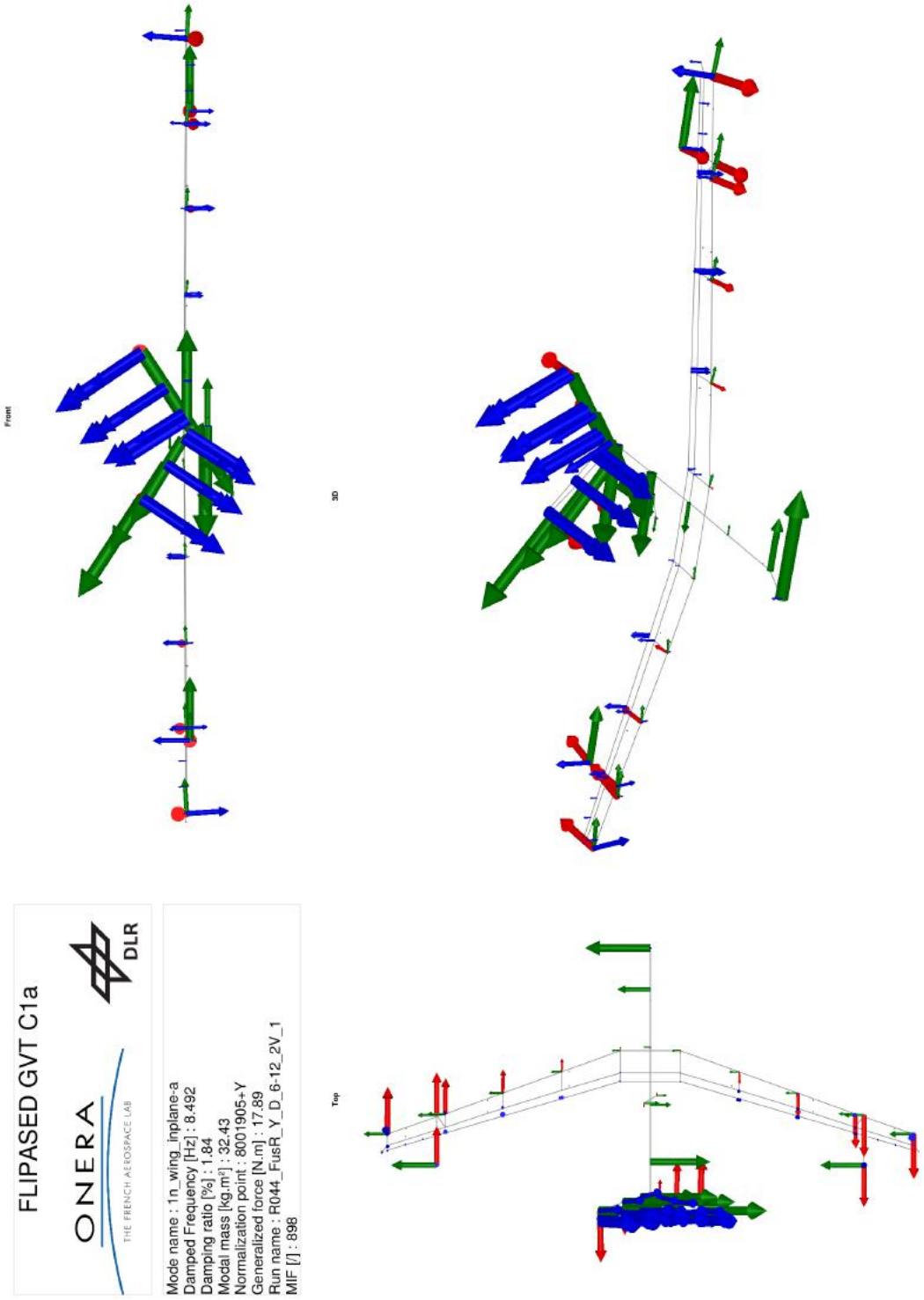

Figure B.8: Mode shape and properties of mode 1n_wing_inplane-a identified in C1a.

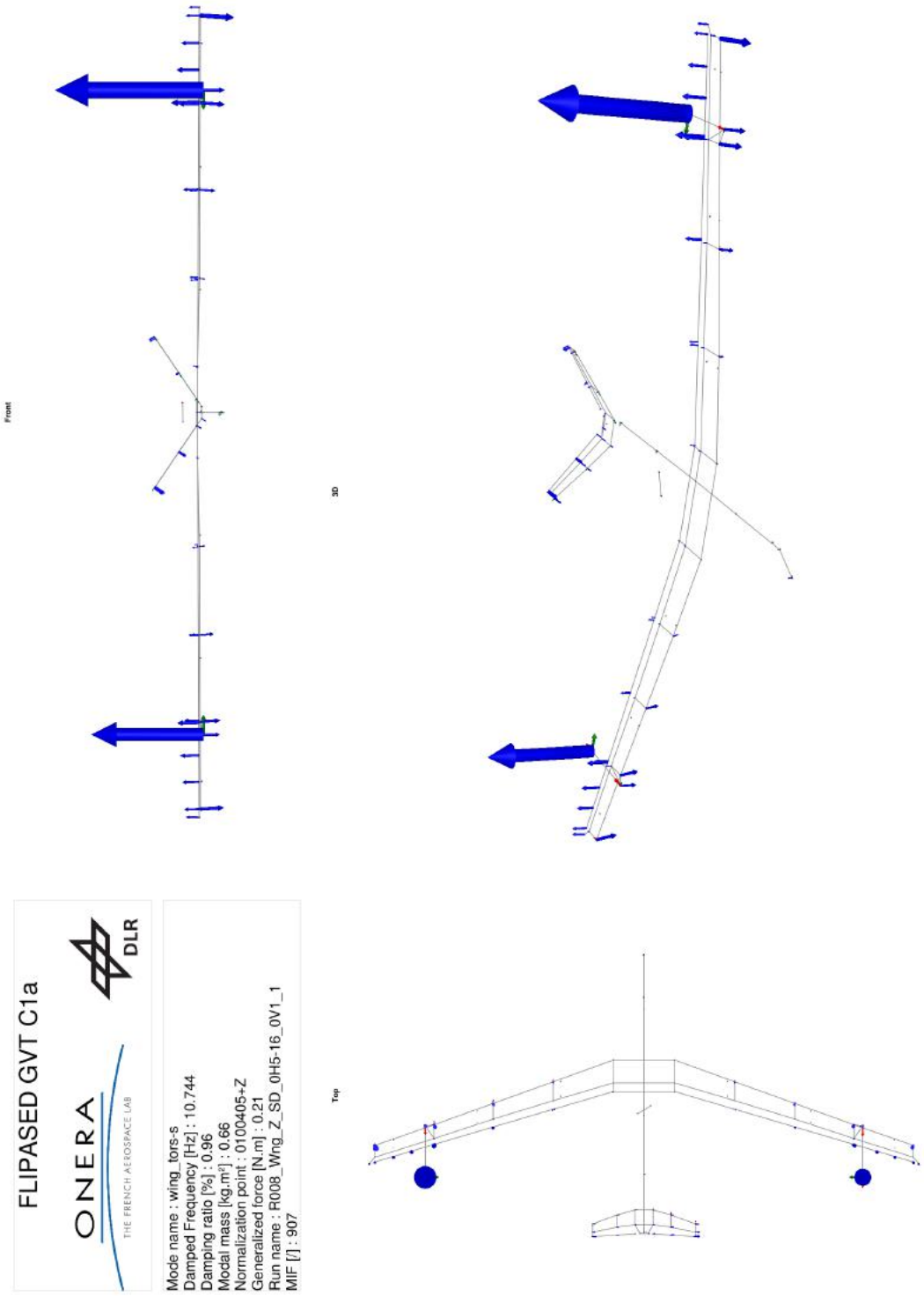

Figure B.9: Mode shape and properties of mode wing_tors-s identified in C1a.

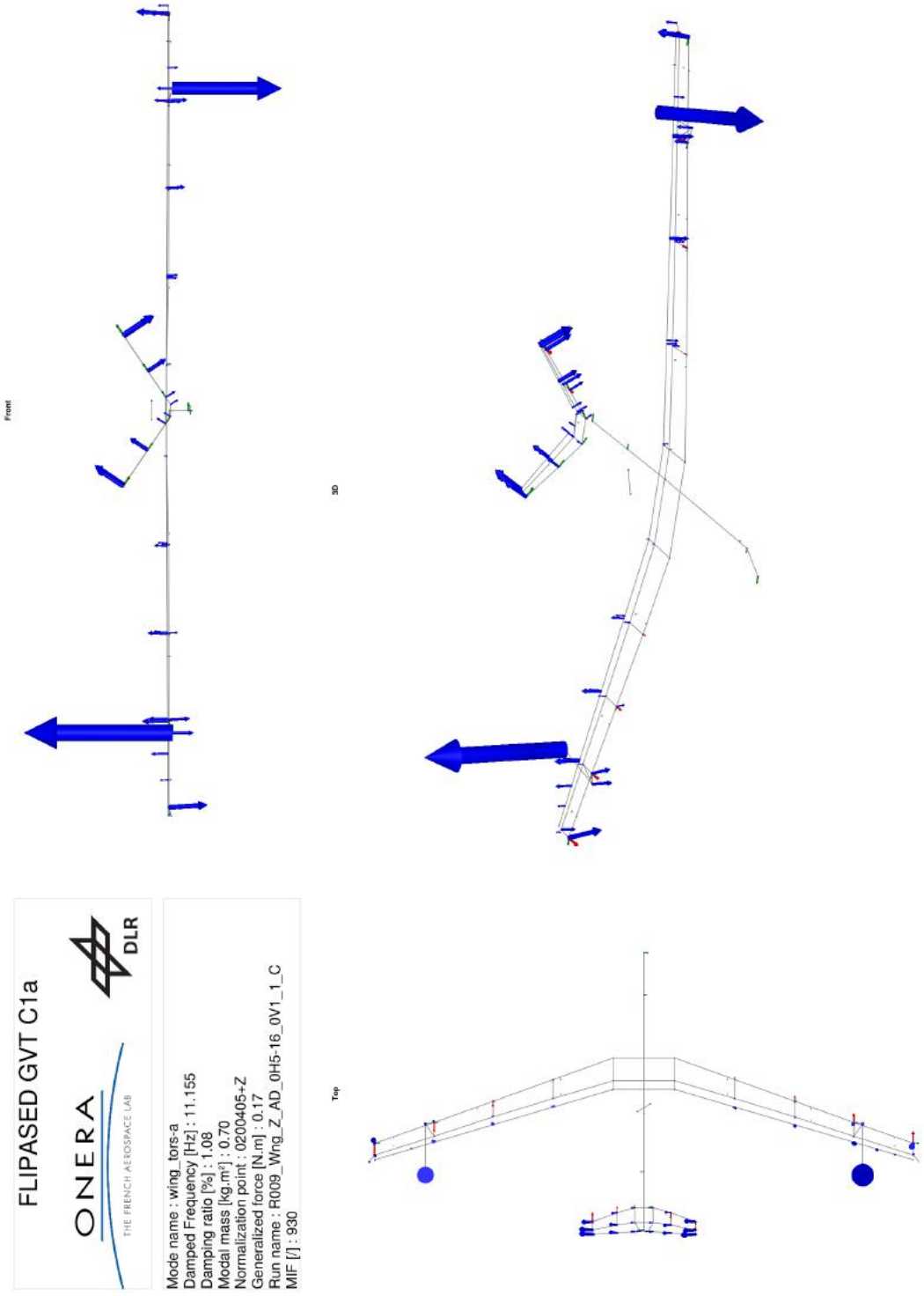

Figure B.10: Mode shape and properties of mode wing_tors-a identified in C1a.

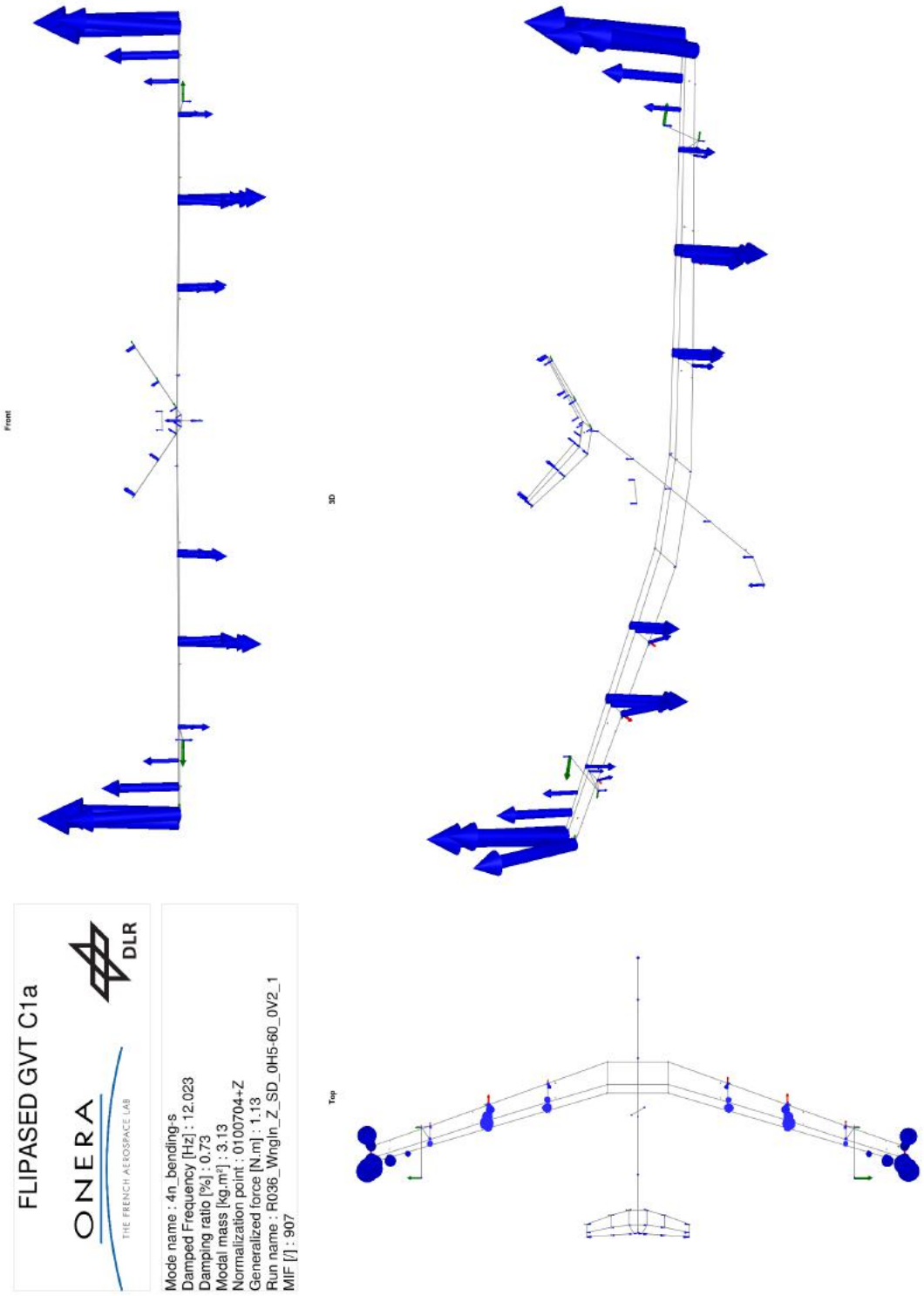

Figure B.11: Mode shape and properties of mode 4n_bending-s identified in C1a.

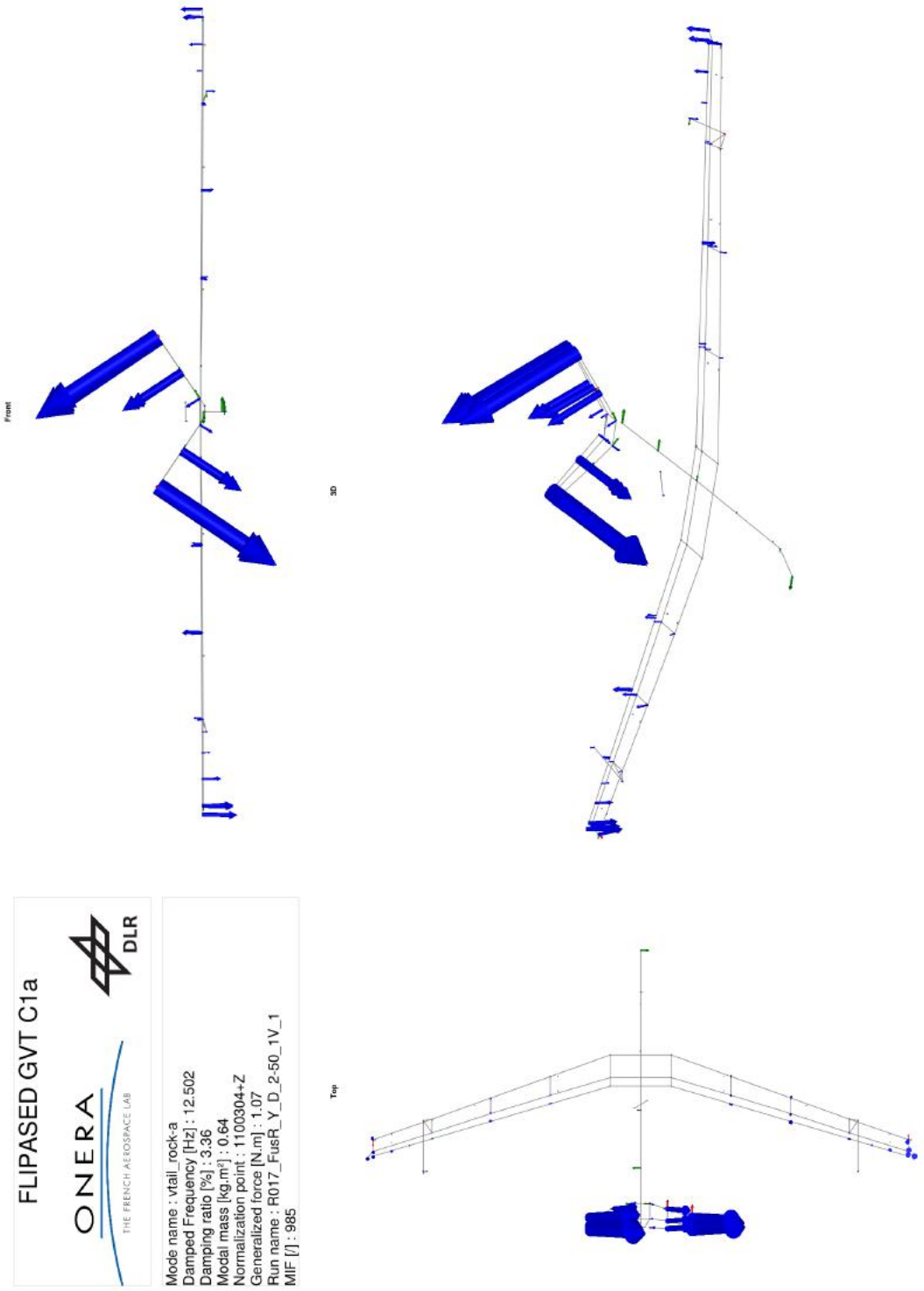

Figure B.12: Mode shape and properties of mode vtail_rock-a identified in C1a.

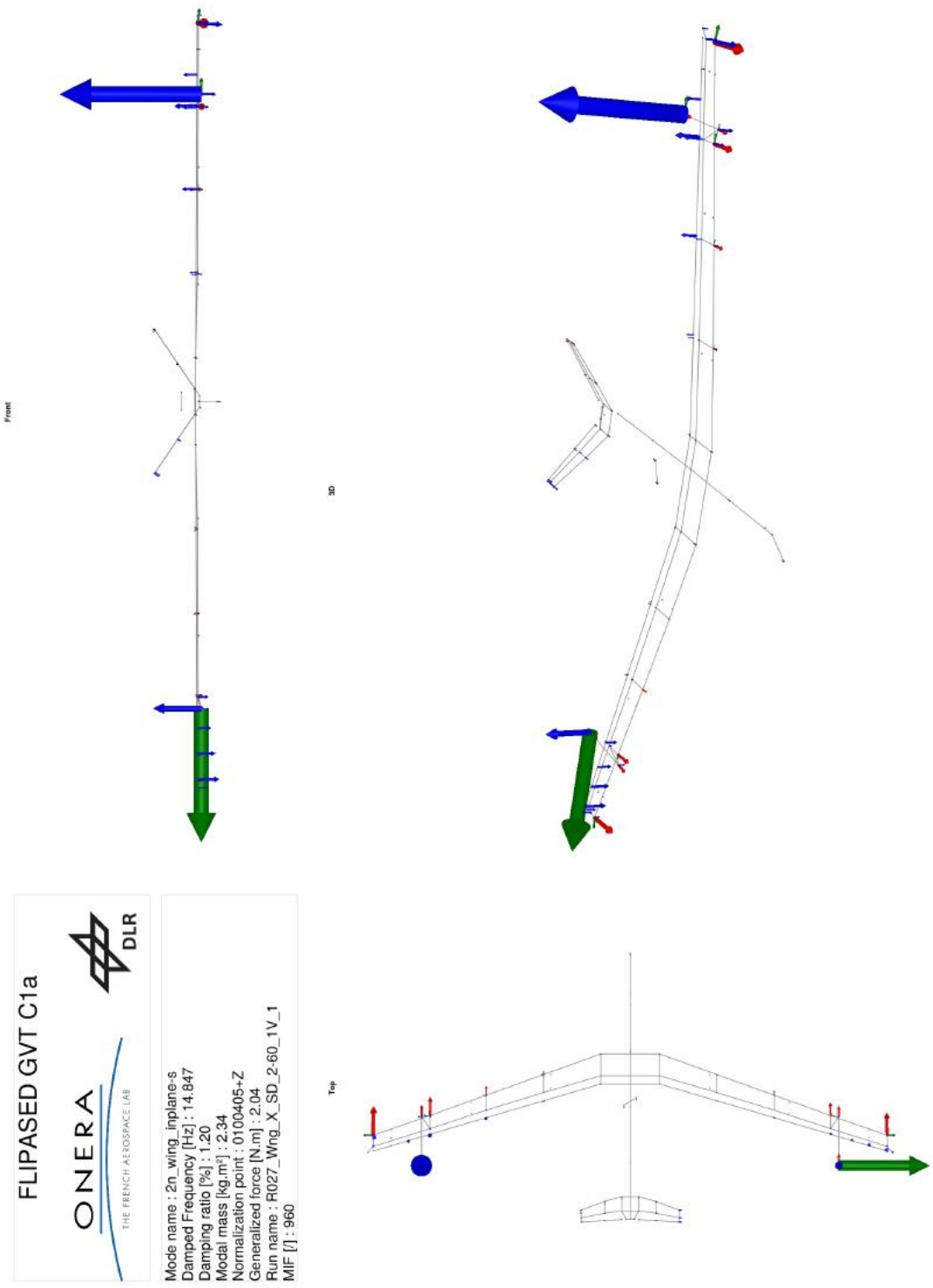

Figure B.13: Mode shape and properties of mode 2n_wing_inplane-s identified in C1a.

Figure B.14: Mode shape and properties of mode flutterstop_right_y identified in C1a.

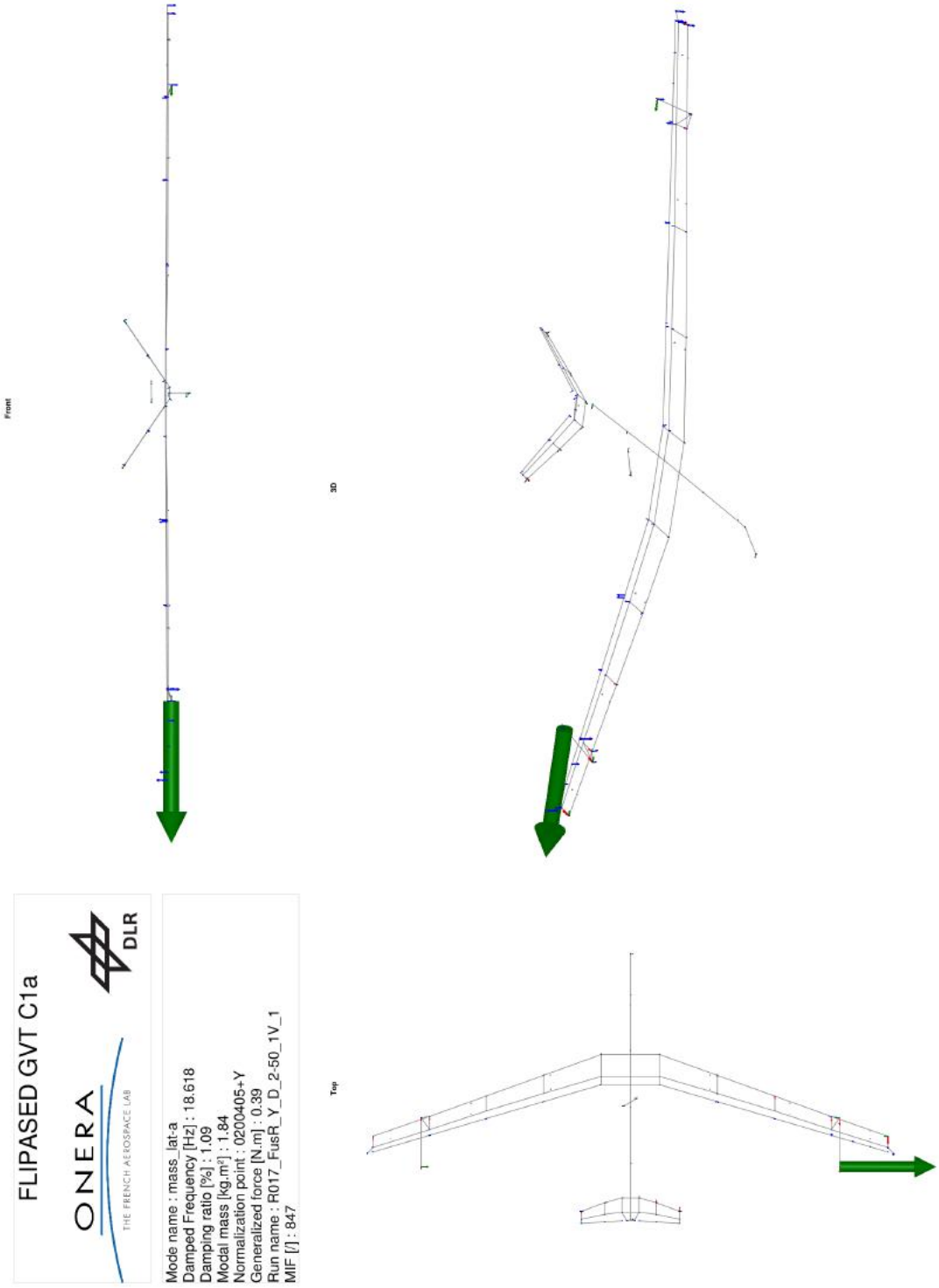

Figure B.15: Mode shape and properties of mode mass_lat-a identified in C1a.

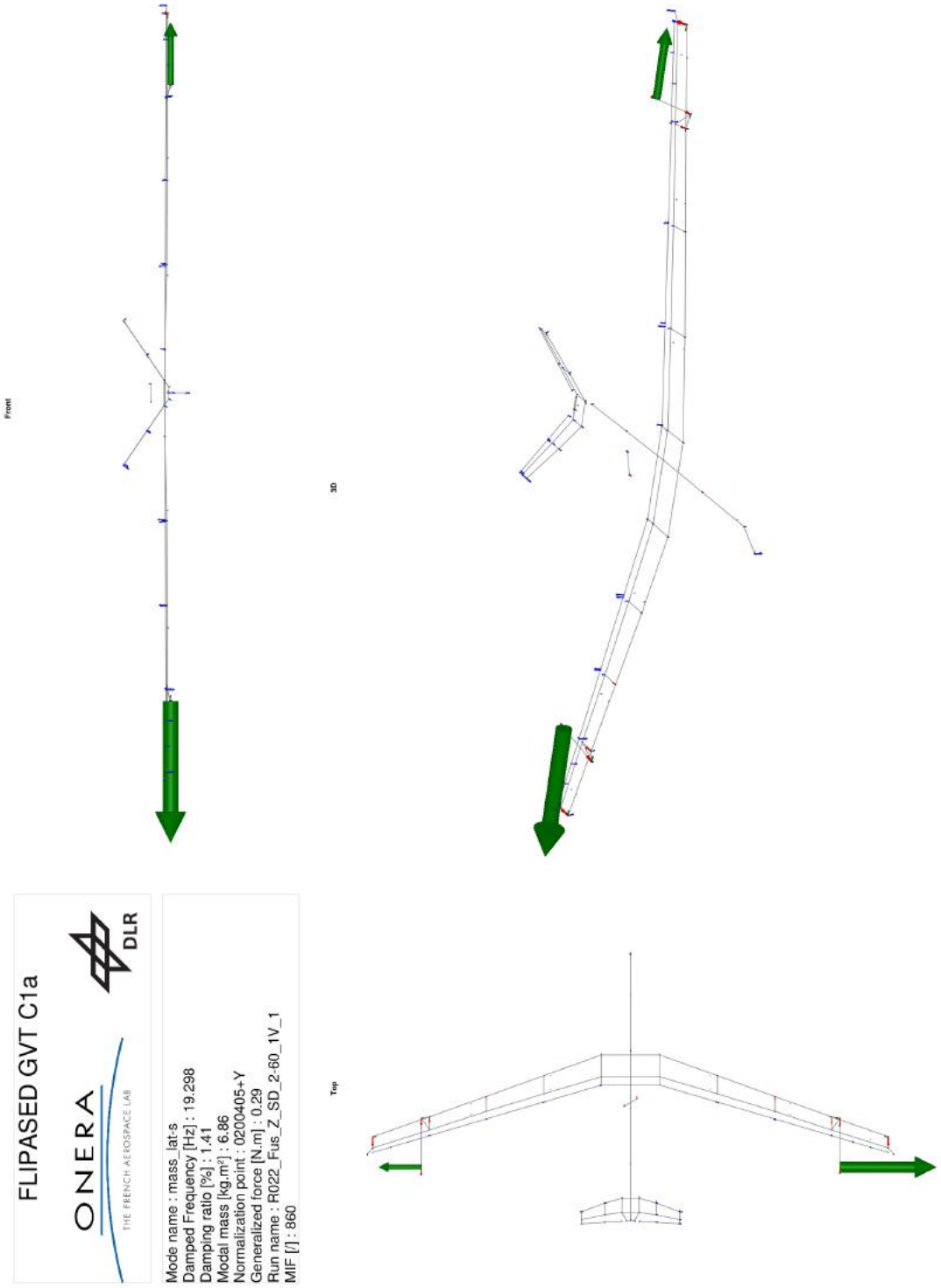

Figure B.16: Mode shape and properties of mode mass_lat-s identified in C1a.

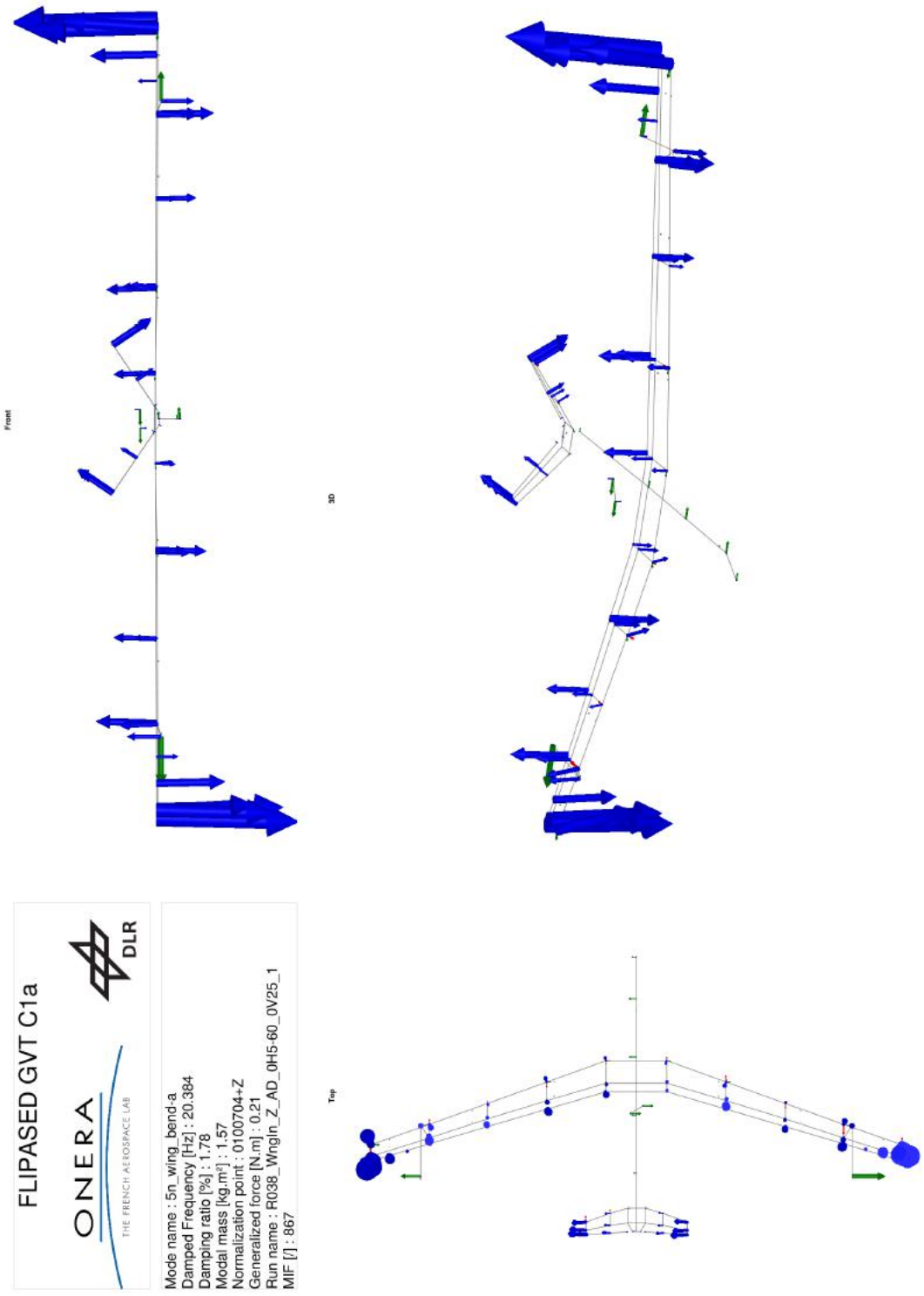

Figure B.17: Mode shape and properties of mode 5n_wing_bend-a identified in C1a.

Figure B.18: Mode shape and properties of mode flutterstop_left_y identified in C1a.

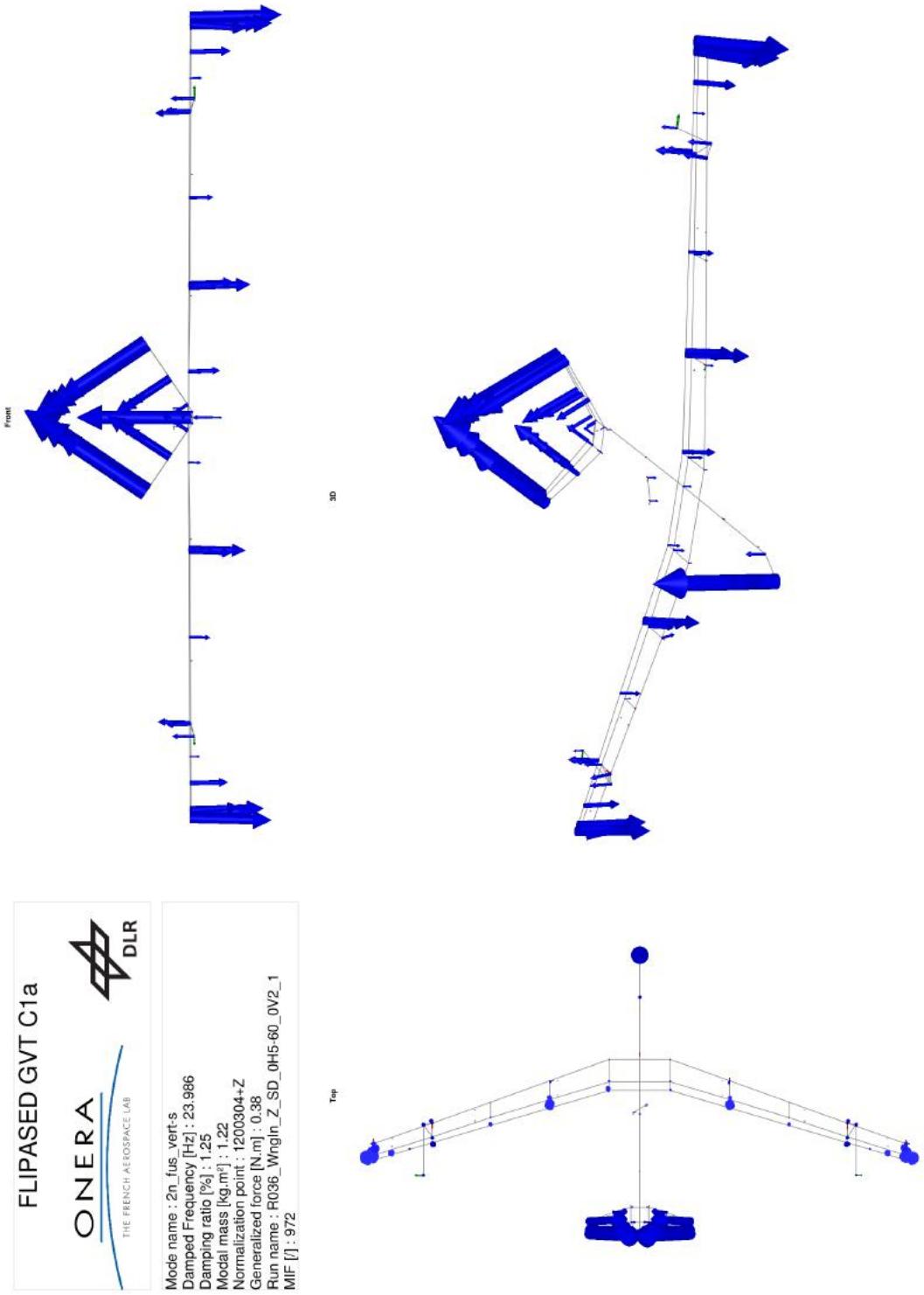

Figure B.19: Mode shape and properties of mode 2n_fus_vert-s identified in C1a.

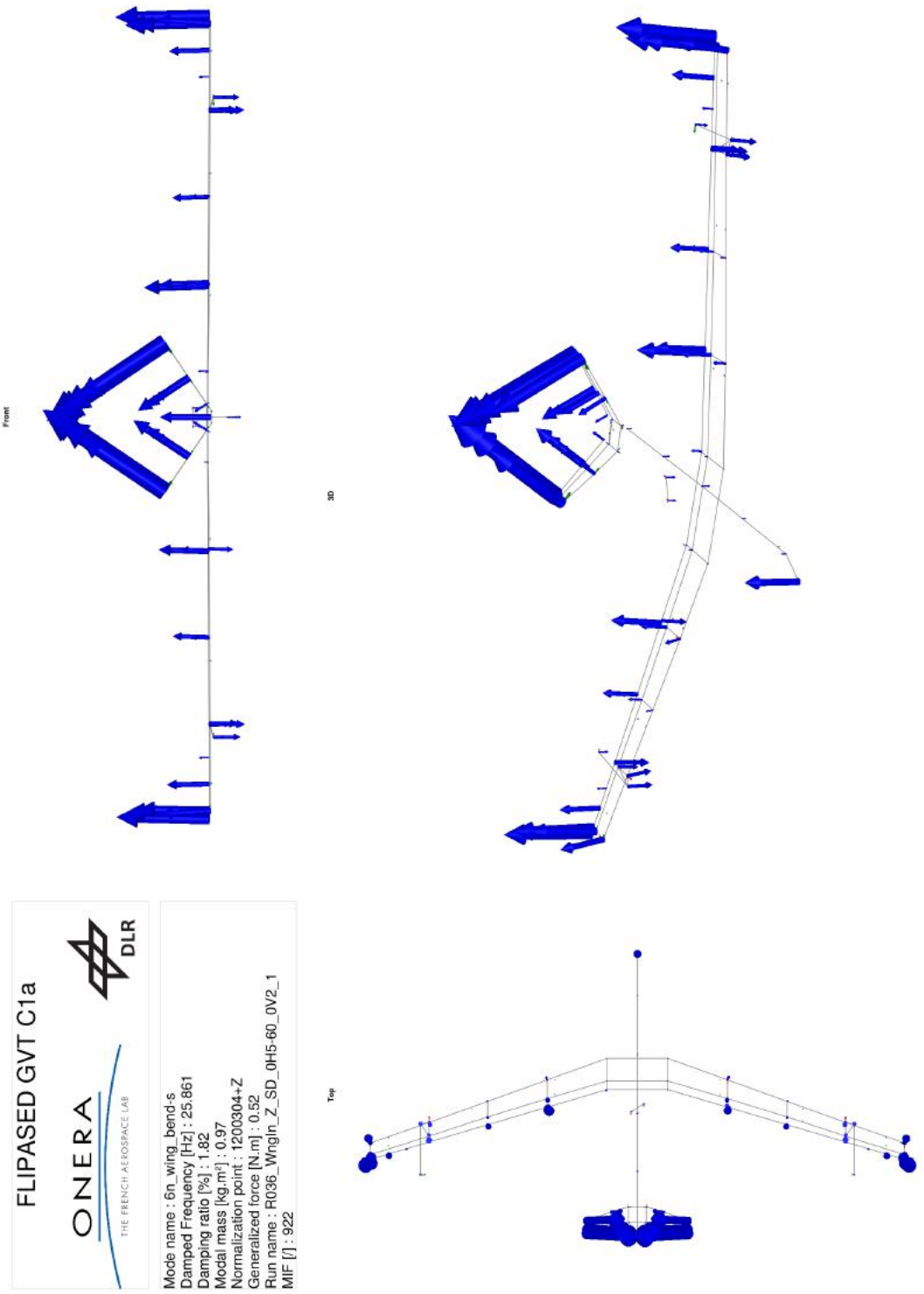

Figure B.20: Mode shape and properties of mode 6n_wing_bend-s identified in C1a.

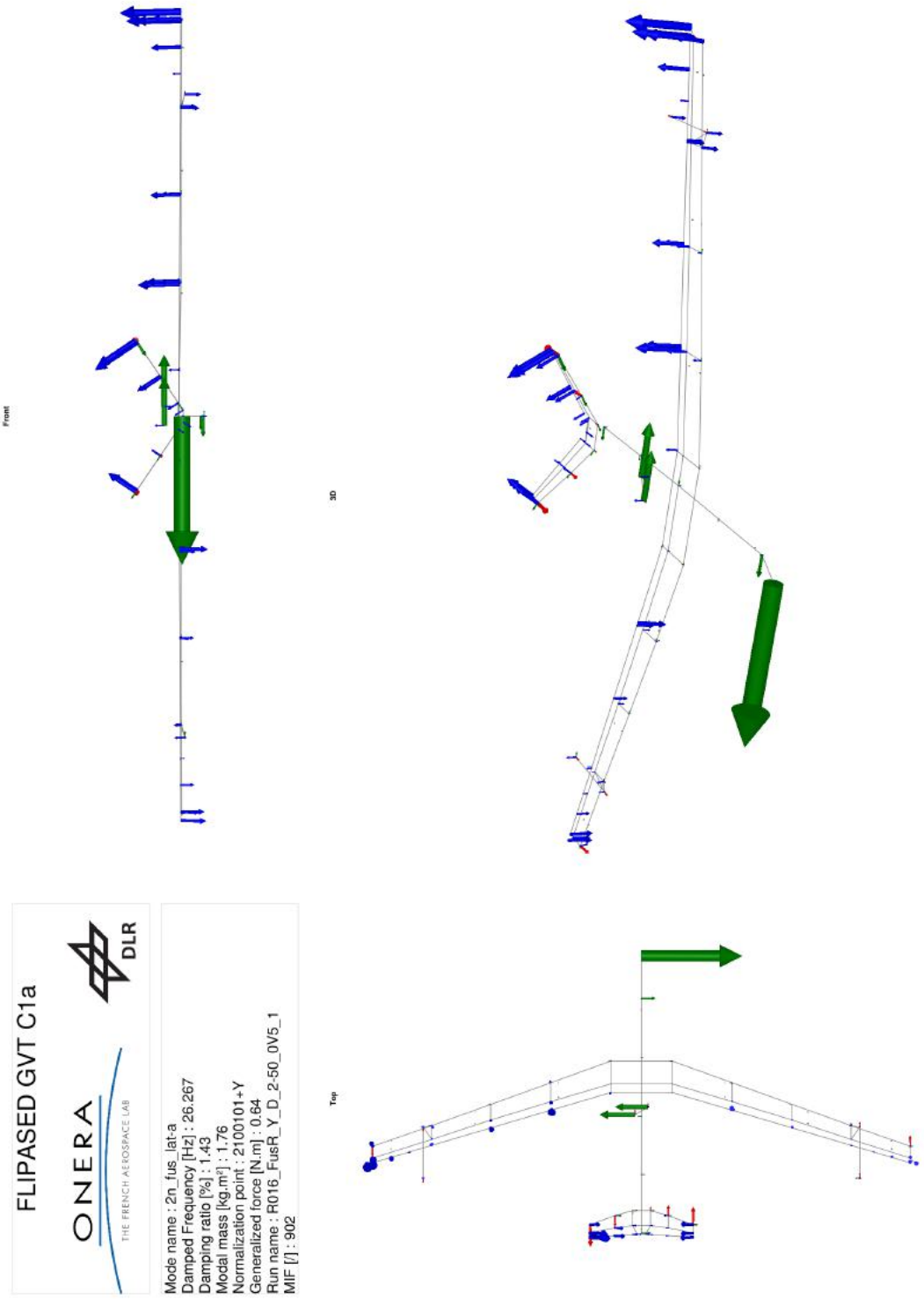

Figure B.21: Mode shape and properties of mode 2n_fus_lat-a identified in C1a.

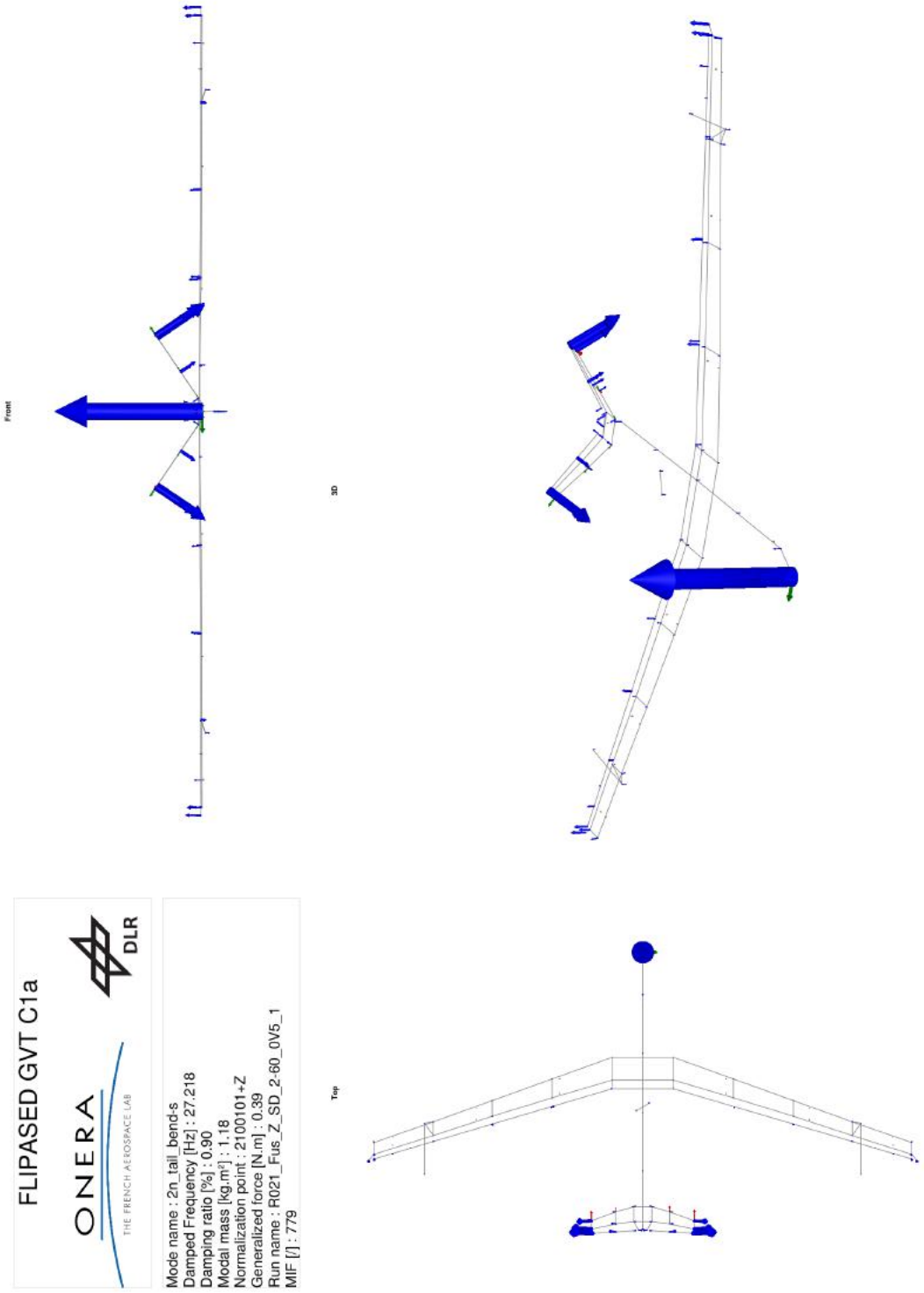

Figure B.22: Mode shape and properties of mode 2n_tail_bend-s identified in C1a.

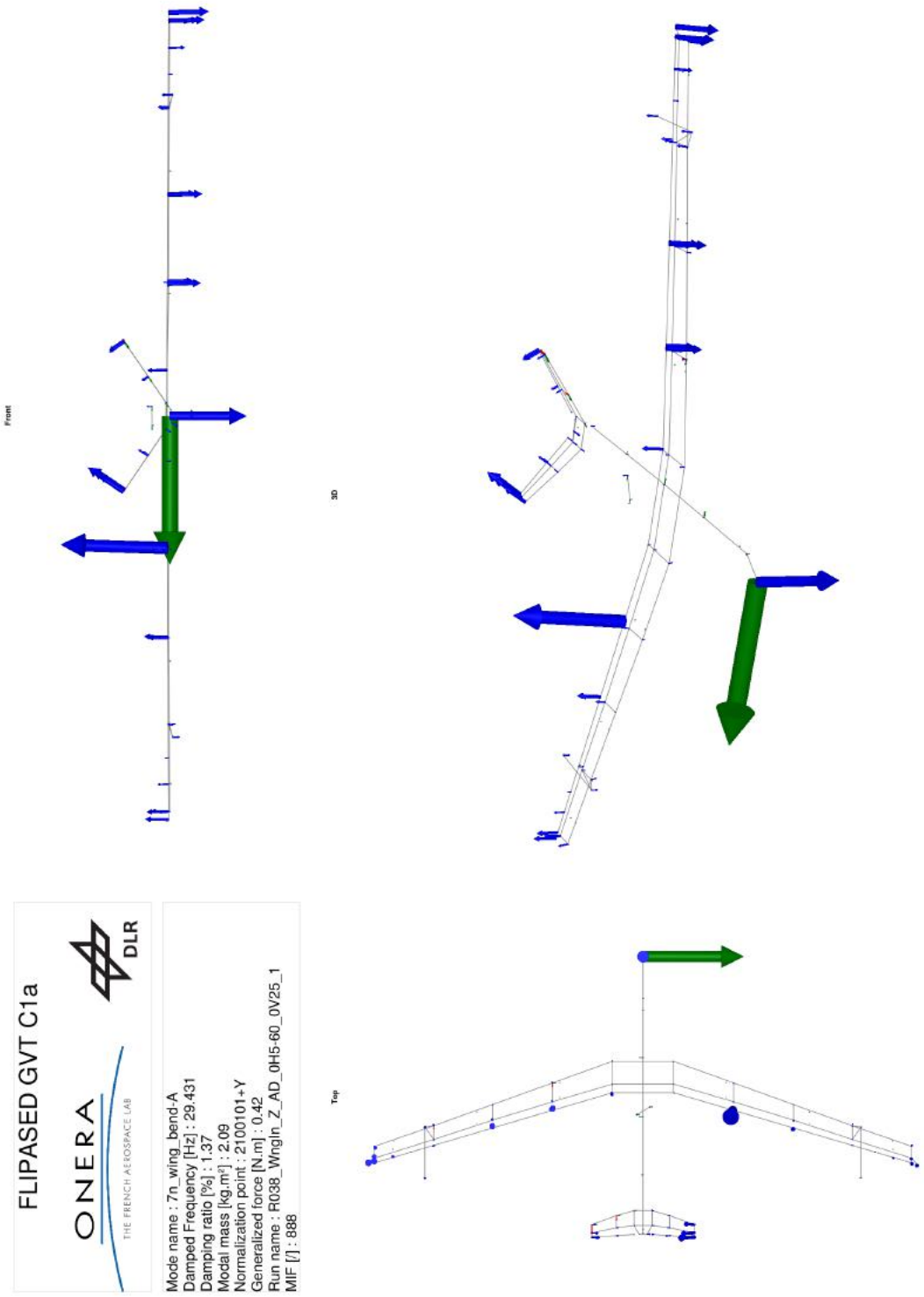

Figure B.23: Mode shape and properties of mode 7n_wing_bend-A identified in C1a.

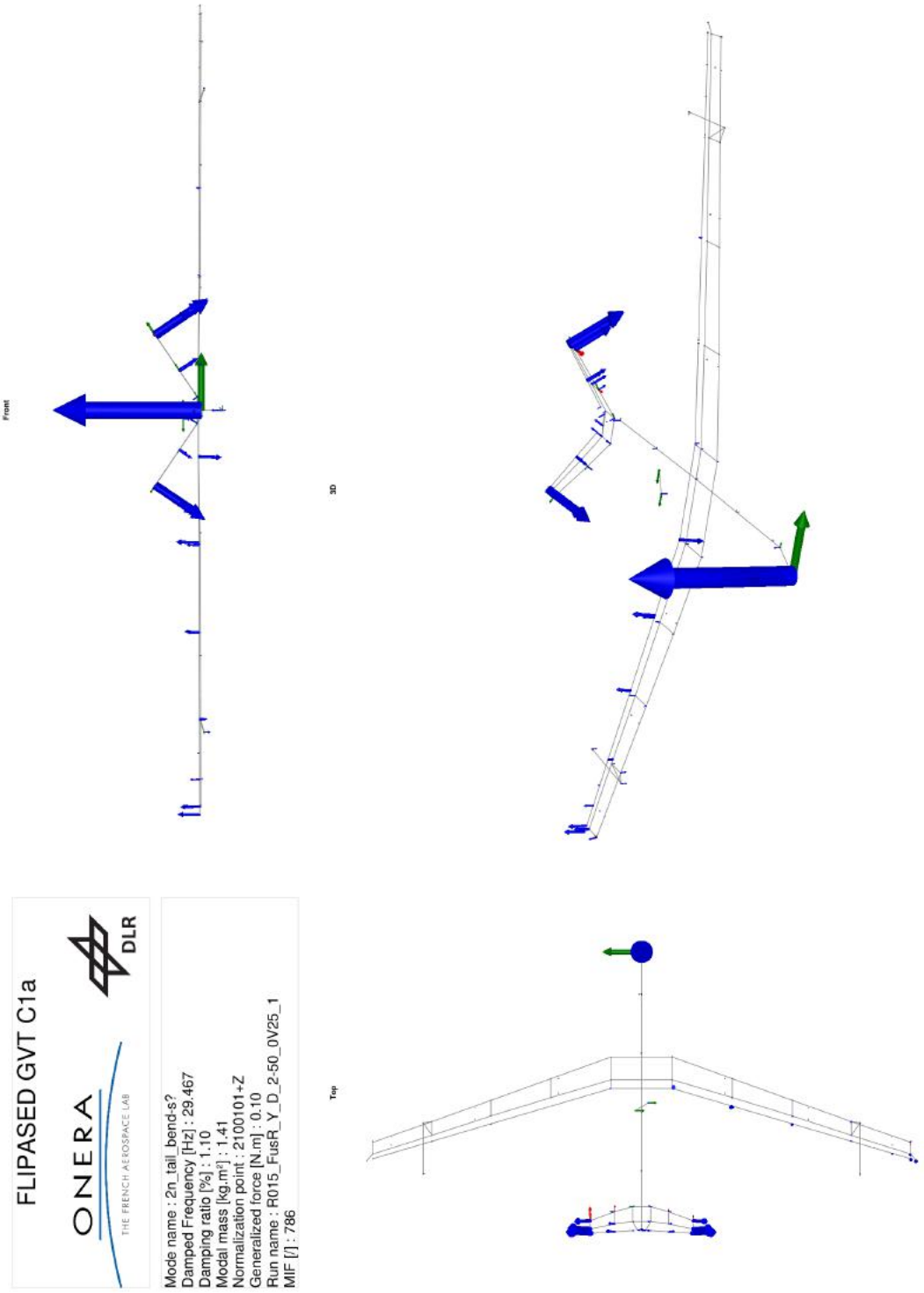

Figure B.24: Mode shape and properties of mode 2n_tail_bend-s? identified in C1a.

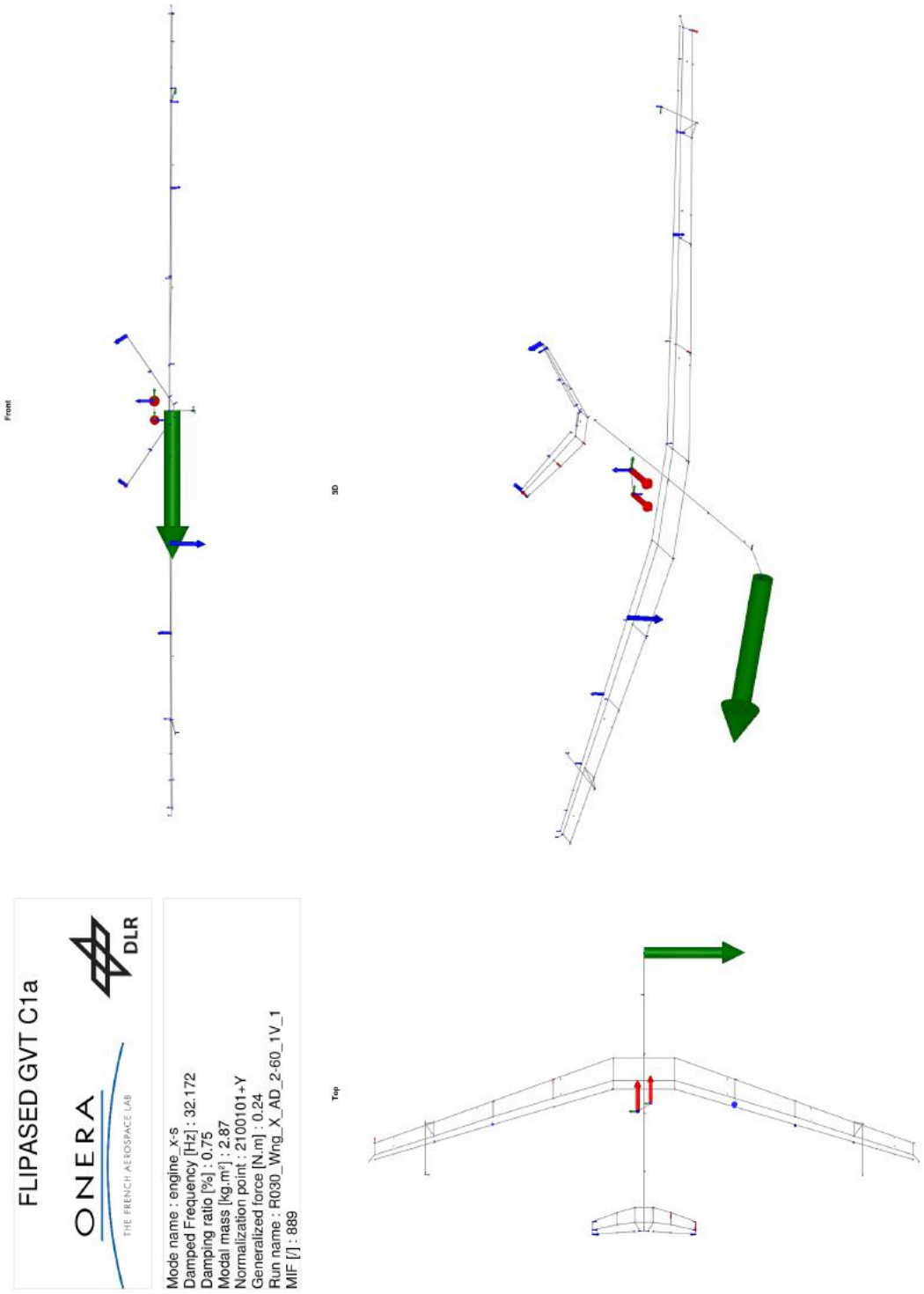

Figure B.25: Mode shape and properties of mode engine_x-s identified in C1a.

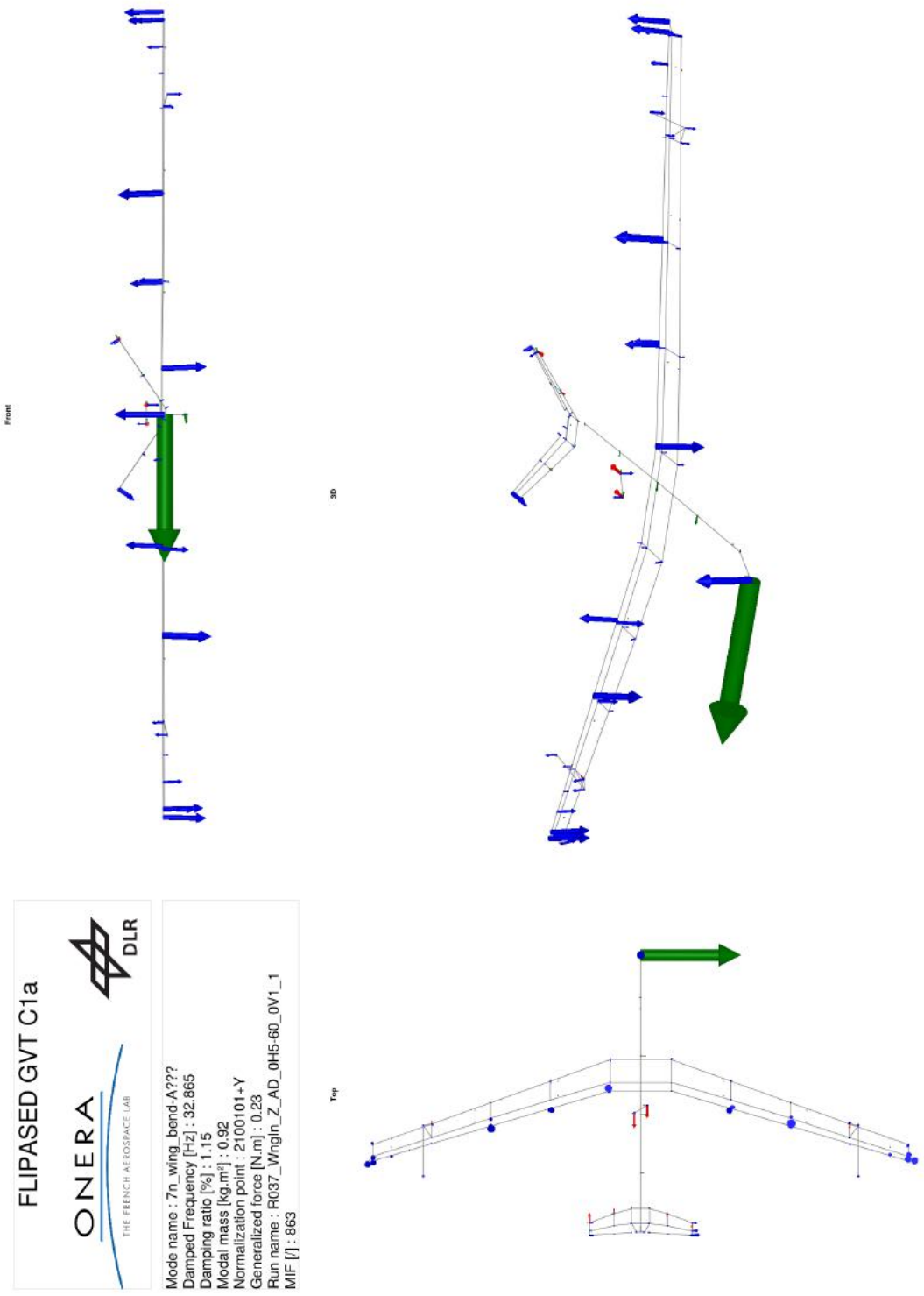

Figure B.26: Mode shape and properties of mode 7n_wing_bend-A??? identified in C1a.

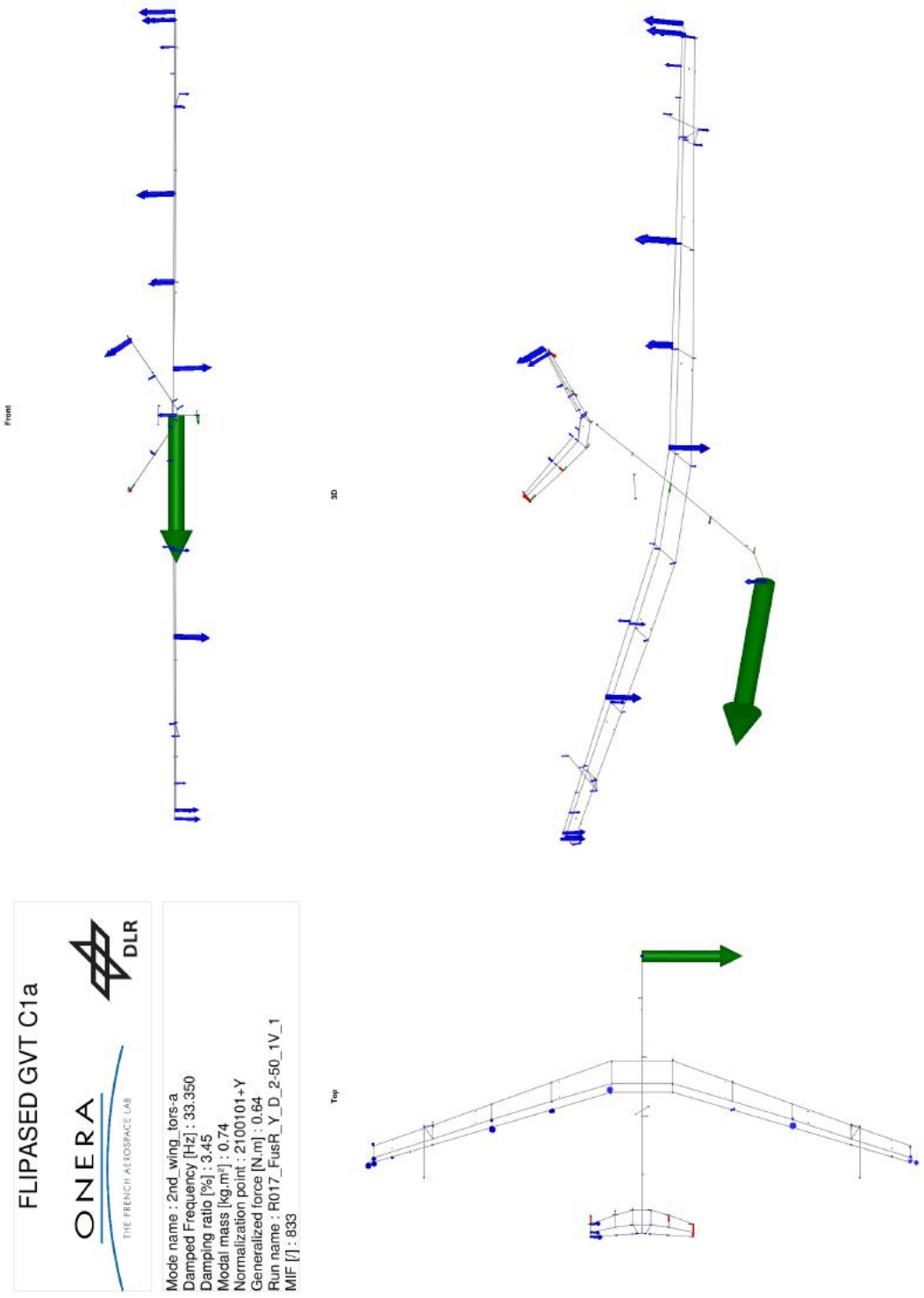

Figure B.27: Mode shape and properties of mode 2nd_wing_tors-a identified in C1a.

2 Configuration C1b

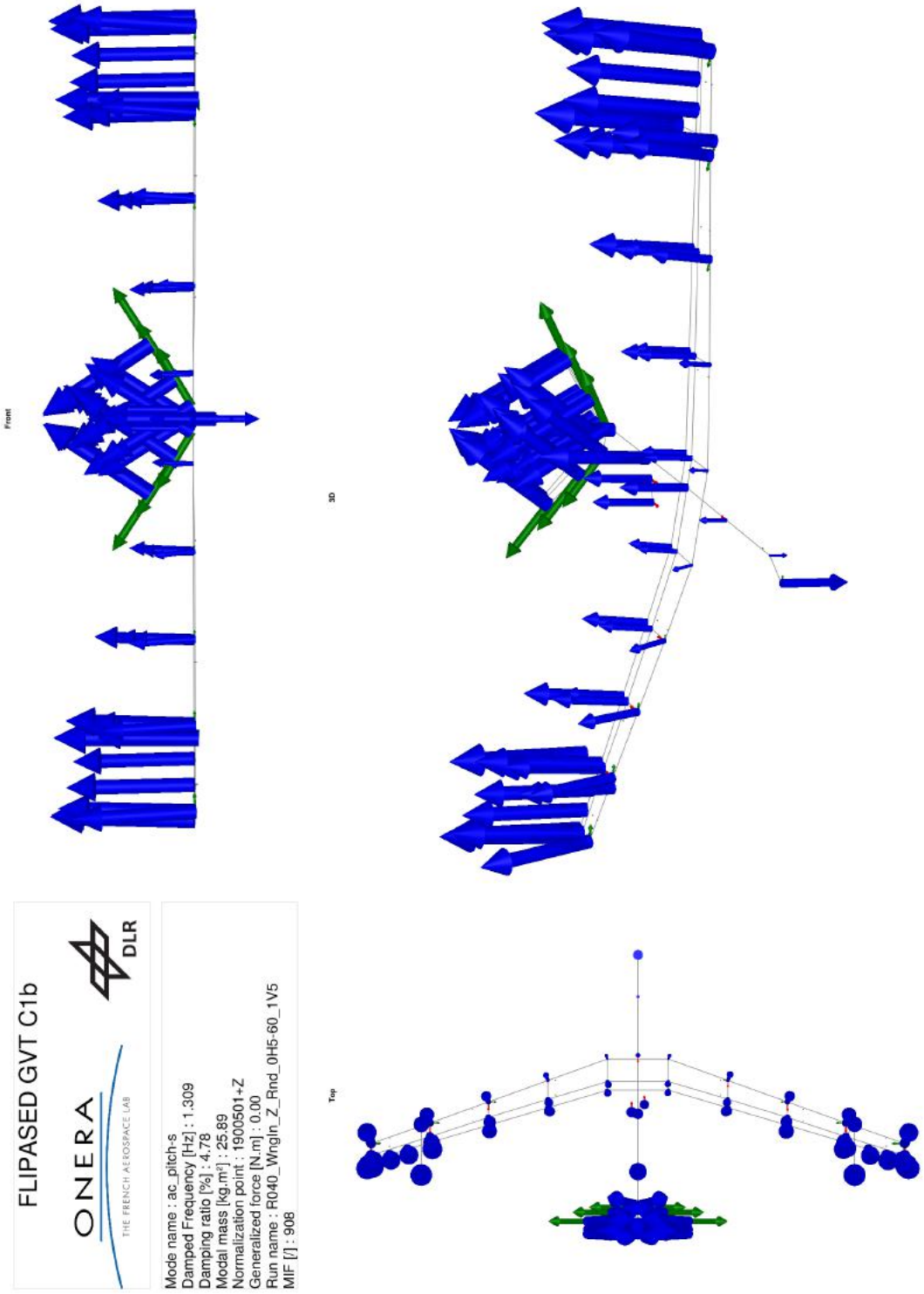

Figure B.28: Mode shape and properties of mode ac_pitch-s identified in C1b.

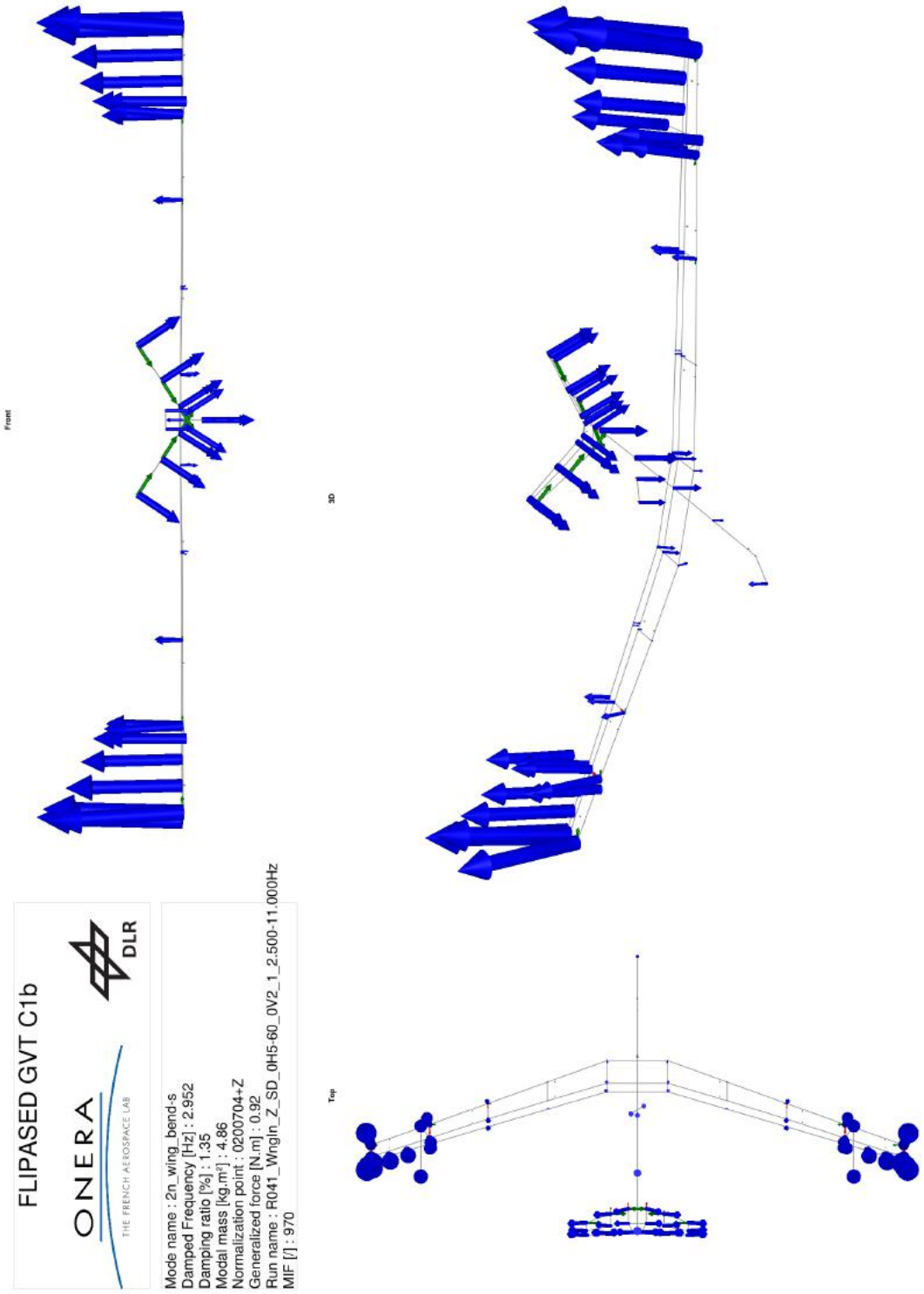

Figure B.29: Mode shape and properties of mode 2n_wing_bend-s identified in C1b.

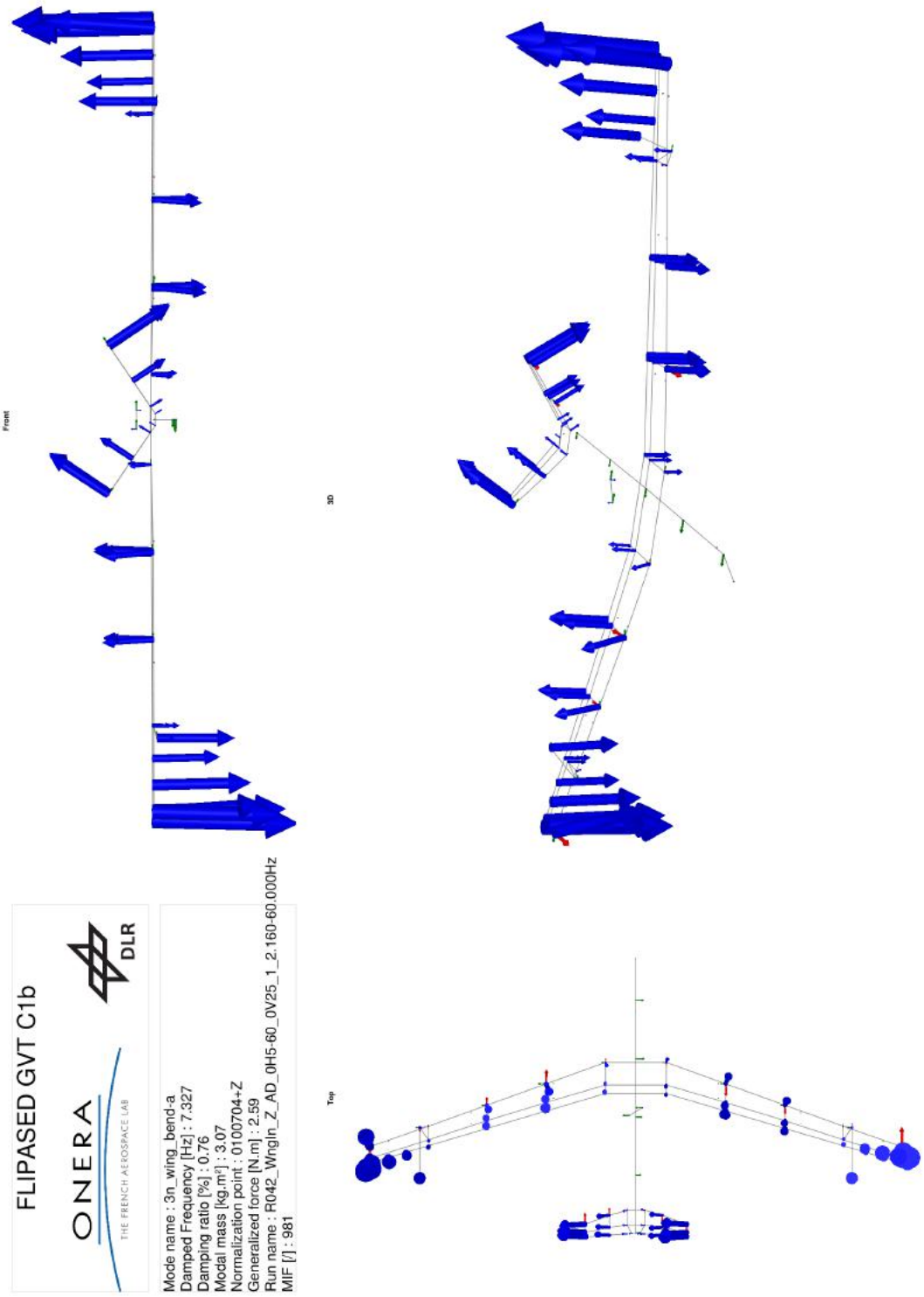

Figure B.30: Mode shape and properties of mode 3n_wing_bend-a identified in C1b.

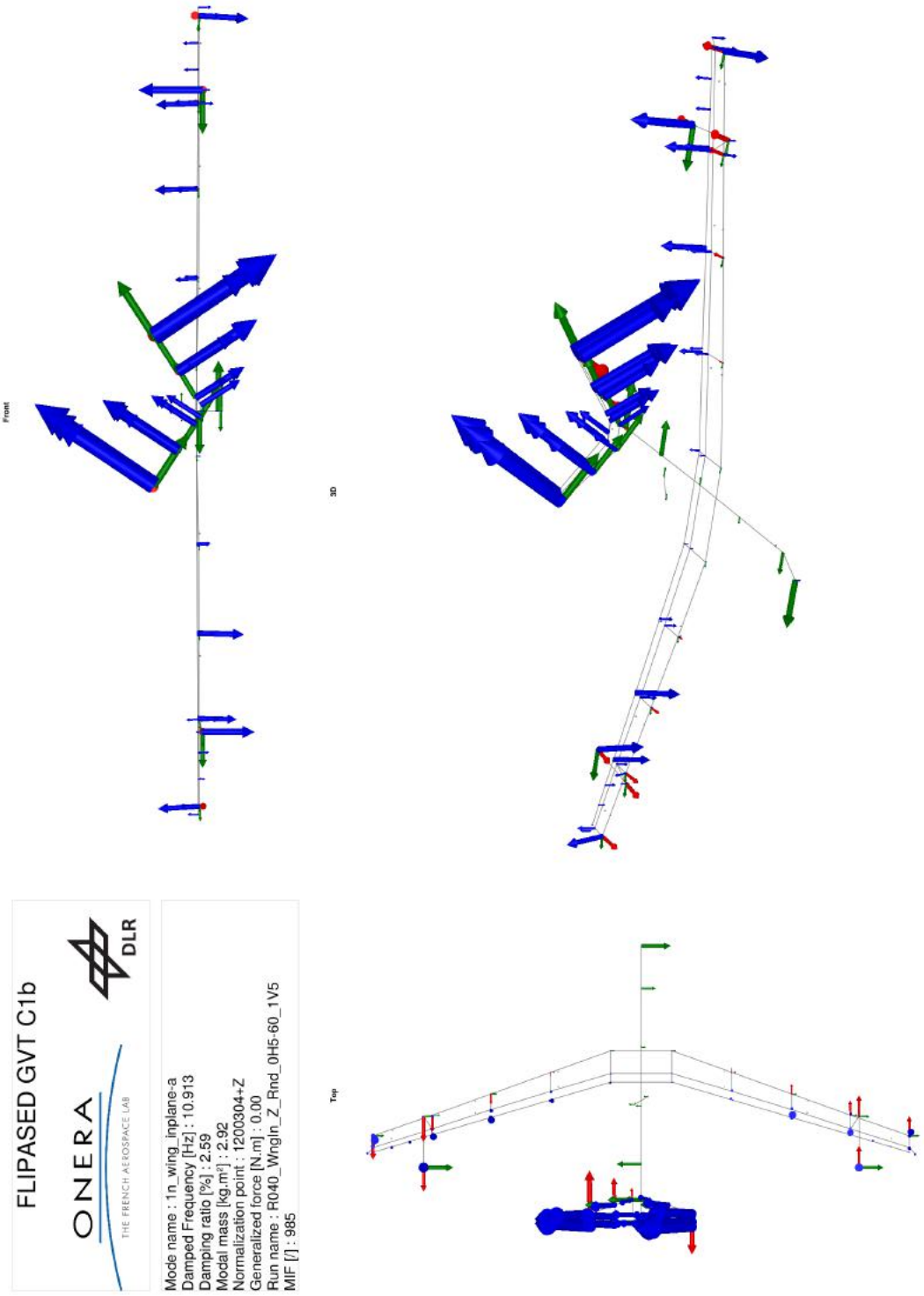

Figure B.31: Mode shape and properties of mode 1n_wing_inplane-a identified in C1b.

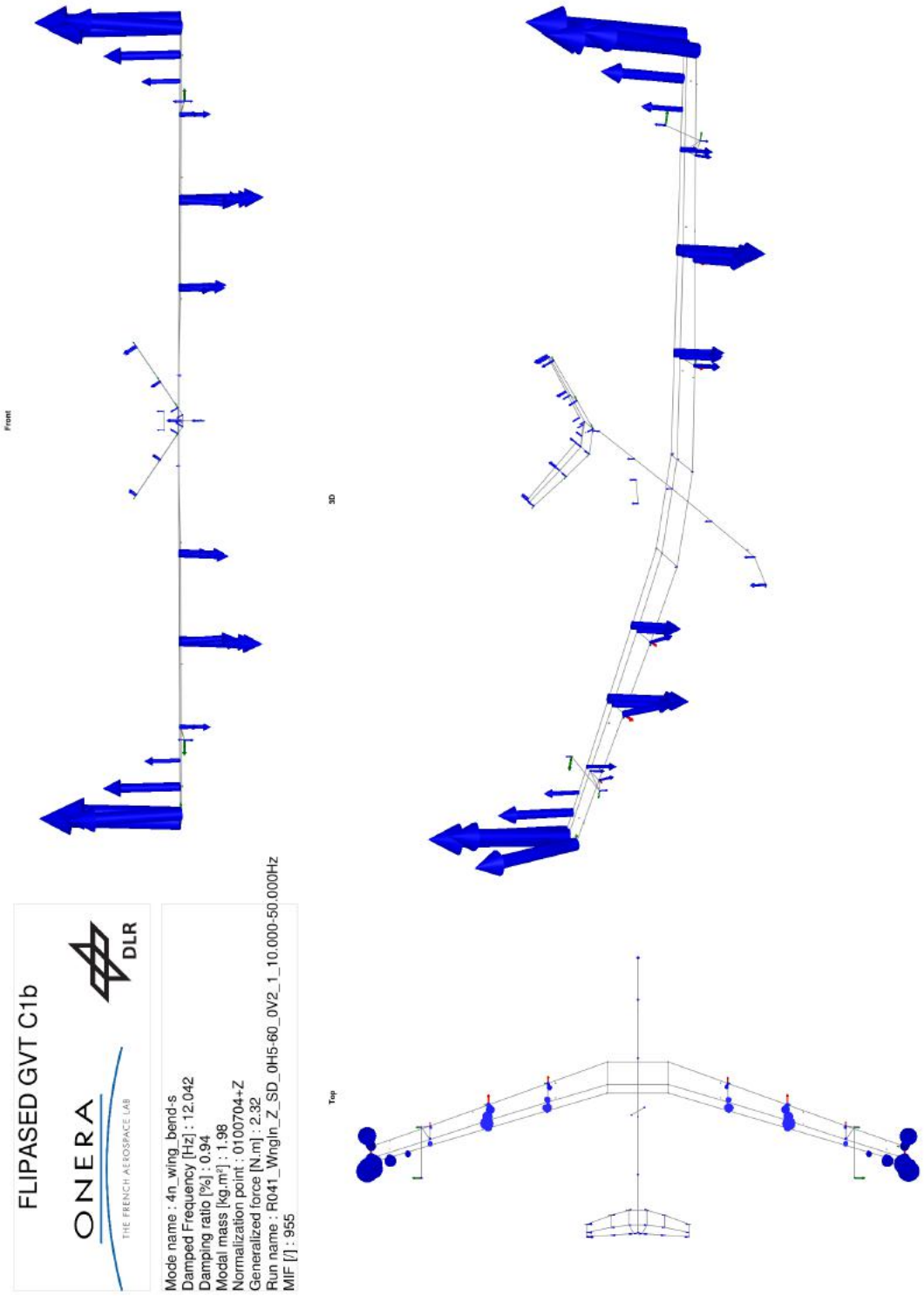

Figure B.32: Mode shape and properties of mode 4n_wing_bend-s identified in C1b.

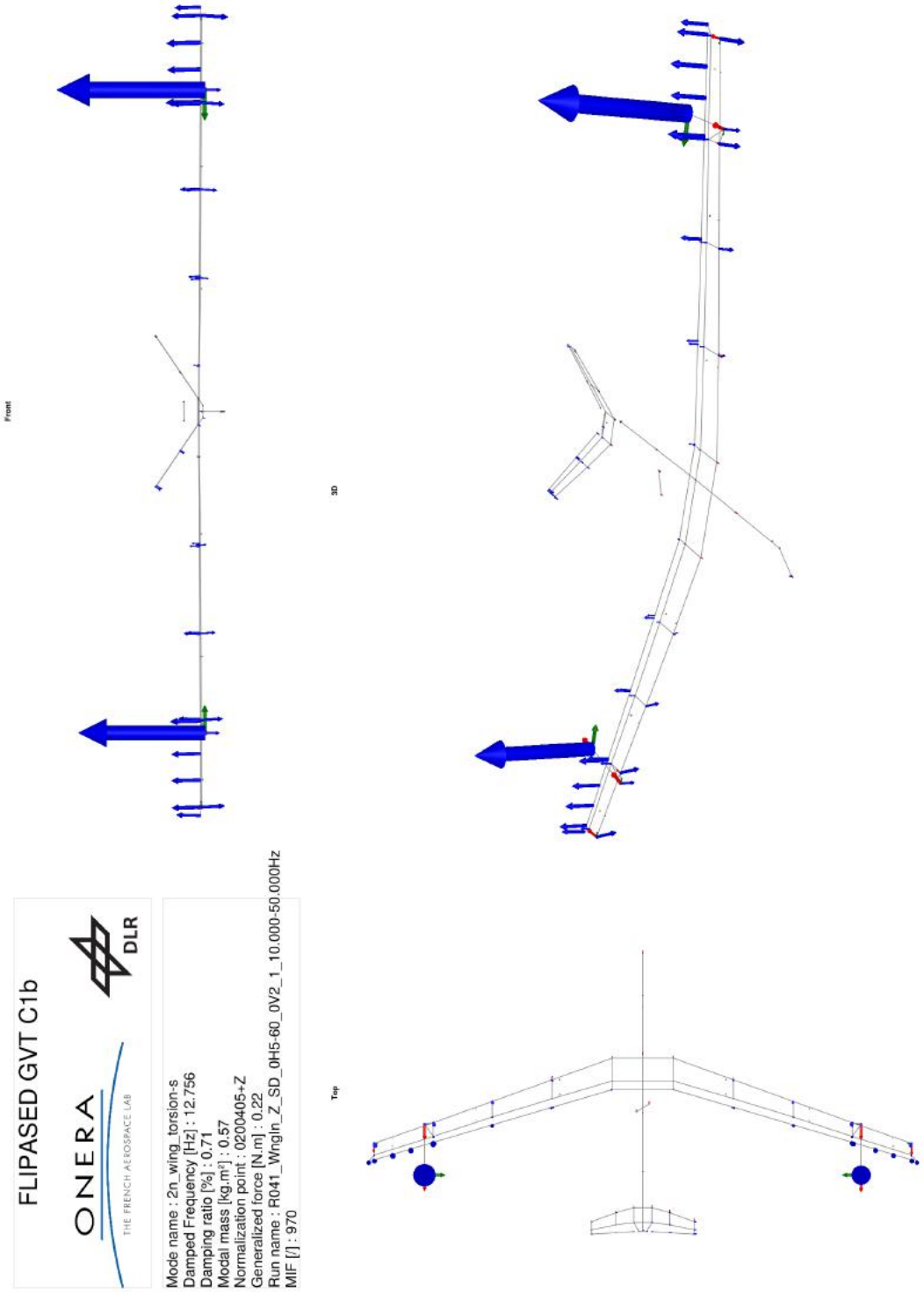

Figure B.33: Mode shape and properties of mode 2n_wing_torsion-s identified in C1b.

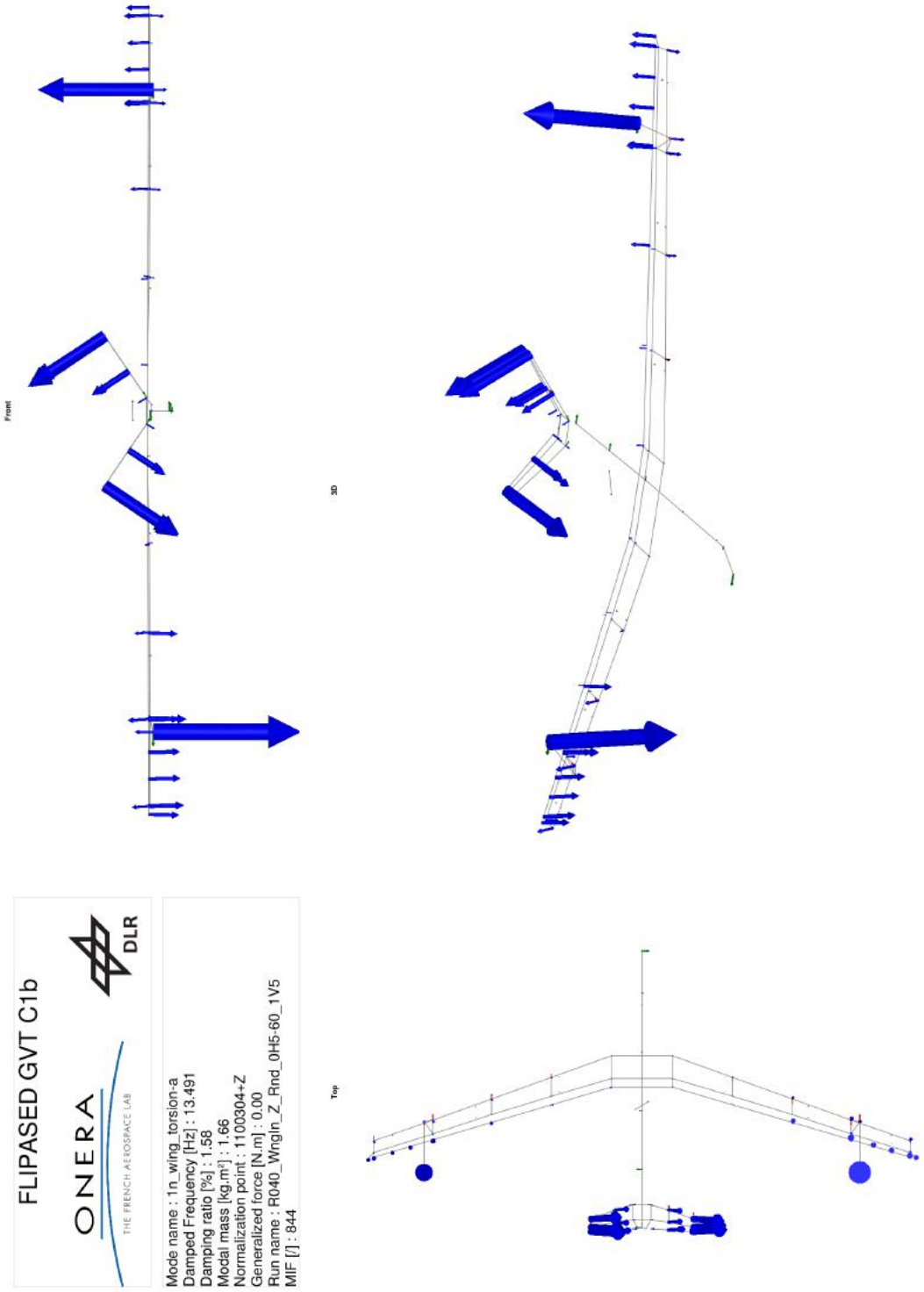

Figure B.34: Mode shape and properties of mode 1n_wing_torsion-a identified in C1b.

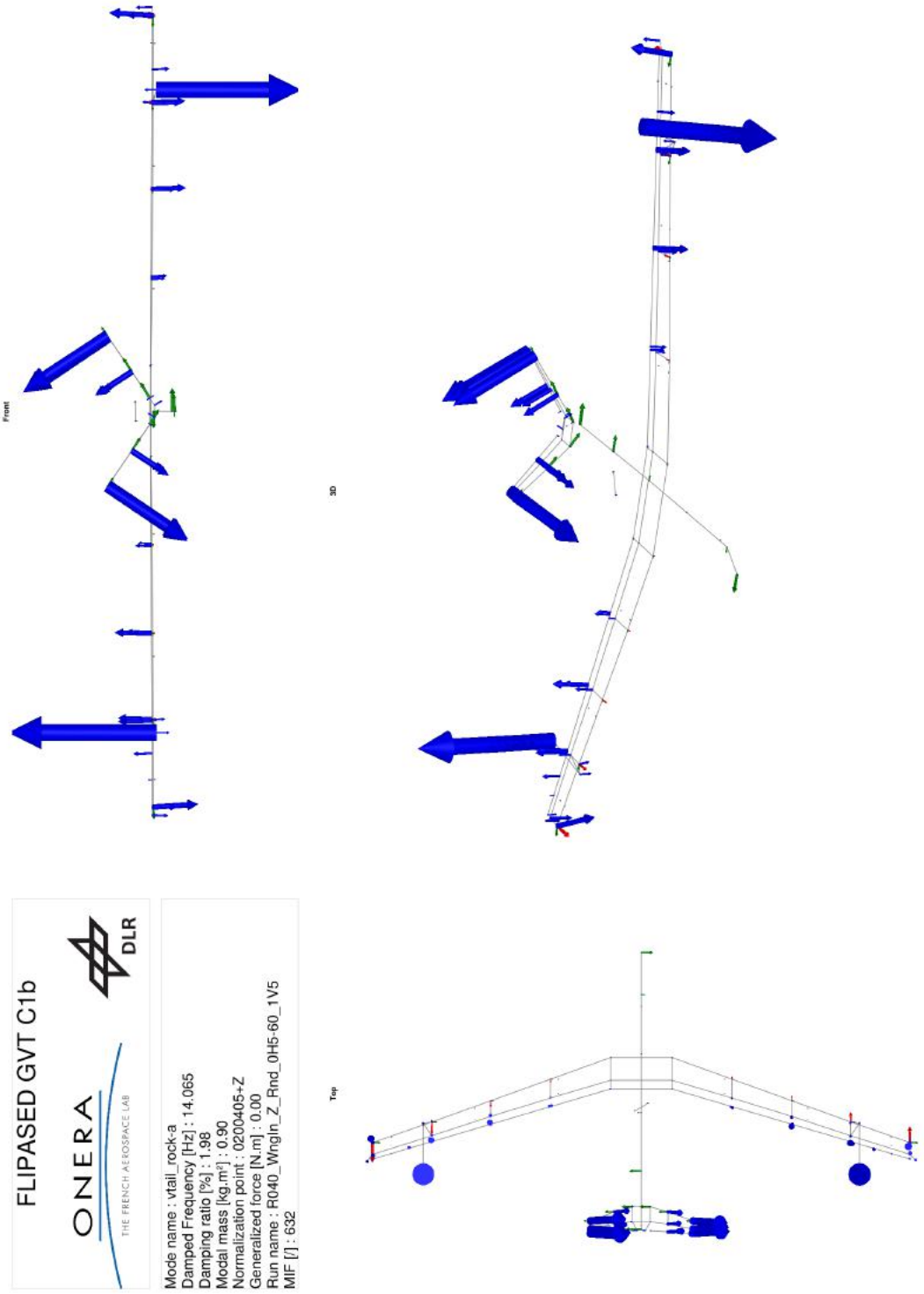

Figure B.35: Mode shape and properties of mode vtail_rock-a identified in C1b.

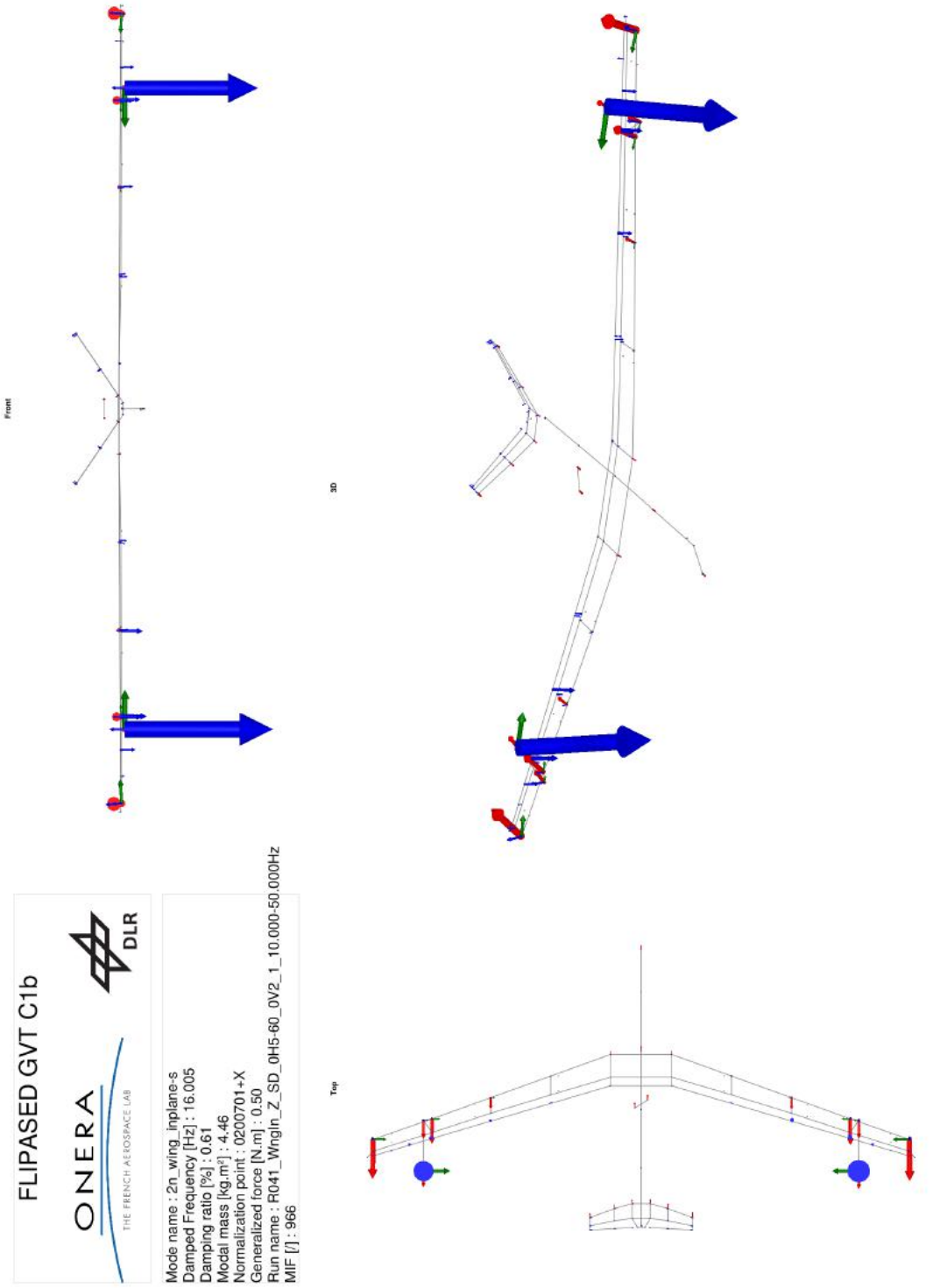

Figure B.36: Mode shape and properties of mode 2n_wing_inplane-s identified in C1b.

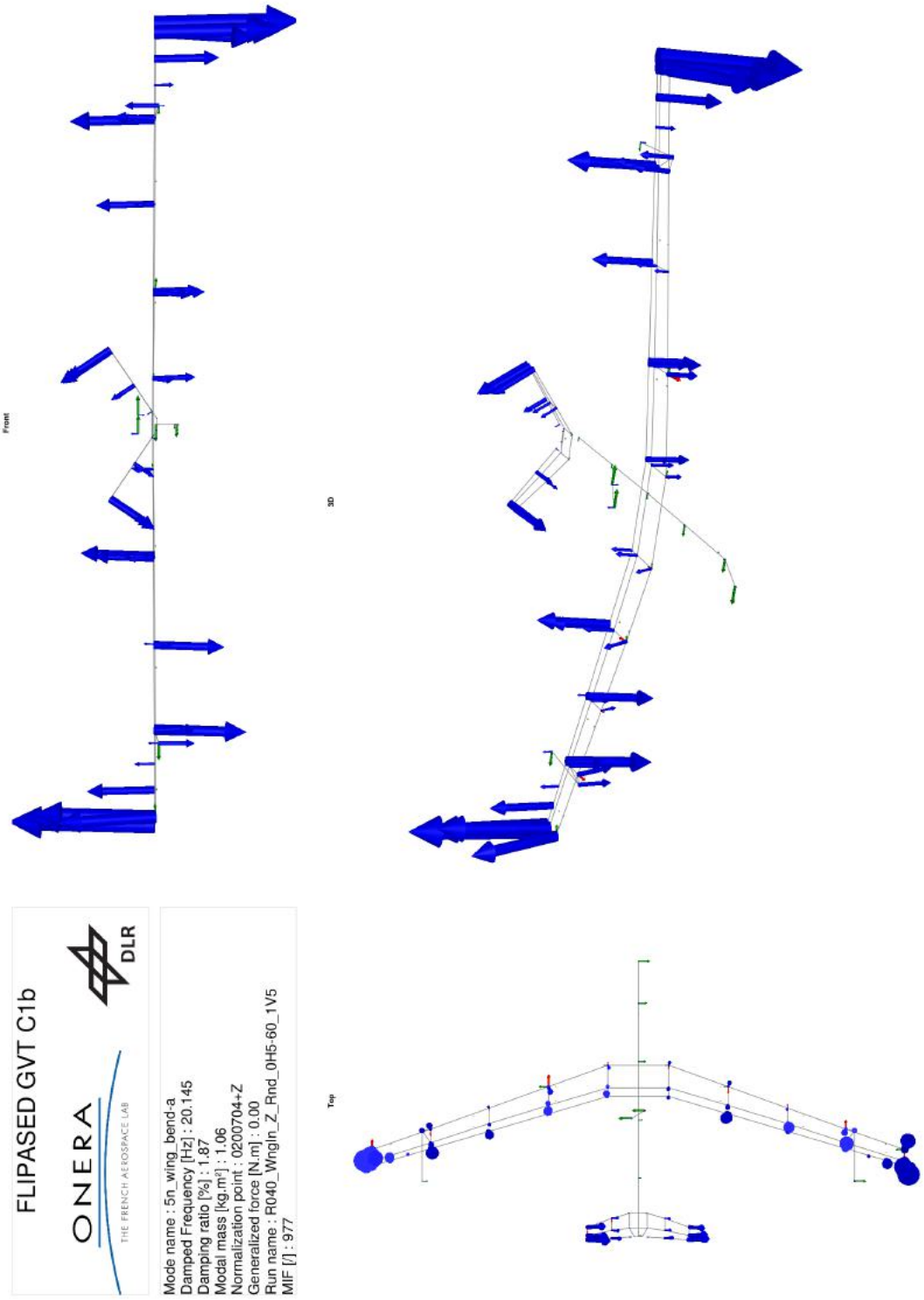

Figure B.37: Mode shape and properties of mode 5n_wing_bend-a identified in C1b.

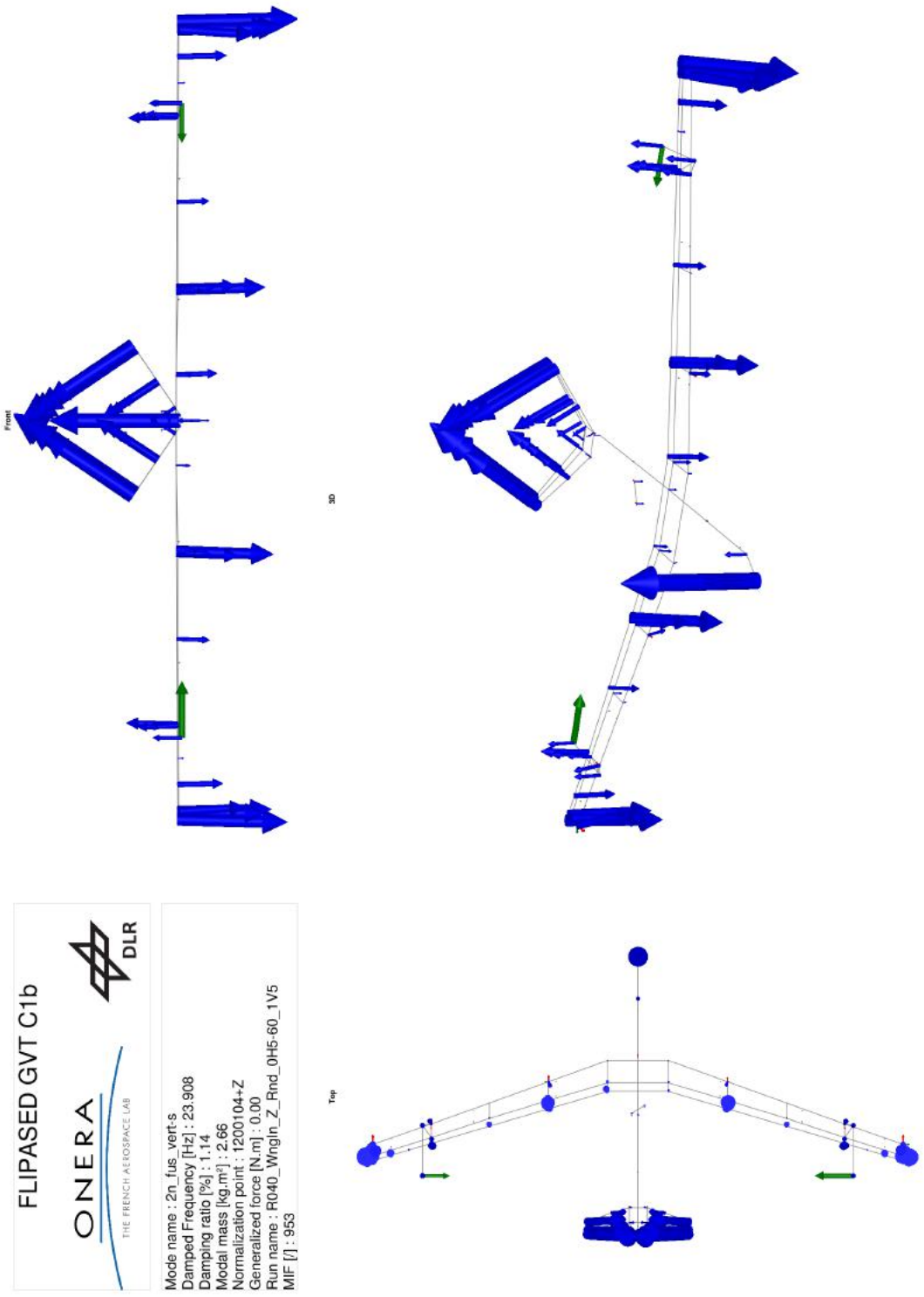

Figure B.38: Mode shape and properties of mode 2n_fus_vert-s identified in C1b.

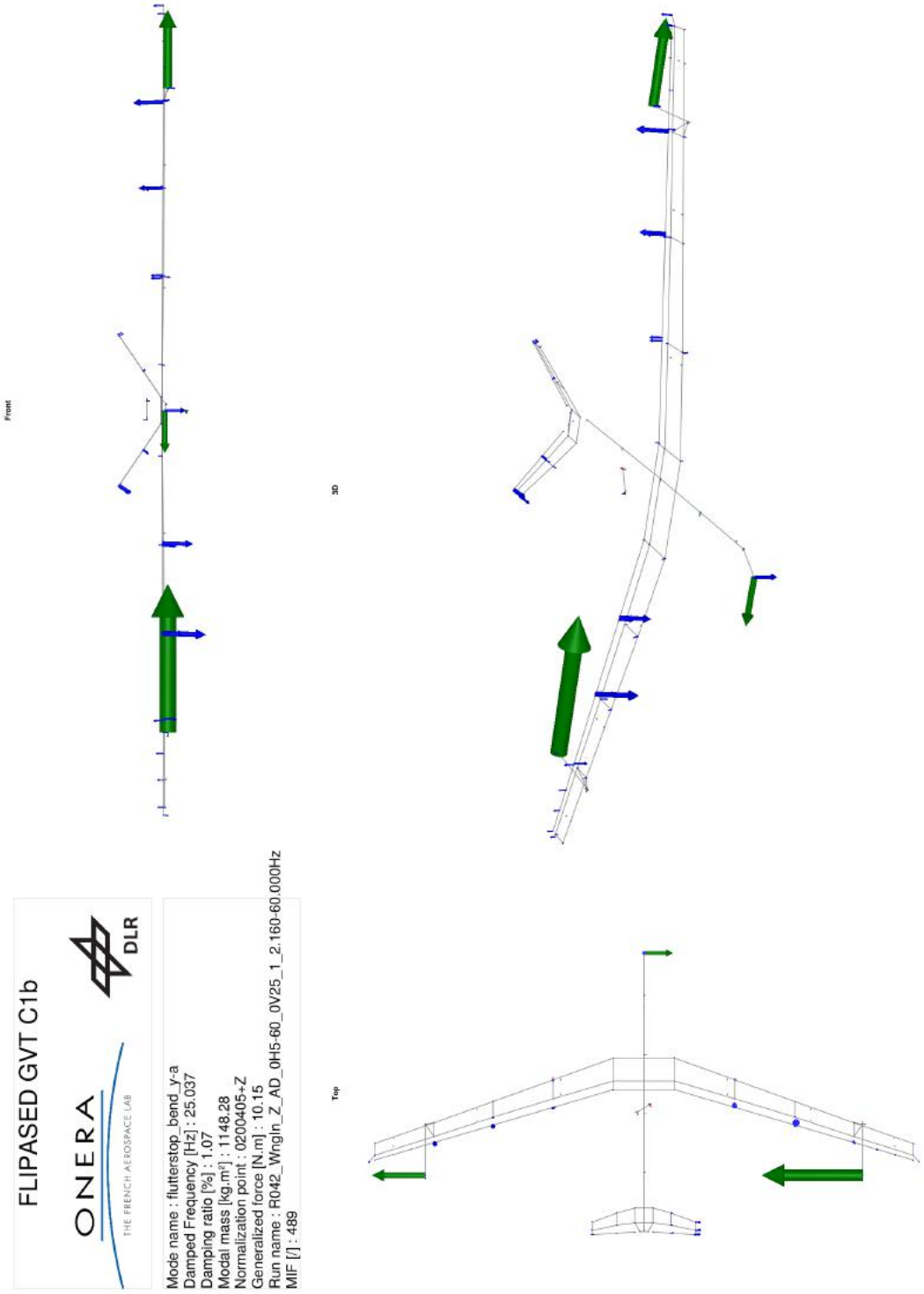

Figure B.39: Mode shape and properties of mode flutterstop_bend_y-a identified in C1b.

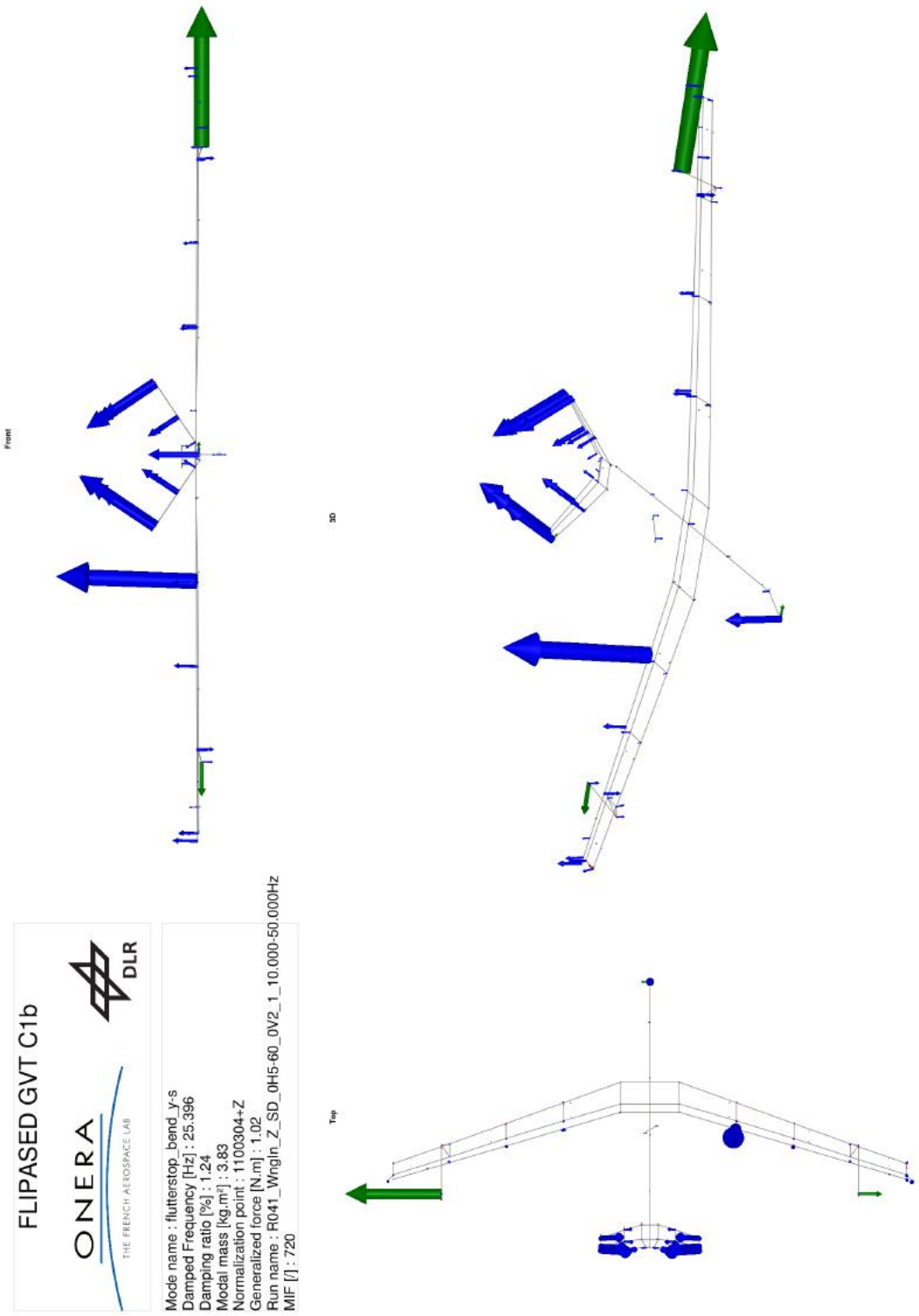

Figure B.40: Mode shape and properties of mode flutterstop_bend_y-s identified in C1b.

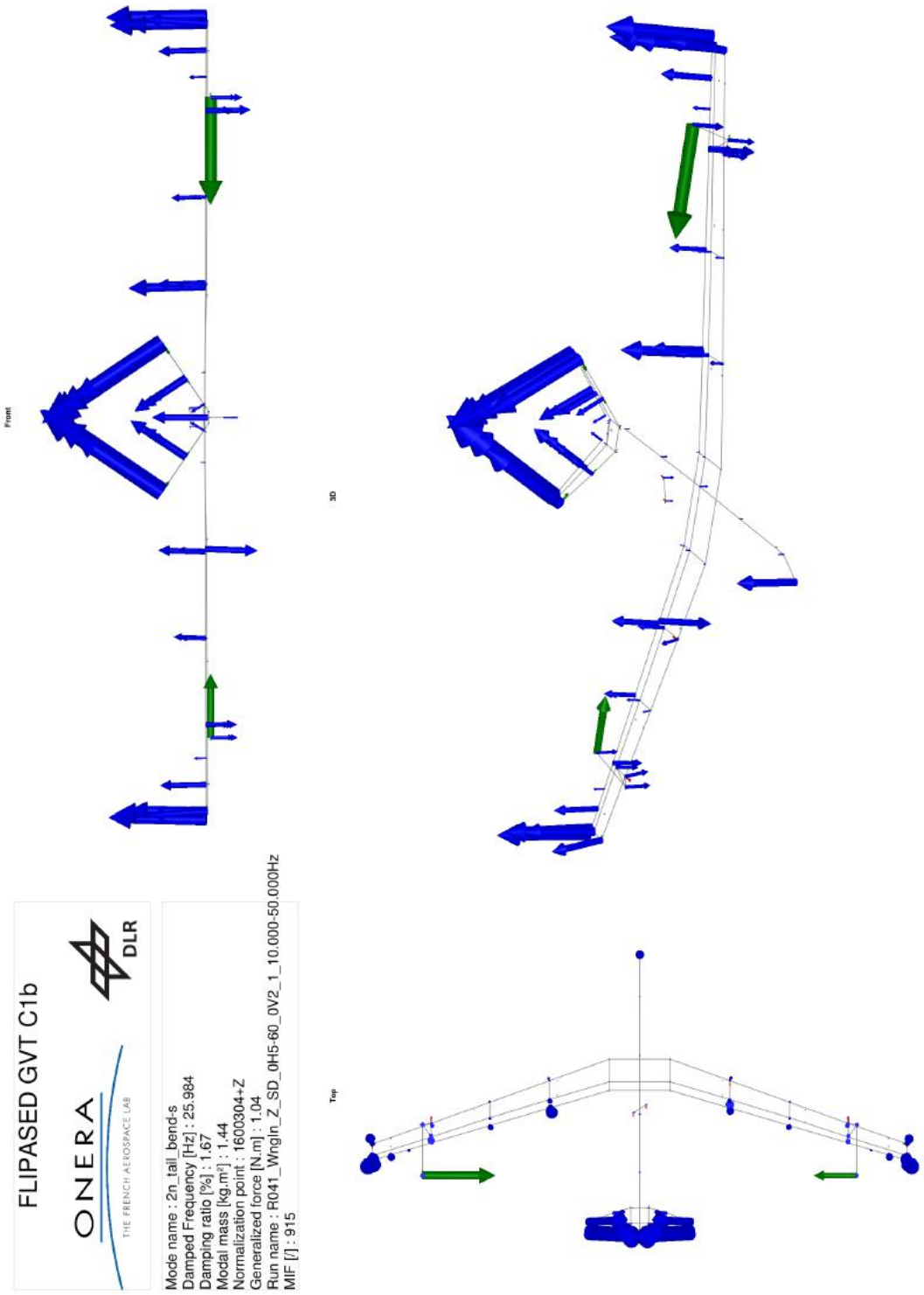

Figure B.41: Mode shape and properties of mode 2n_tail_bend-s identified in C1b.

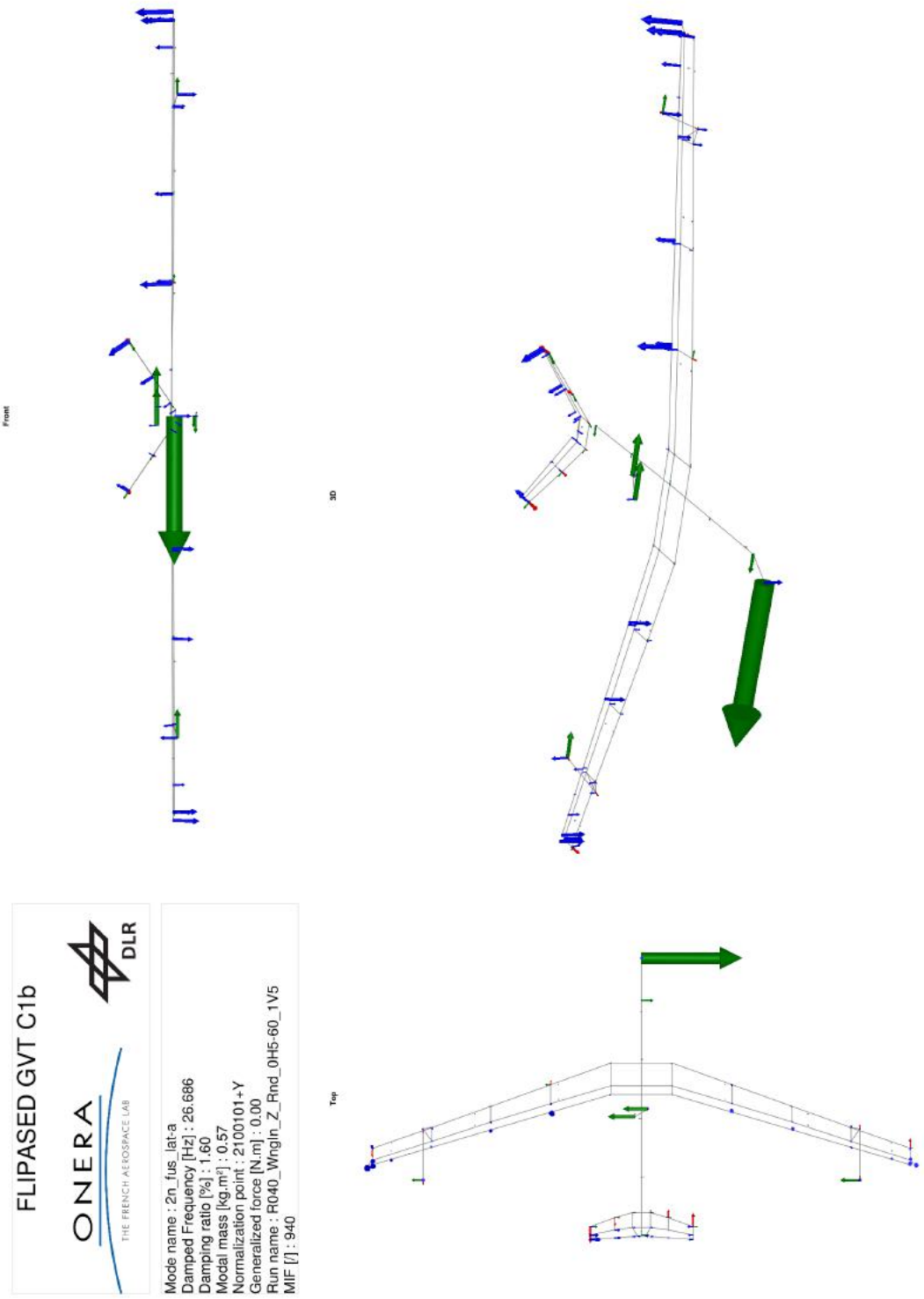

Figure B.42: Mode shape and properties of mode 2n_fus_lat-a identified in C1b.

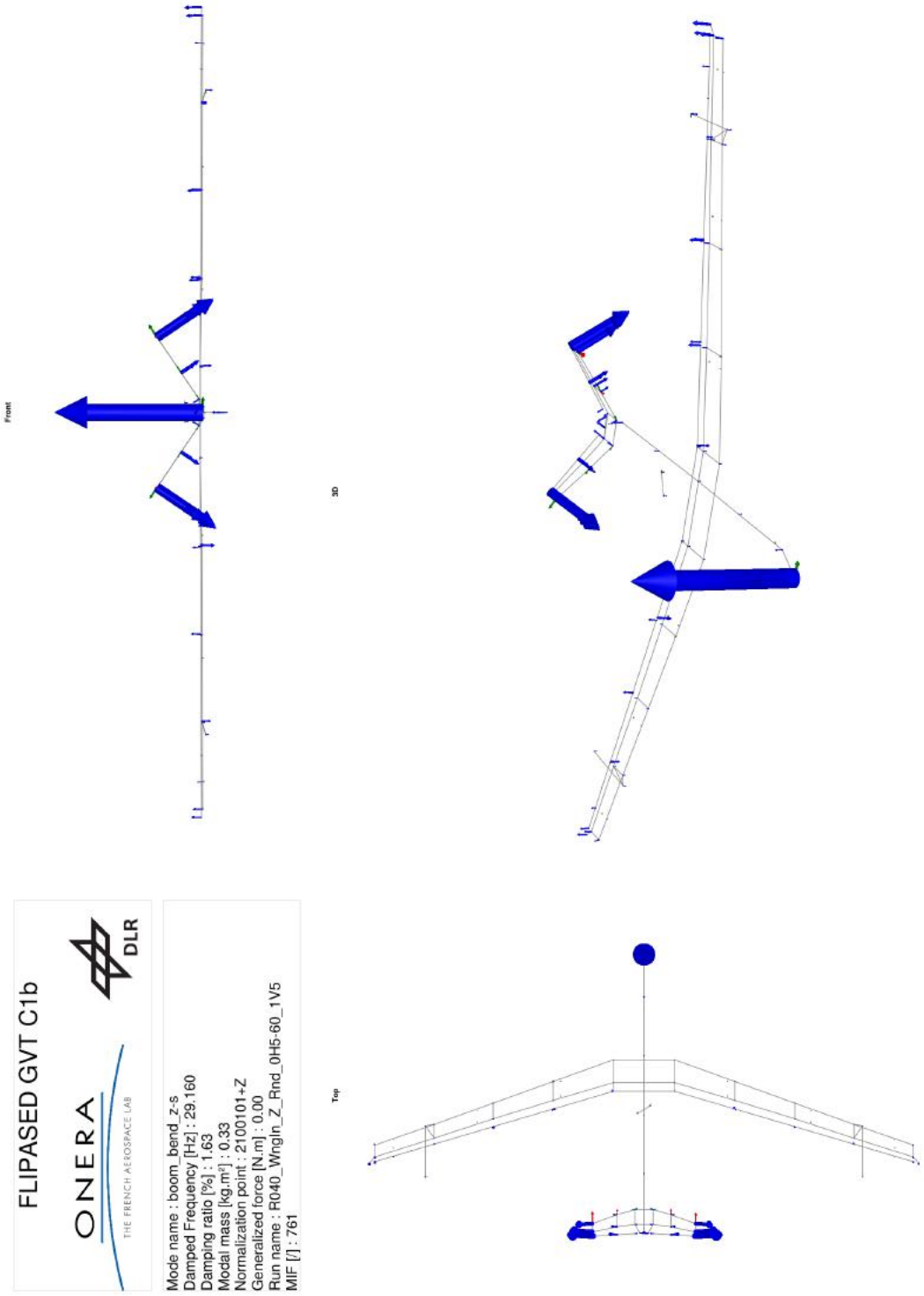

Figure B.43: Mode shape and properties of mode boom_bend_z-s identified in C1b.

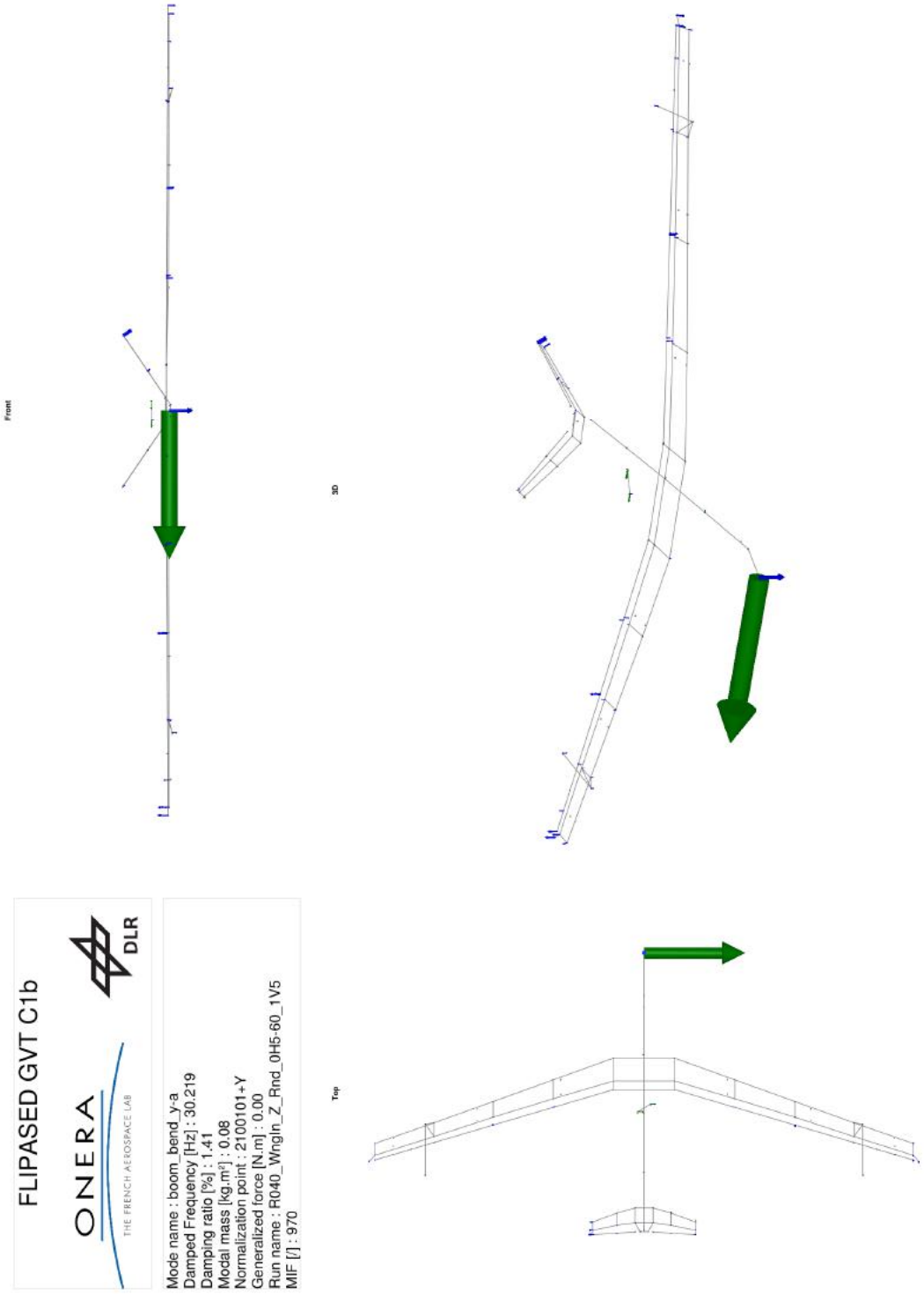

Figure B.44: Mode shape and properties of mode boom_bend_y-a identified in C1b.

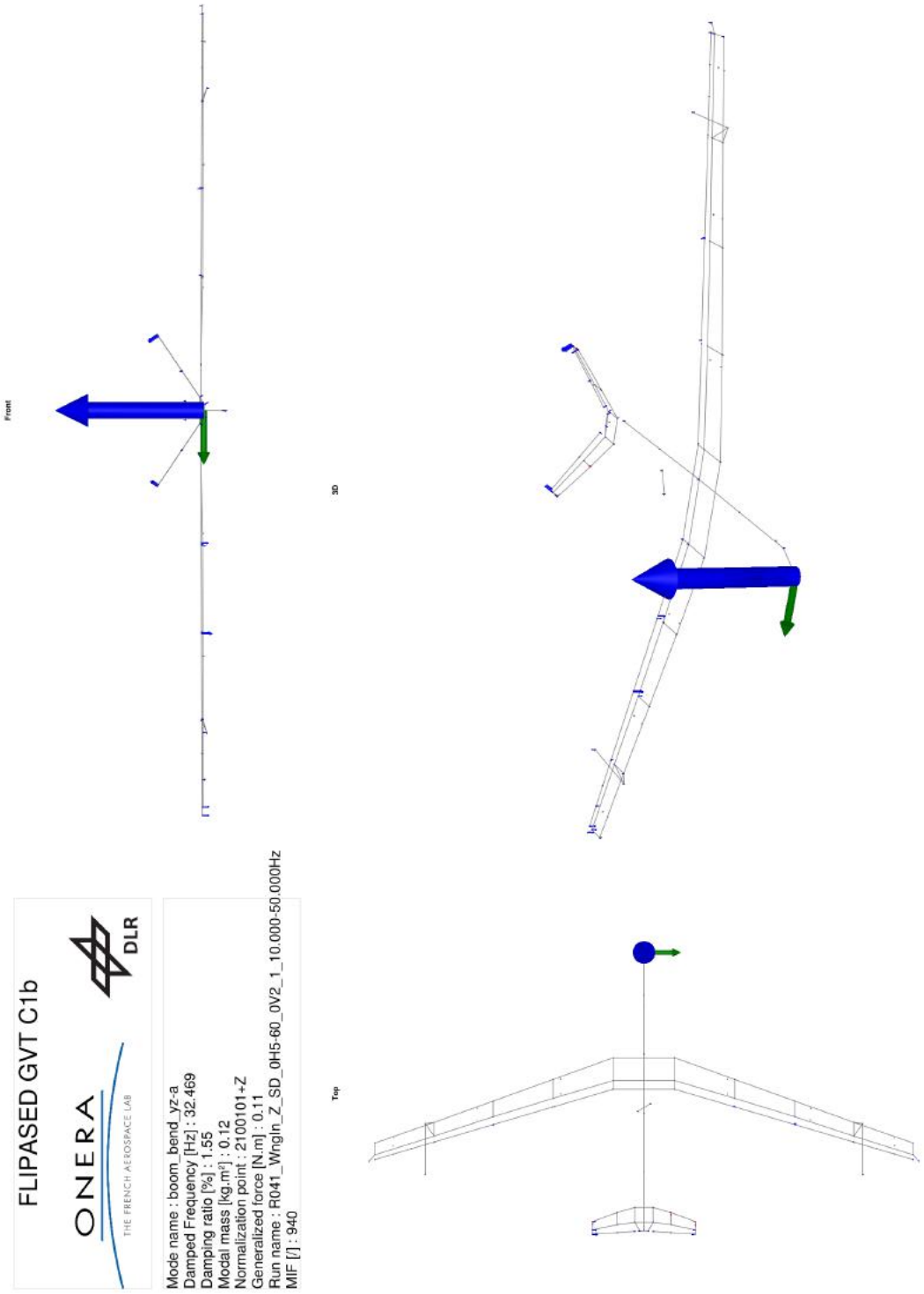

Figure B.45: Mode shape and properties of mode boom_bend_yz-a identified in C1b.

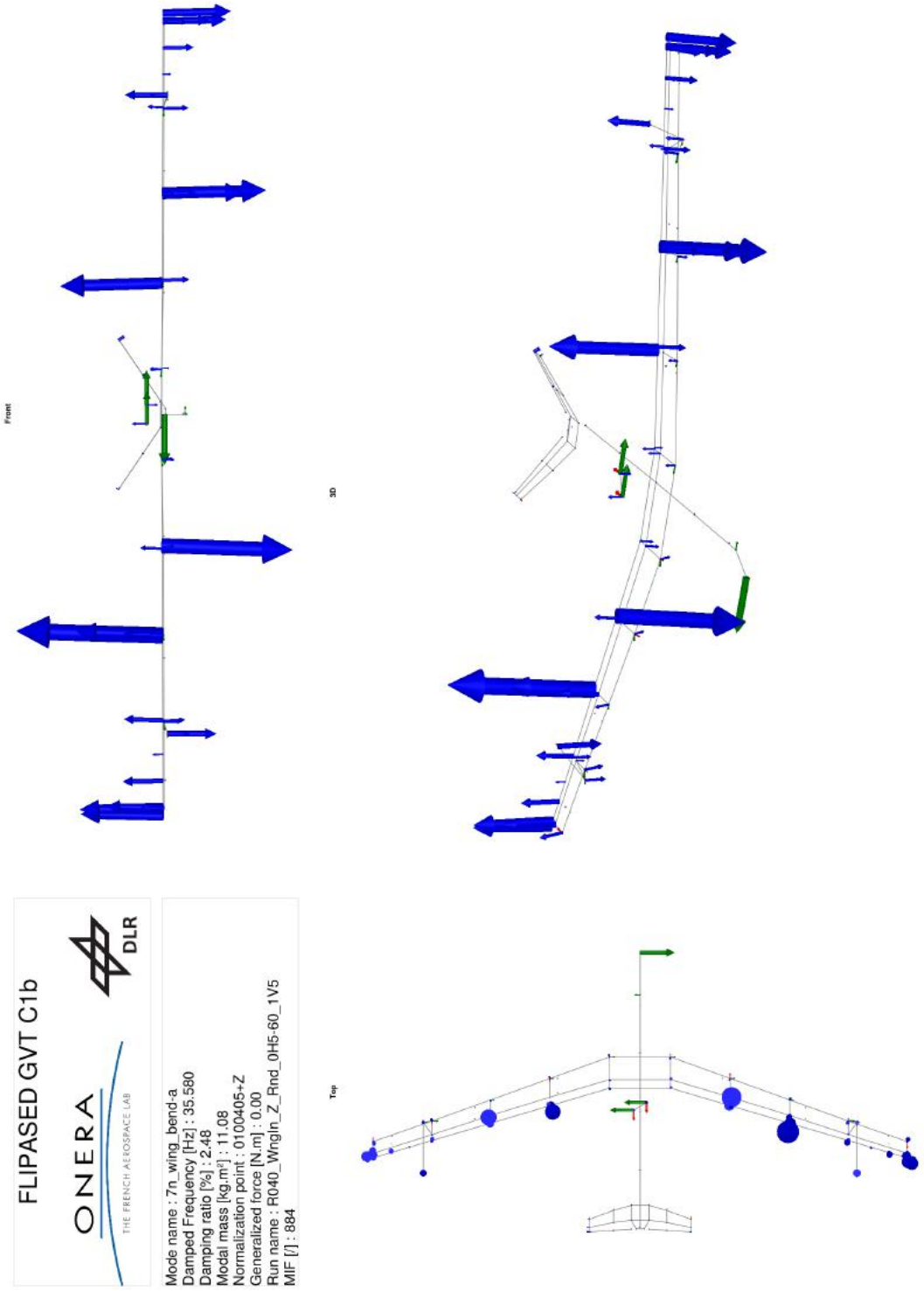

Figure B.46: Mode shape and properties of mode 7n_wing_bend-a identified in C1b.

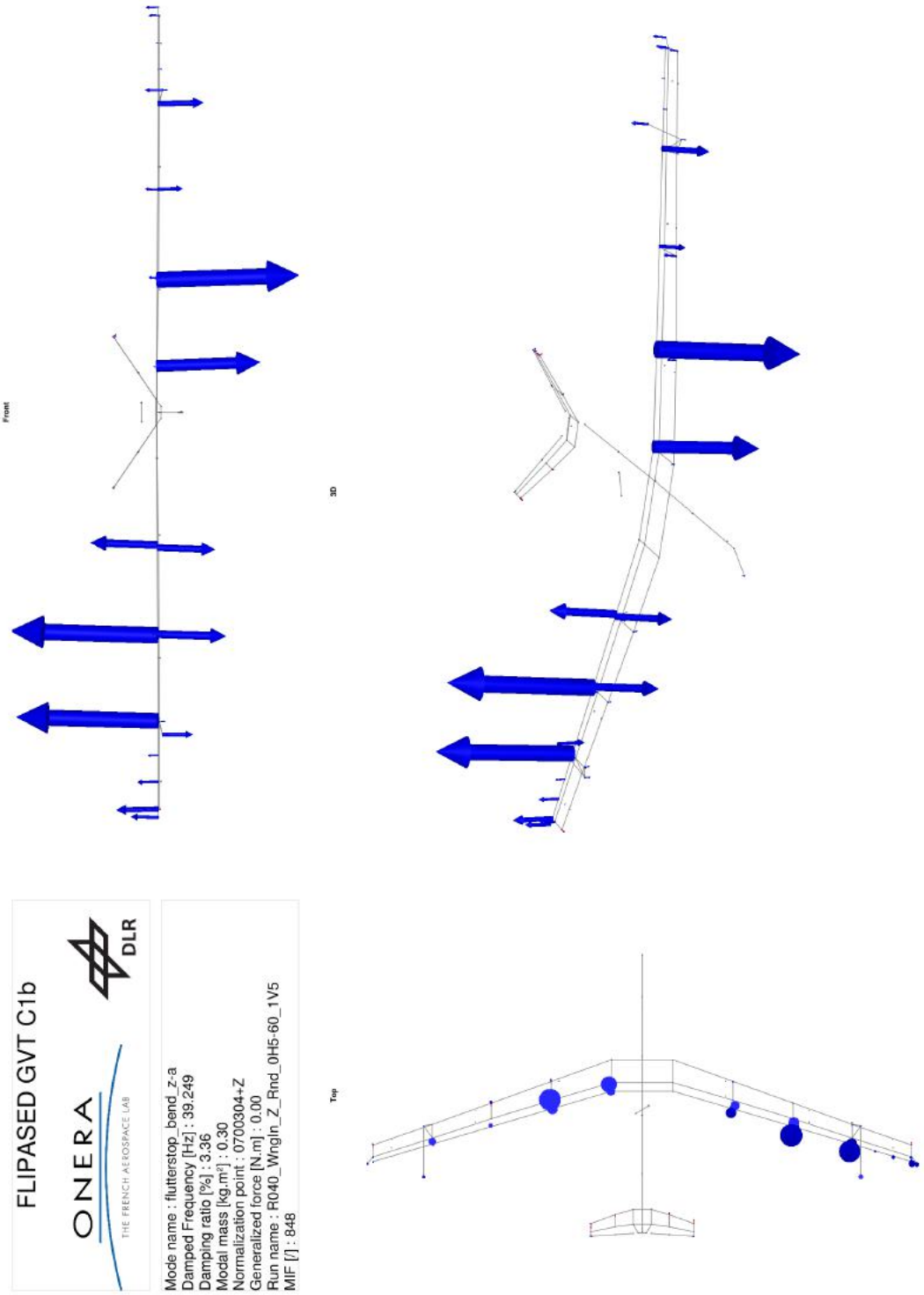

Figure B.47: Mode shape and properties of mode flutterstop_bend_z-a identified in C1b.

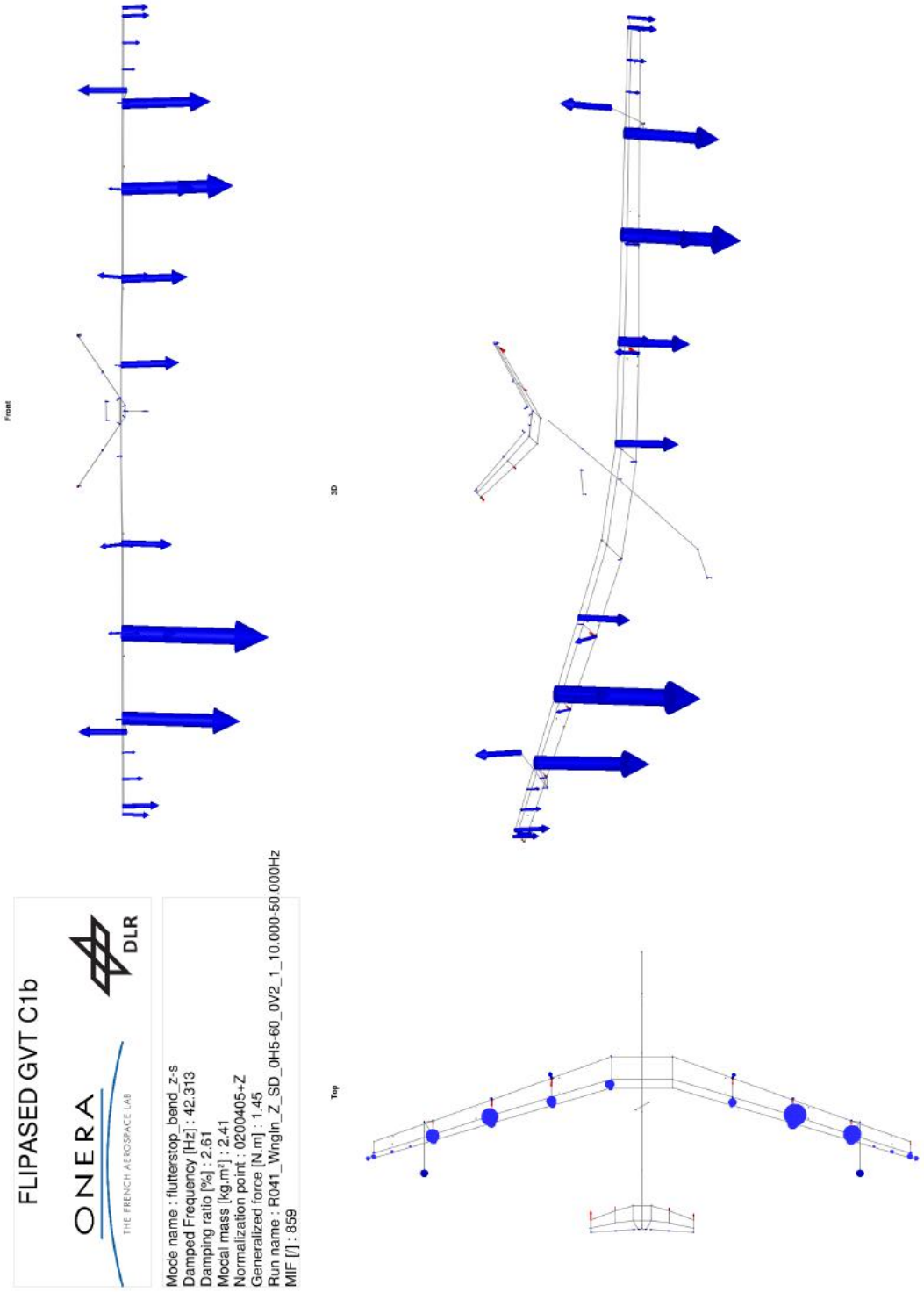

Figure B.48: Mode shape and properties of mode flutterstop_bend_z-s identified in C1b.

3 Configuration C1d

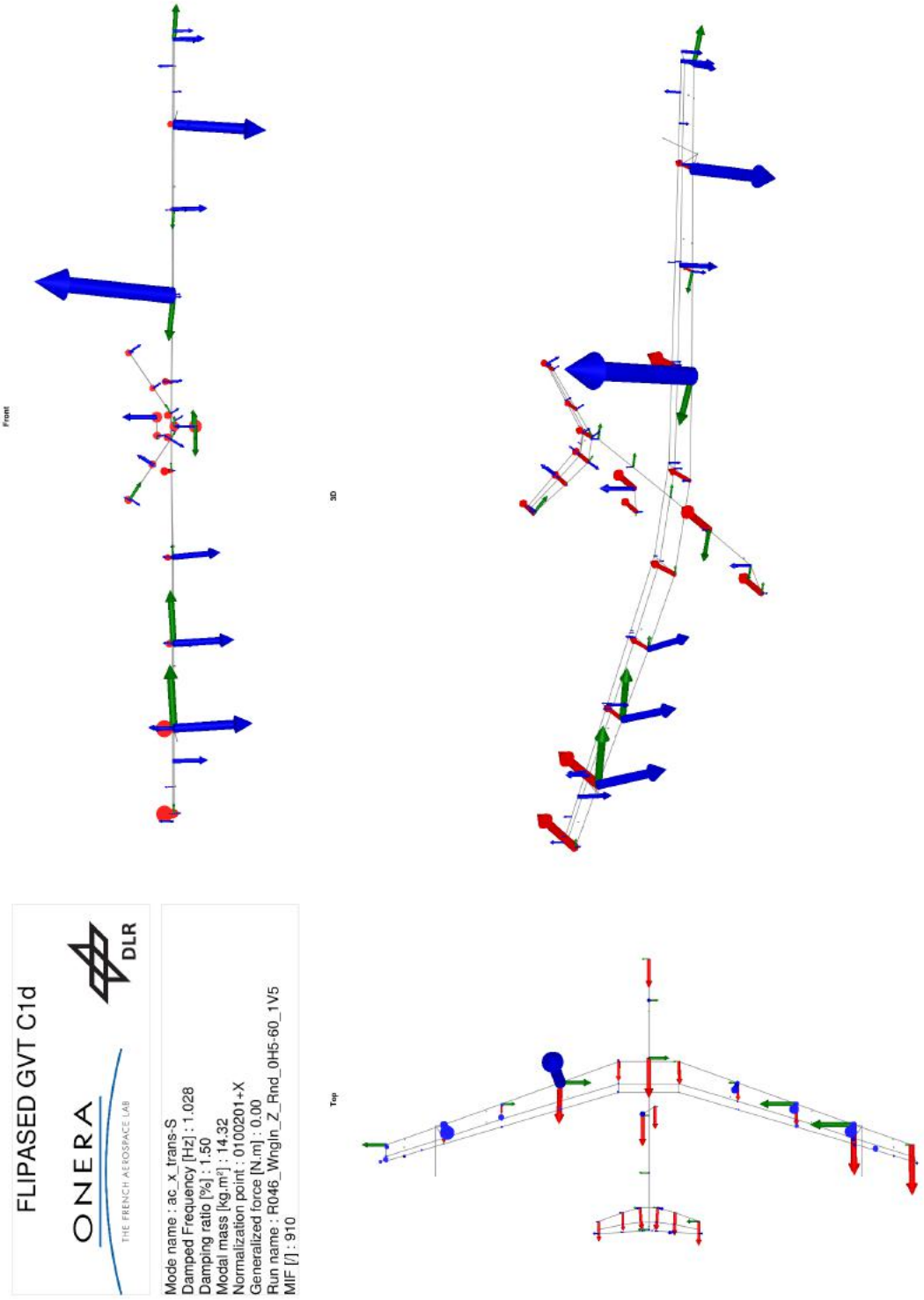

Figure B.49: Mode shape and properties of mode ac_x_trans-S identified in C1d.

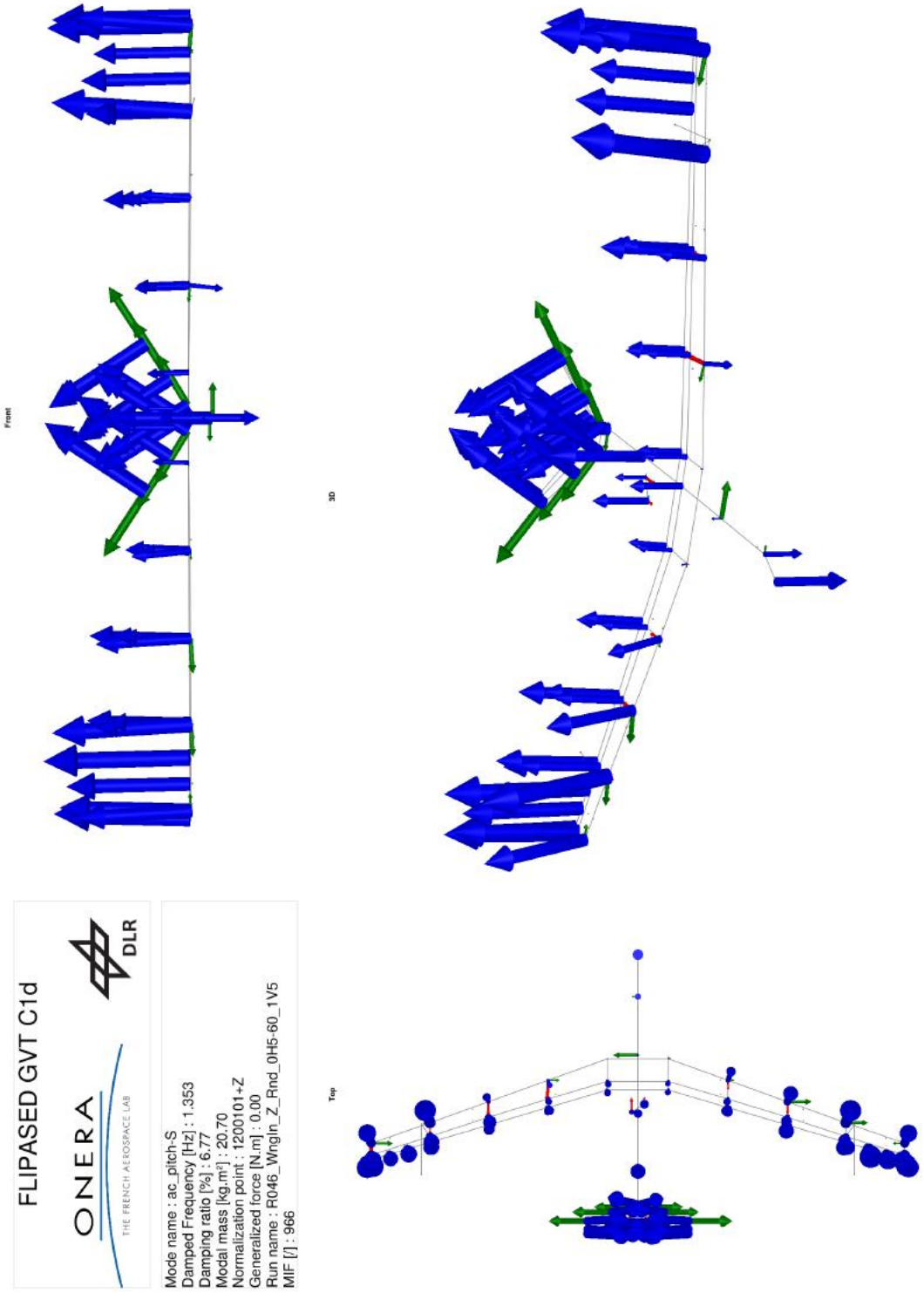

Figure B.50: Mode shape and properties of mode ac_pitch-S identified in C1d.

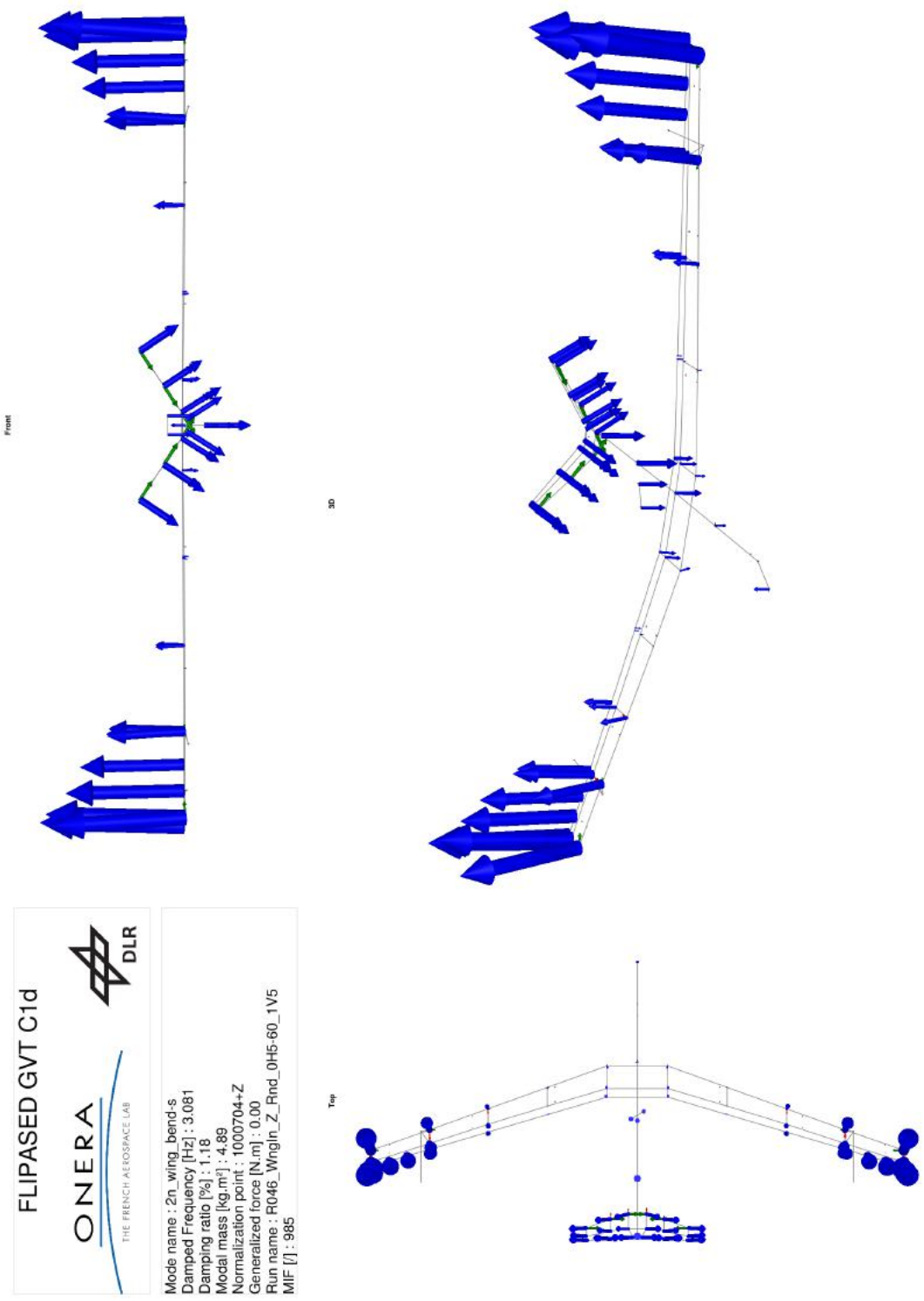

Figure B.51: Mode shape and properties of mode 2n_wing_bend-s identified in C1d.

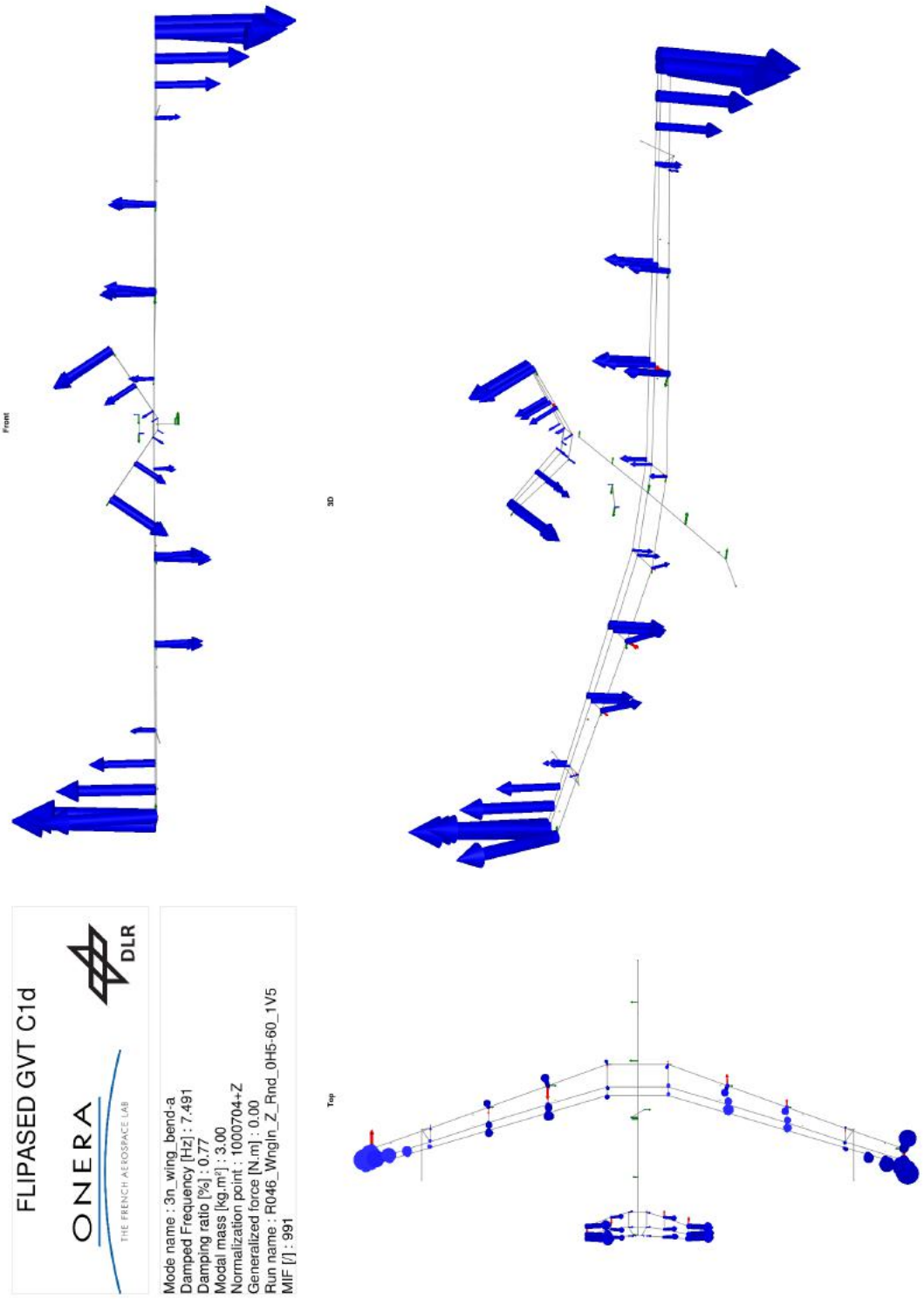

Figure B.52: Mode shape and properties of mode 3n_wing_bend-a identified in C1d.

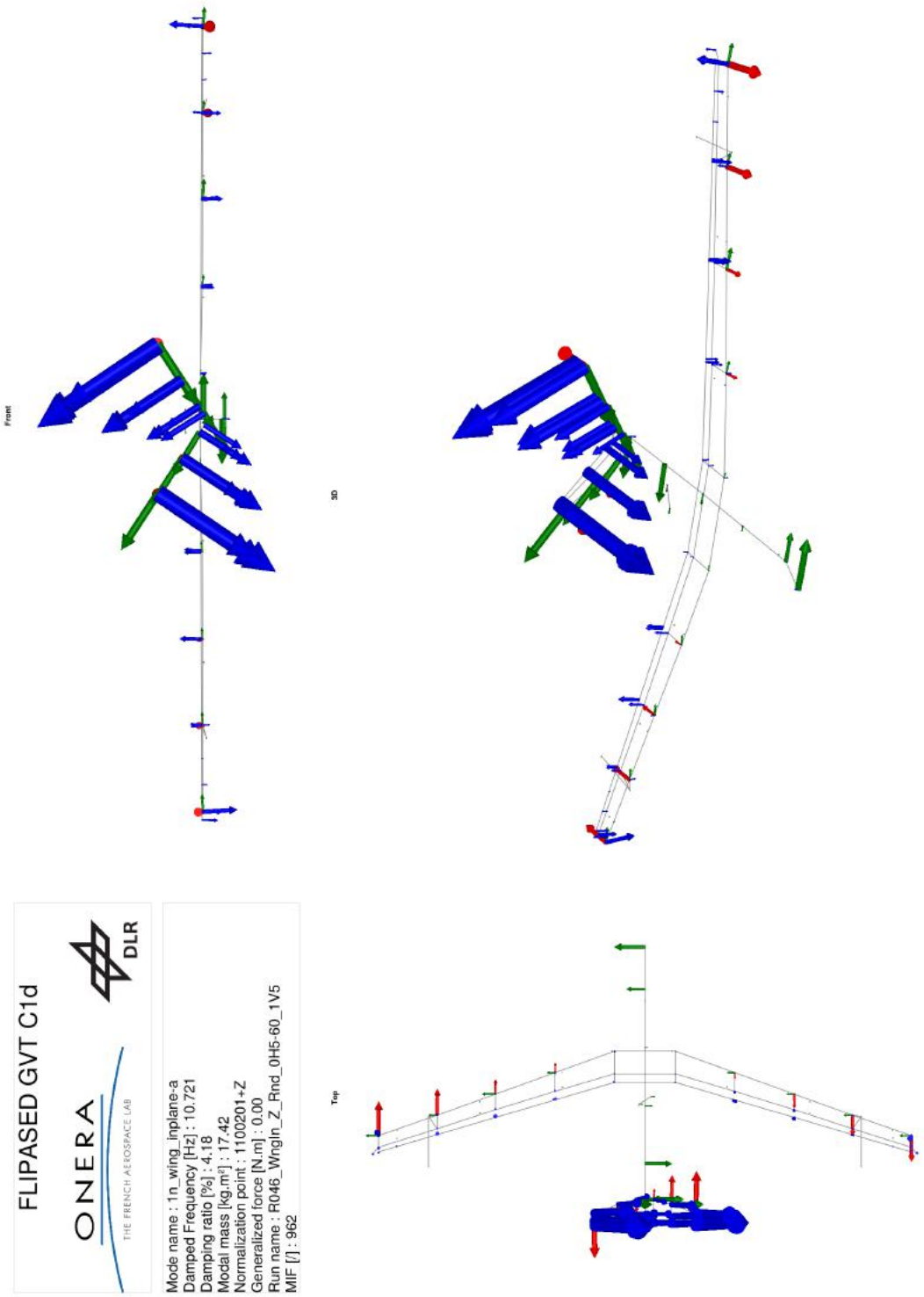

Figure B.53: Mode shape and properties of mode 1n_wing_inplane-a identified in C1d.

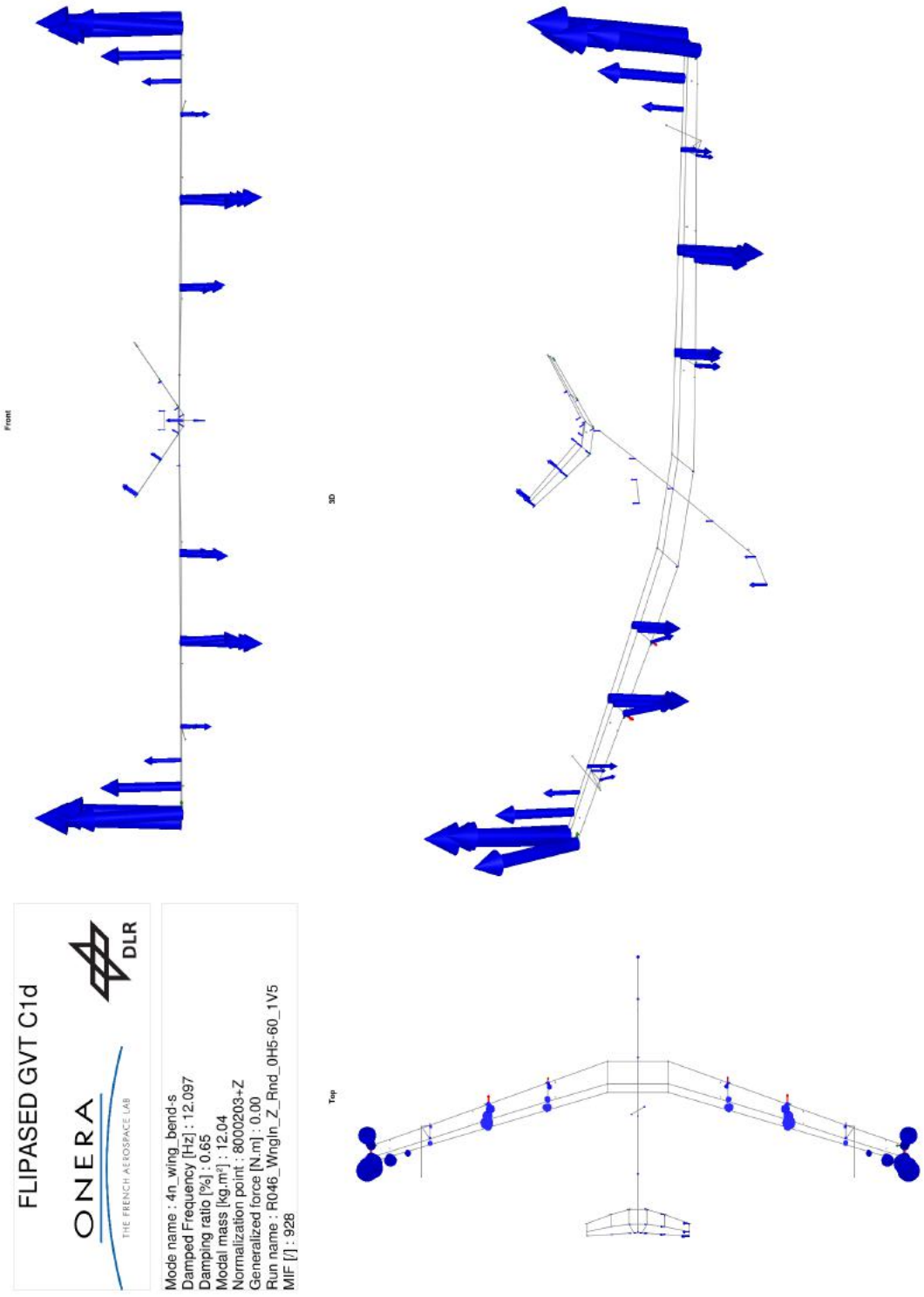

Figure B.54: Mode shape and properties of mode 4n_wing_bend-s identified in C1d.

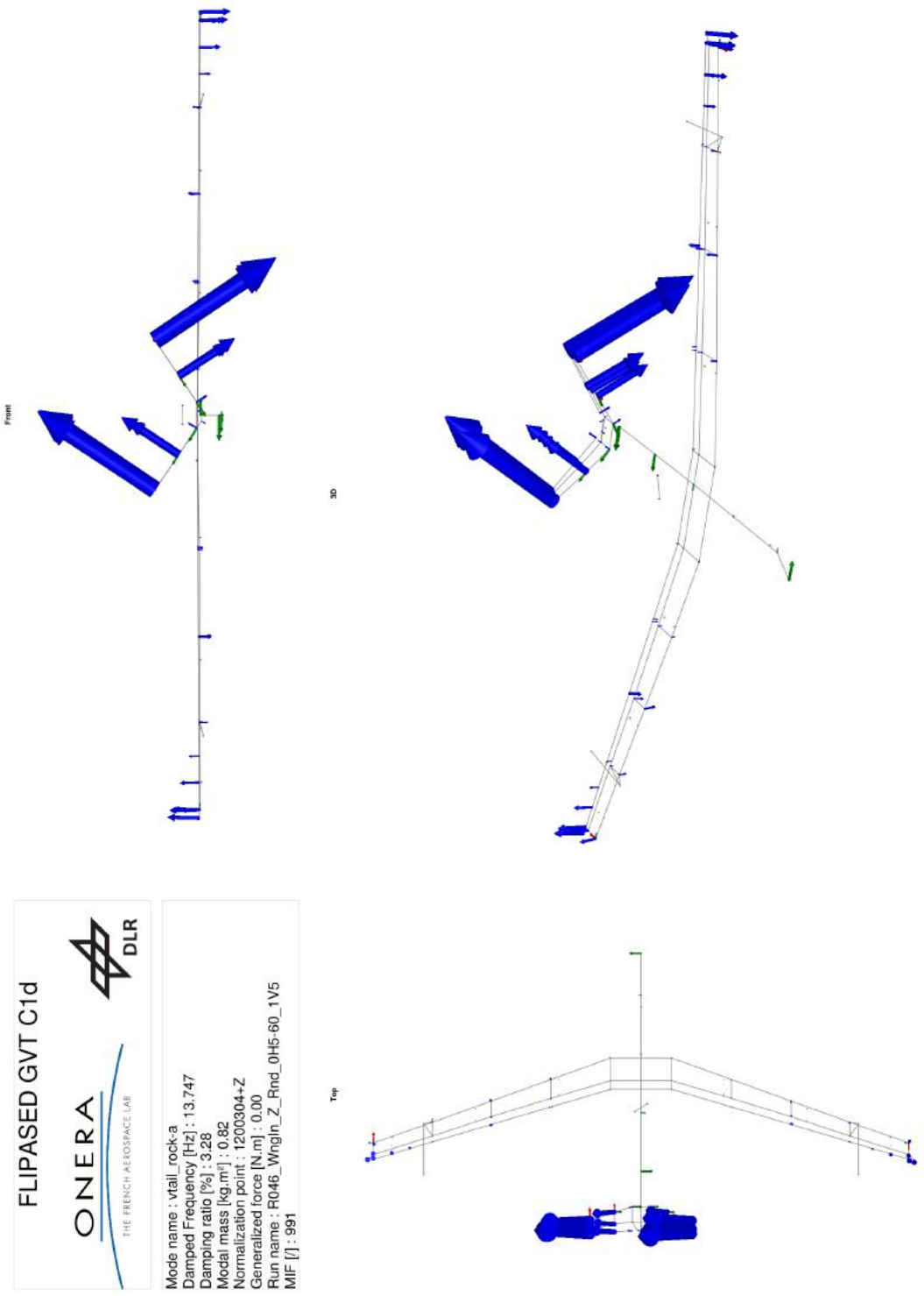

Figure B.55: Mode shape and properties of mode vtail_rock-a identified in C1d.

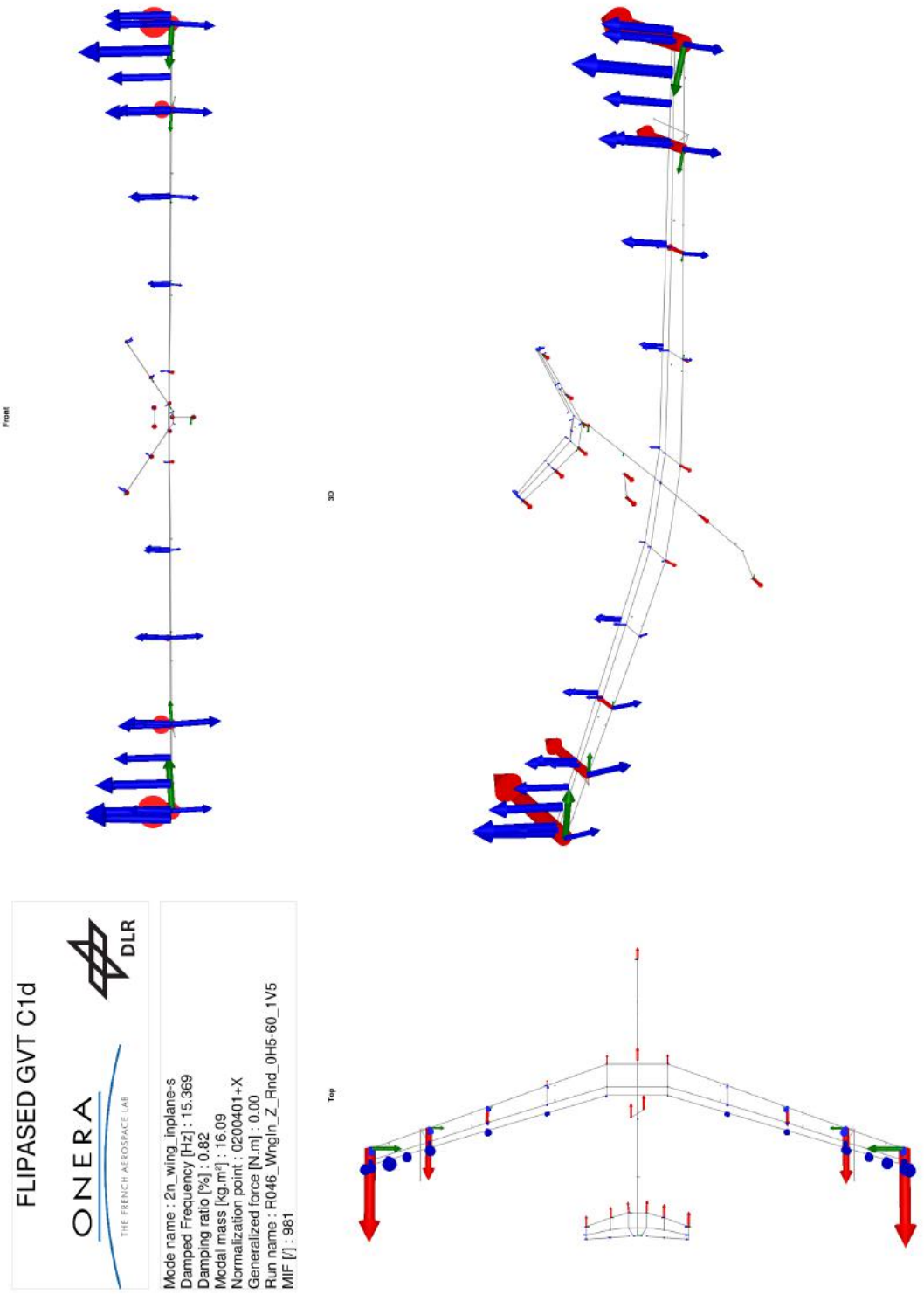

Figure B.56: Mode shape and properties of mode 2n_wing_inplane-s identified in C1d.

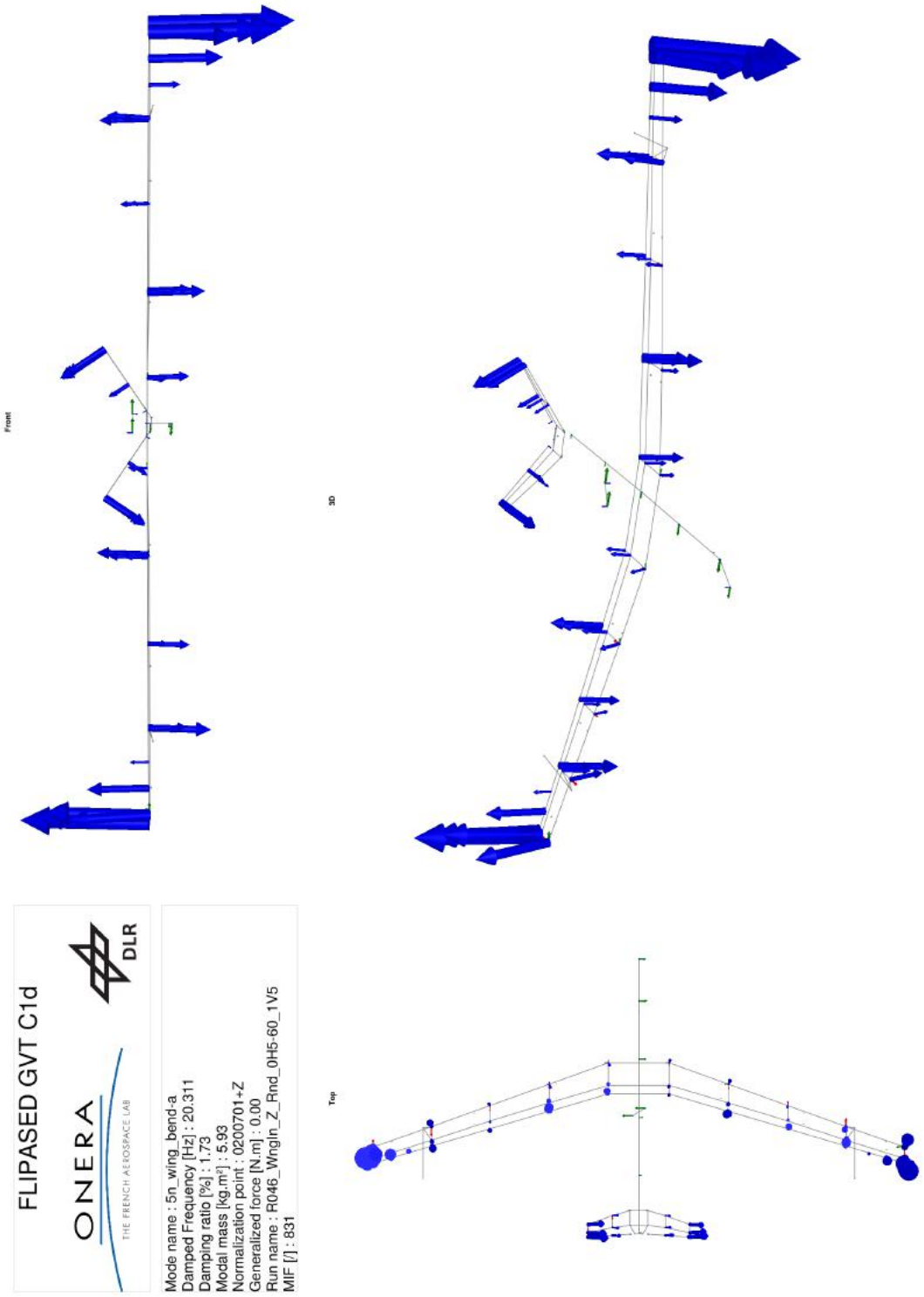

Figure B.57: Mode shape and properties of mode 5n_wing_bend-a identified in C1d.

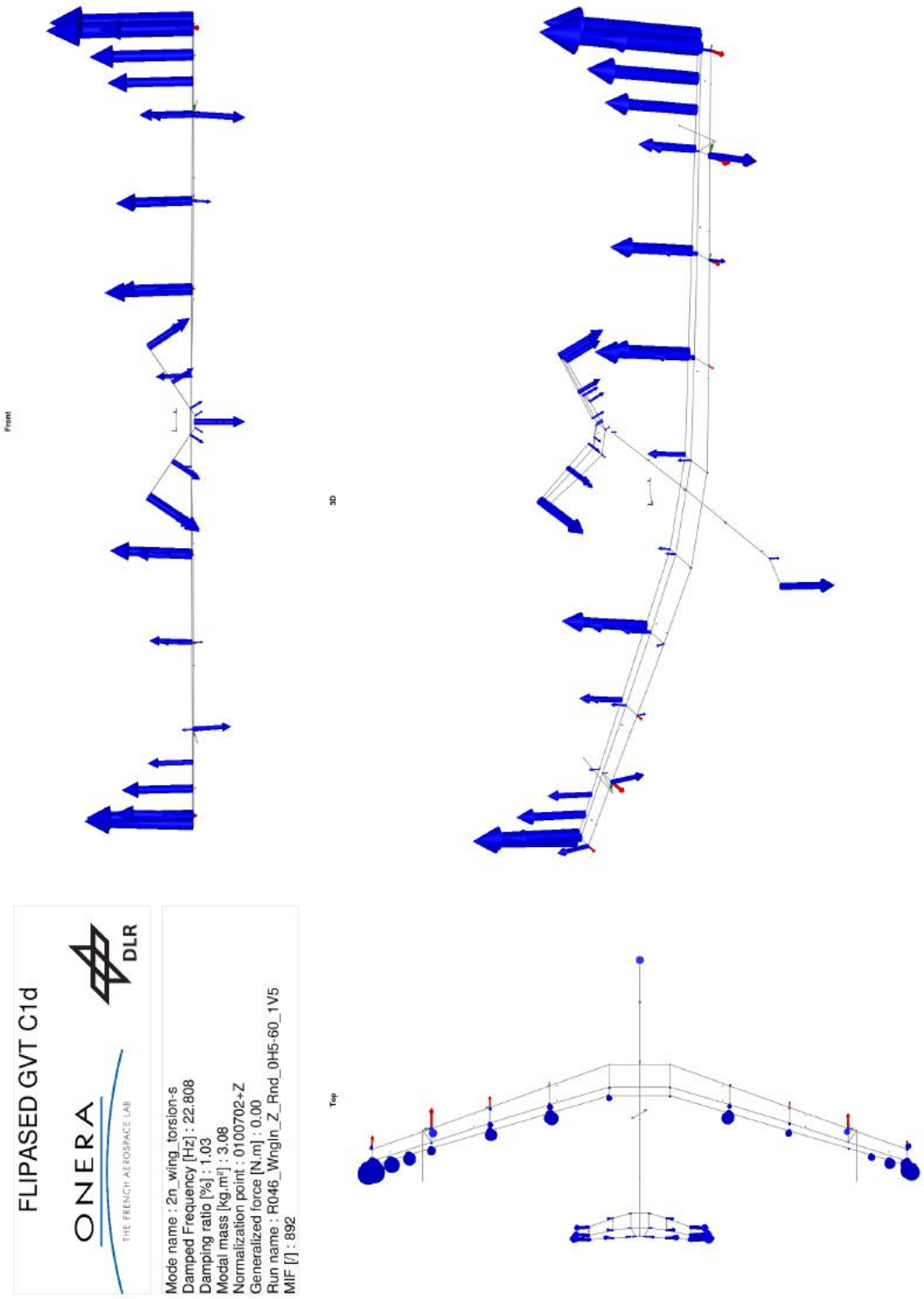

Figure B.58: Mode shape and properties of mode 2n_wing_torsion-s identified in C1d.

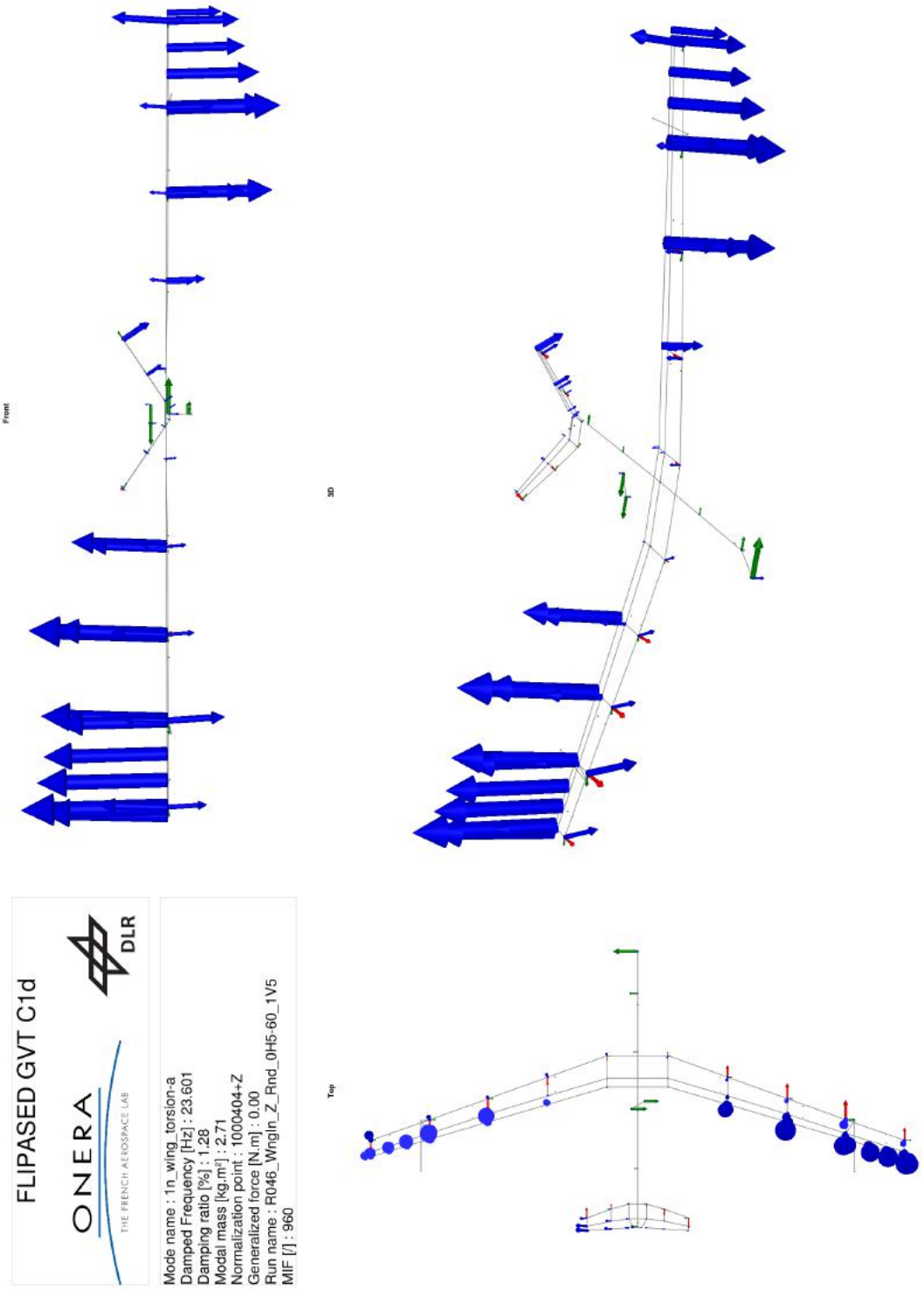

Figure B.59: Mode shape and properties of mode 1n_wing_torsion-a identified in C1d.

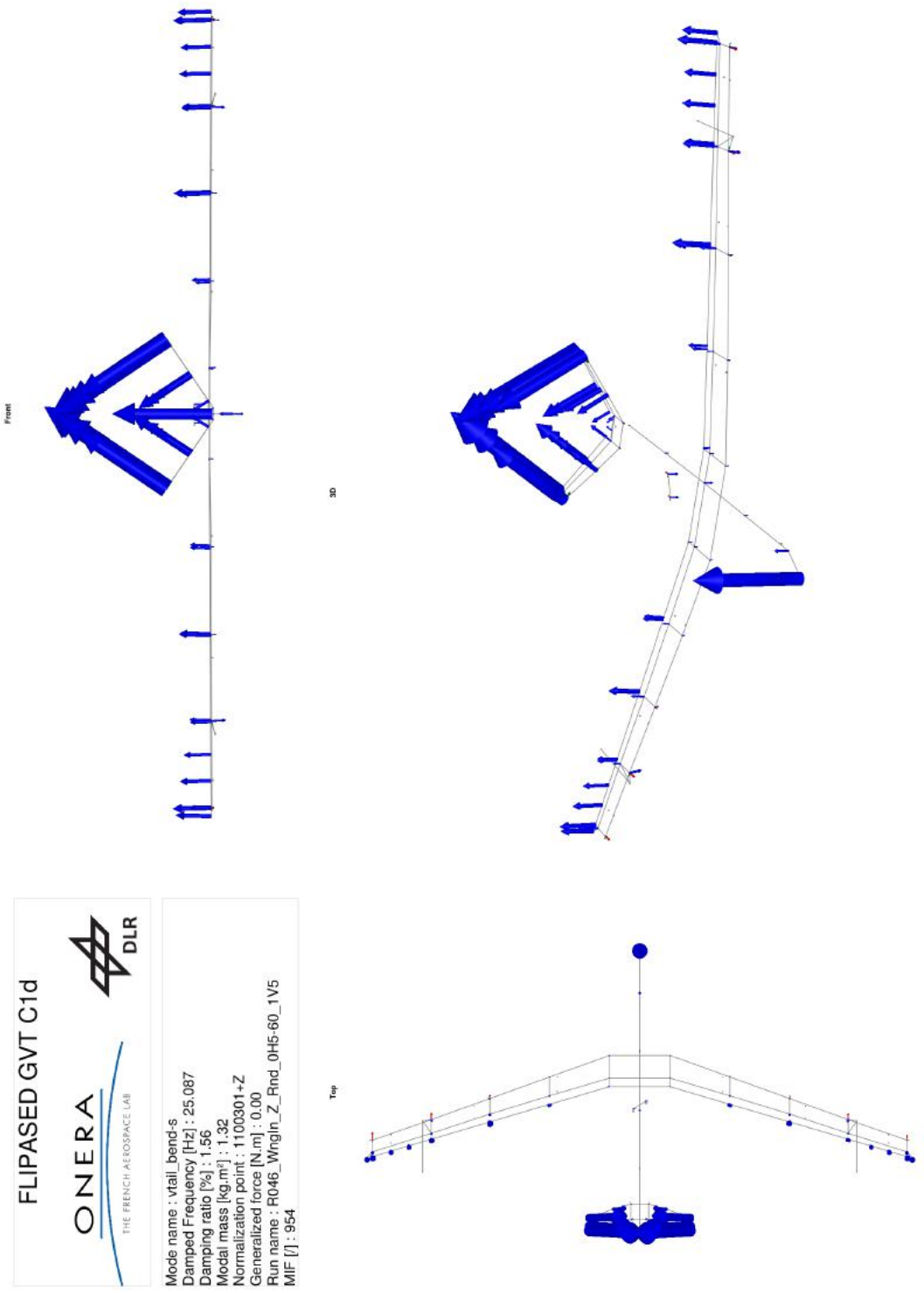

Figure B.60: Mode shape and properties of mode vtail_bend-s identified in C1d.

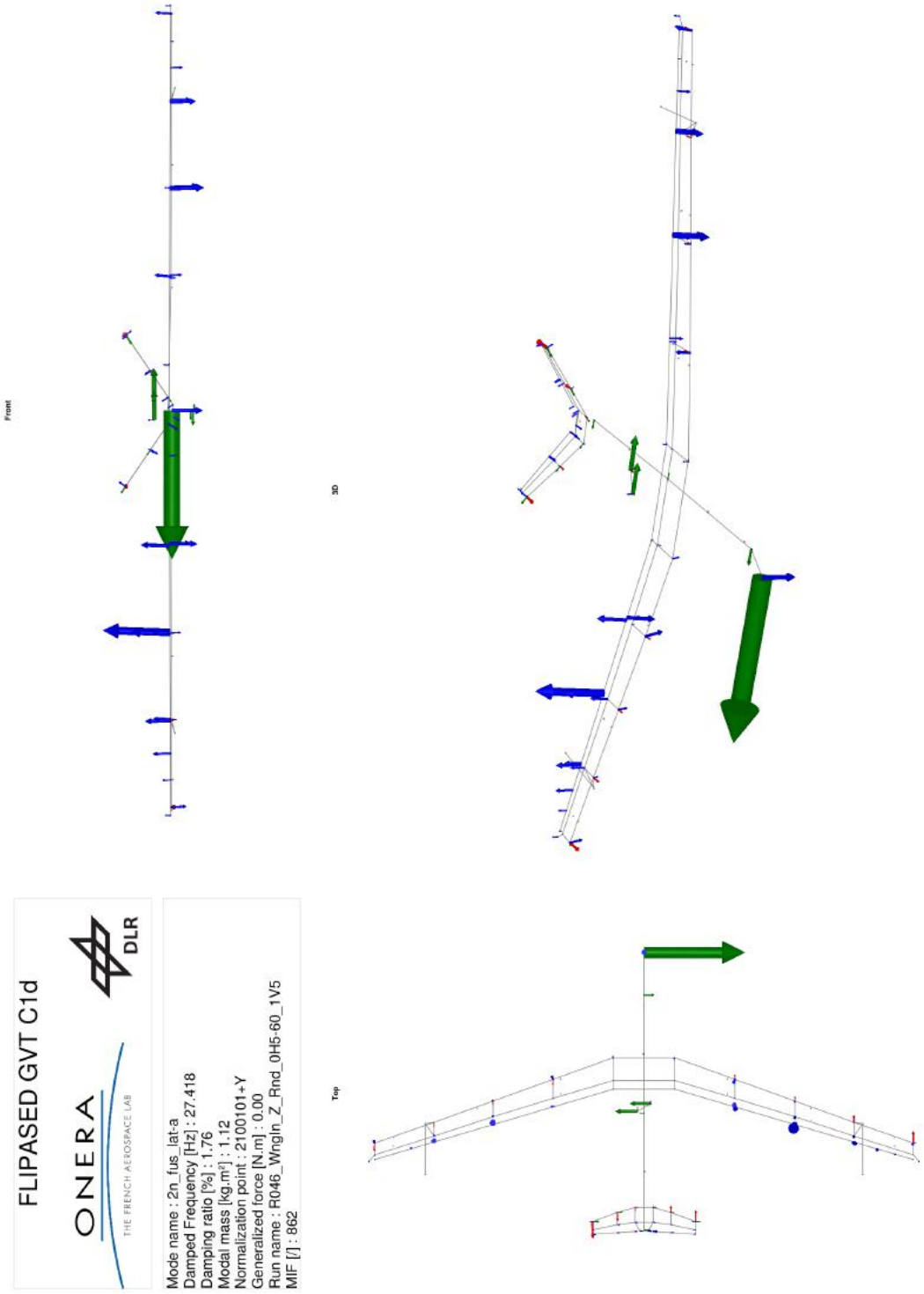

Figure B.61: Mode shape and properties of mode 2n_fus_lat-a identified in C1d.

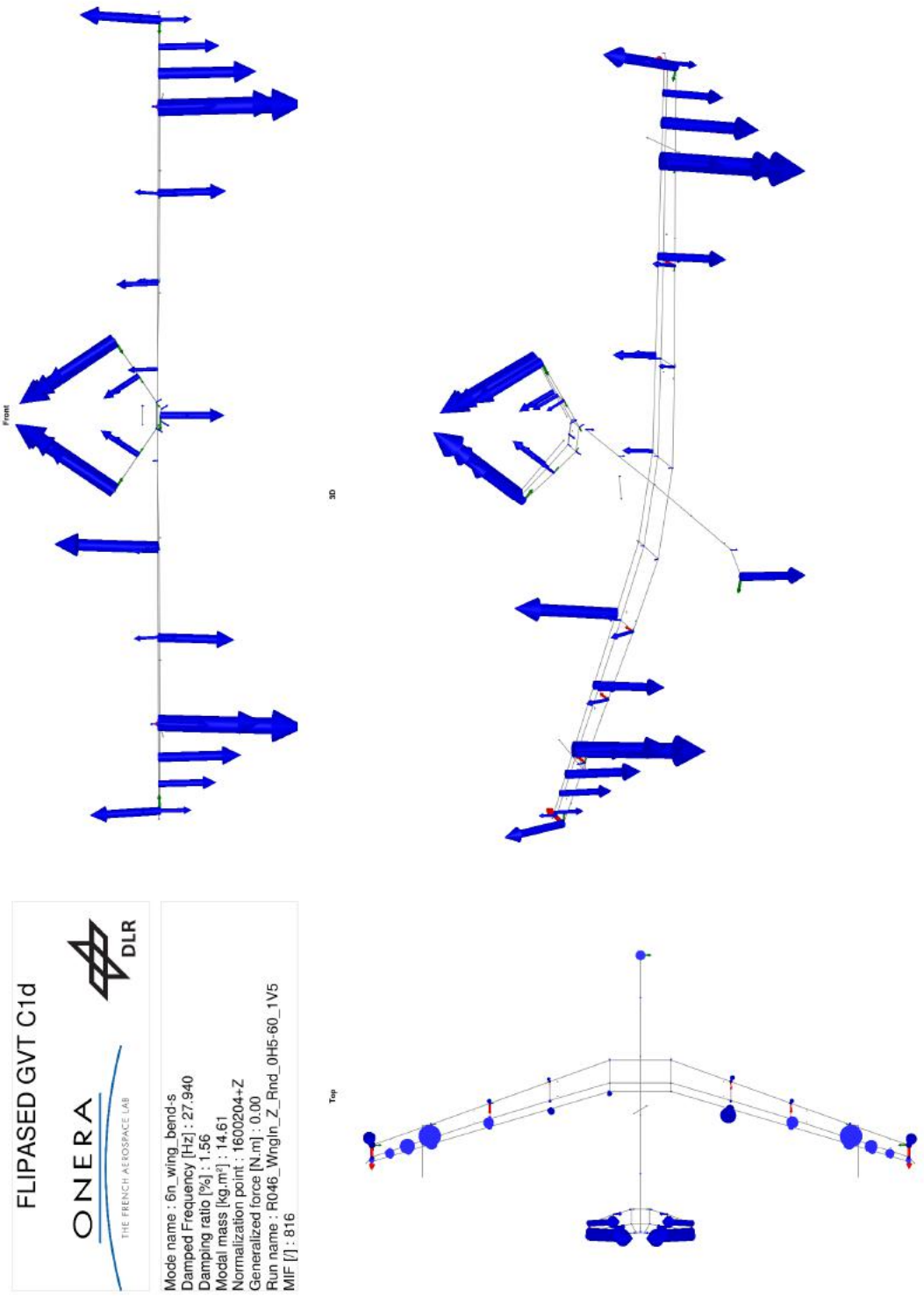

Figure B.62: Mode shape and properties of mode 6n_wing_bend-s identified in C1d.

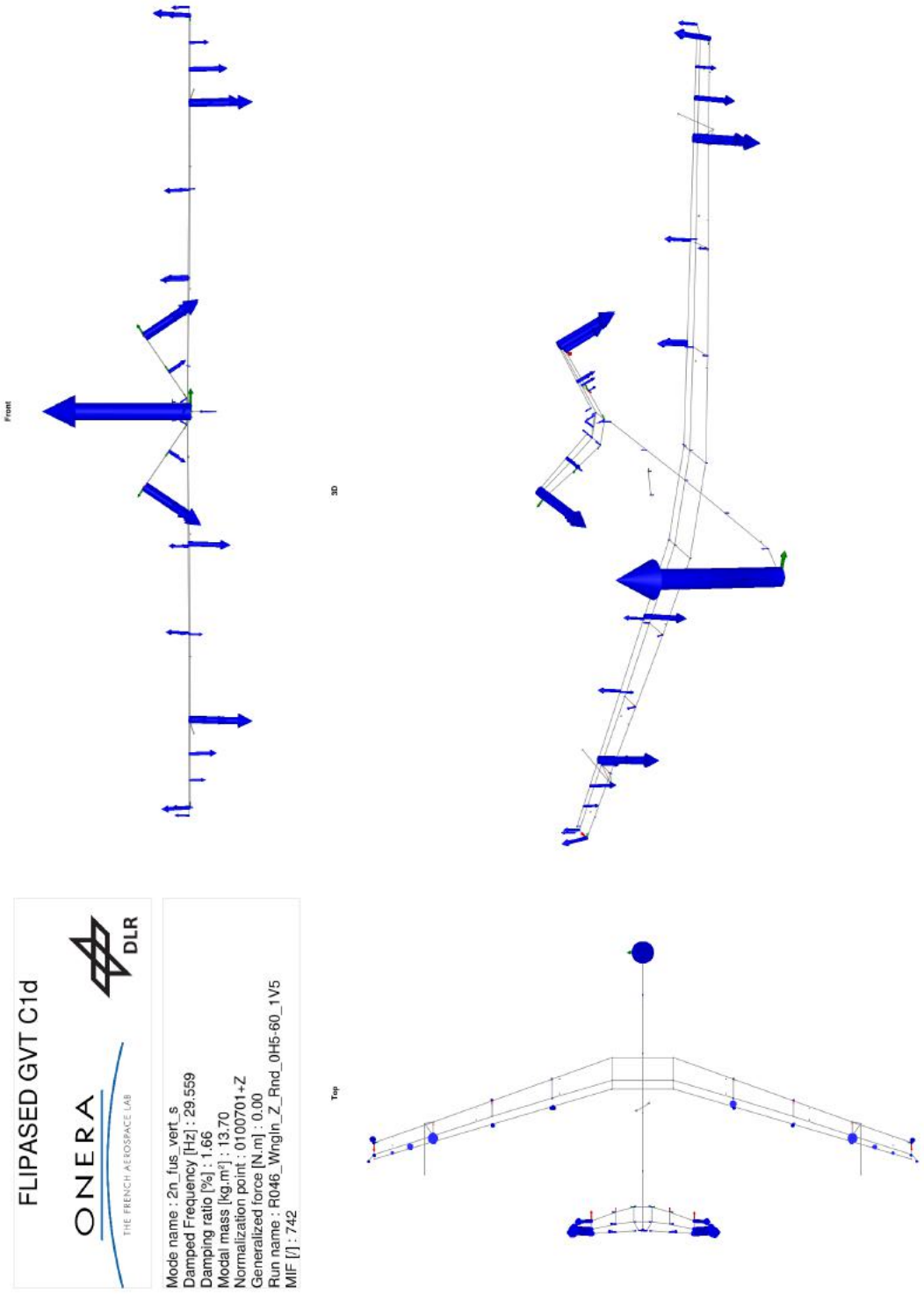

Figure B.63: Mode shape and properties of mode 2n_fus_vert_s identified in C1d.

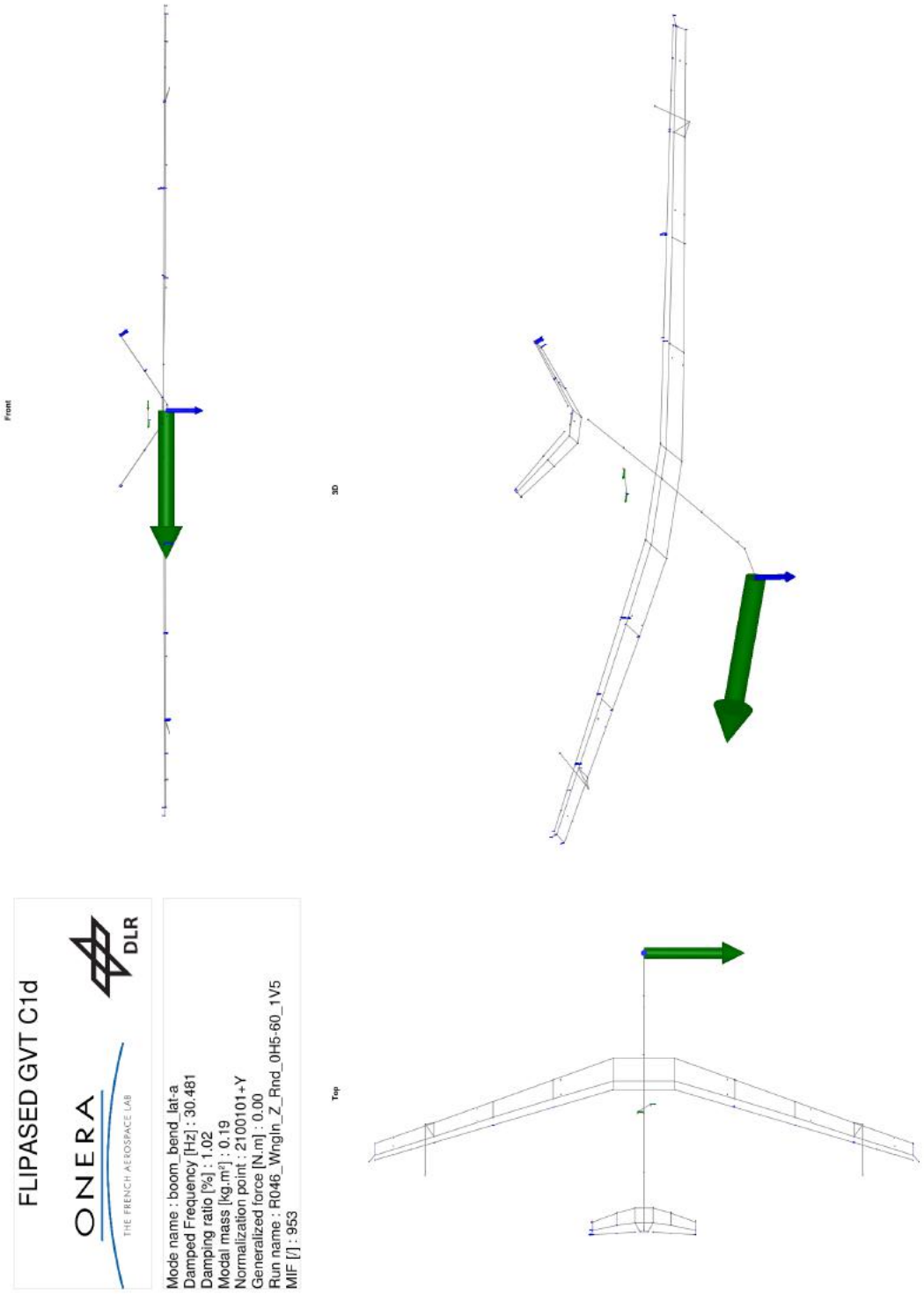

Figure B.64: Mode shape and properties of mode boom_bend_lat-a identified in C1d.

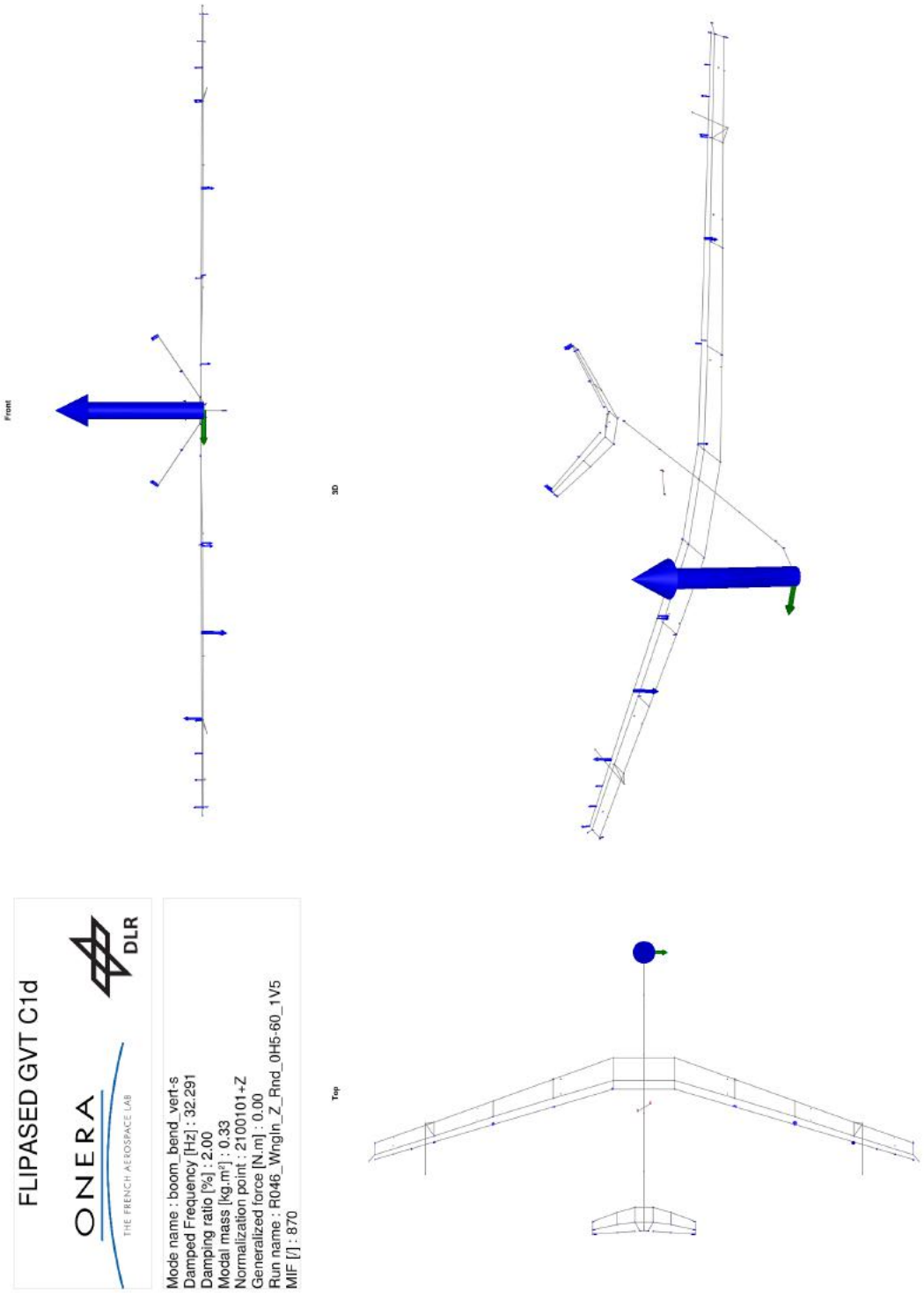

Figure B.65: Mode shape and properties of mode boom_bend_vert-s identified in C1d.

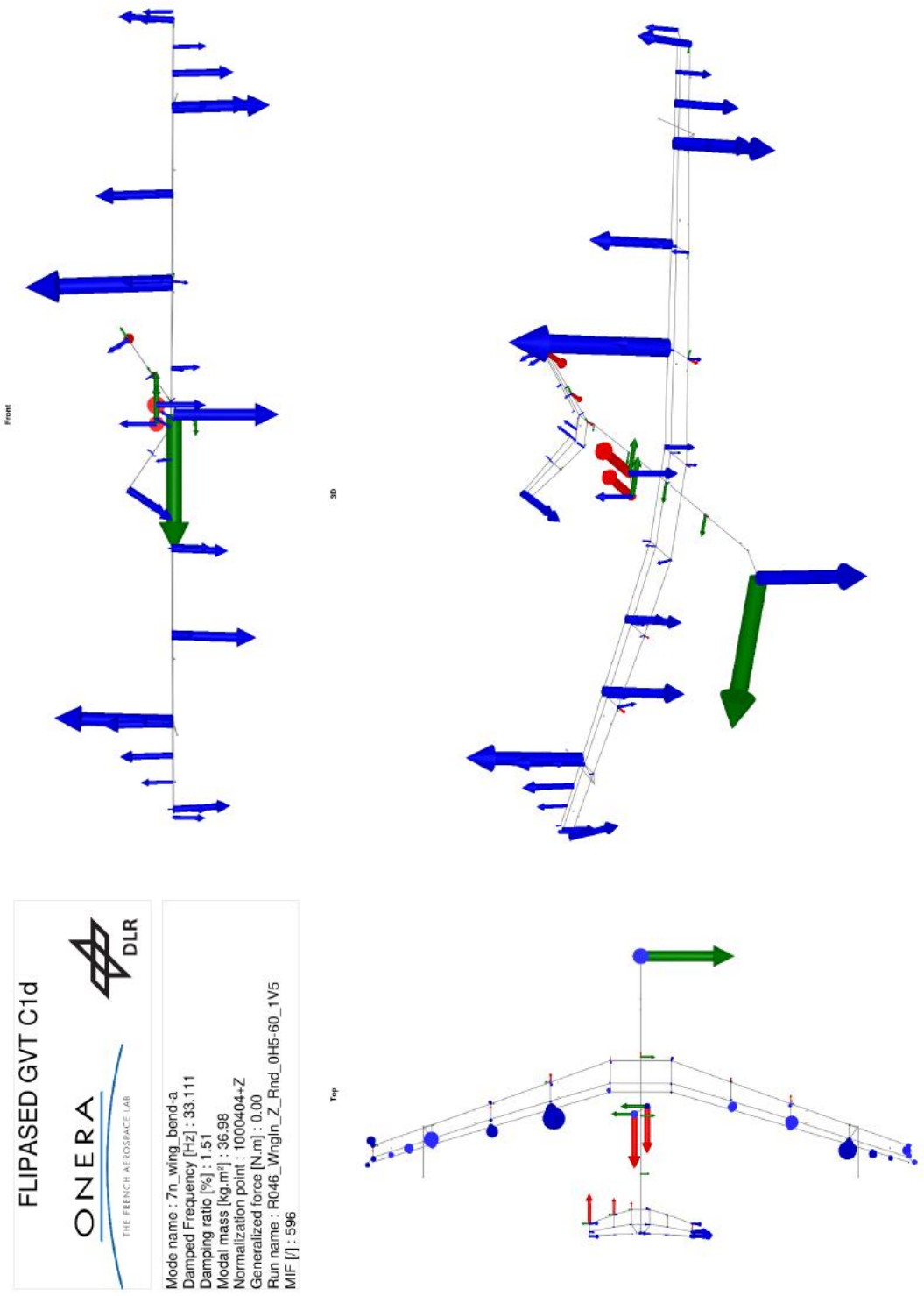

Figure B.66: Mode shape and properties of mode 7n_wing_bend-a identified in C1d.

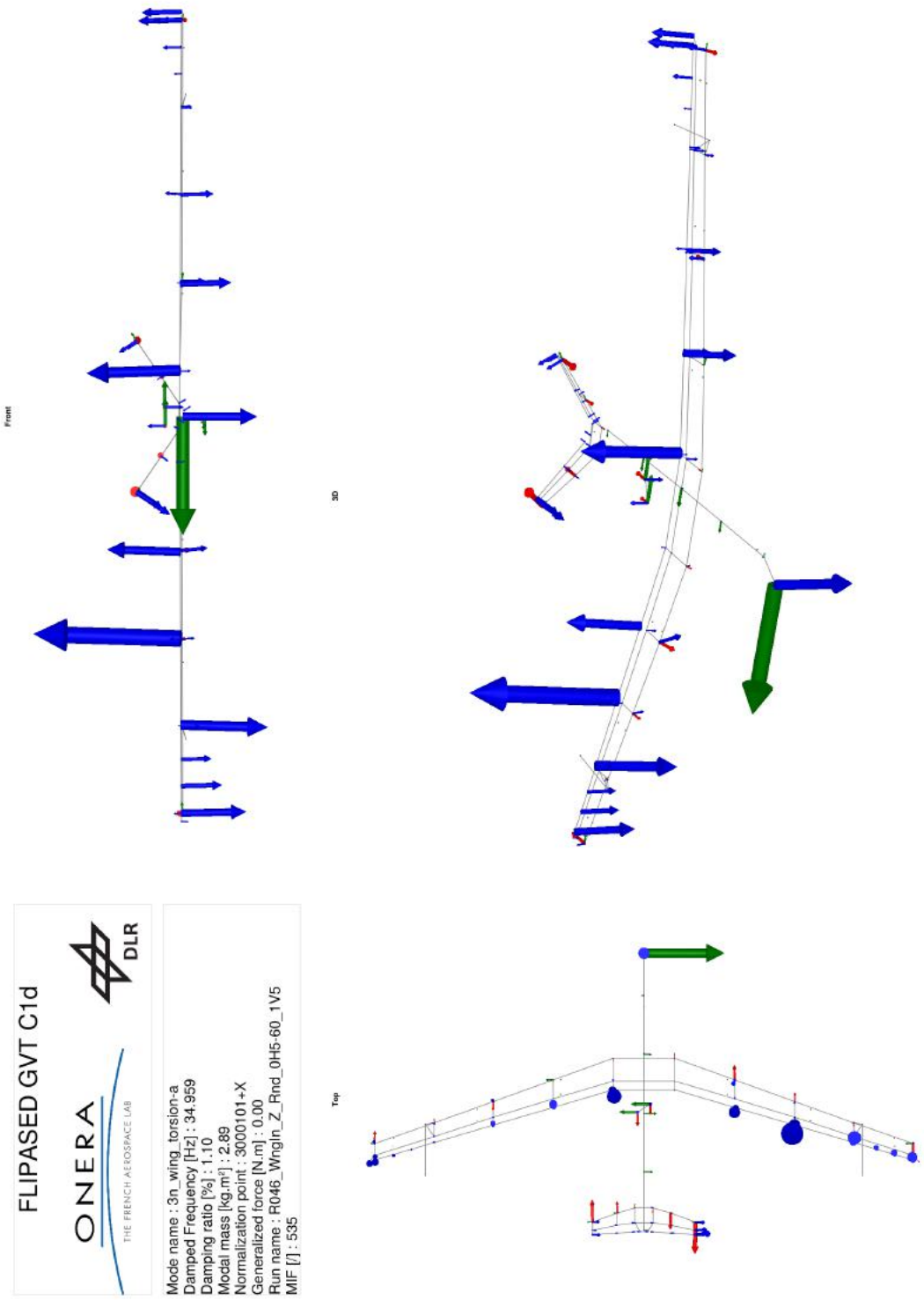

Figure B.67: Mode shape and properties of mode 3n_wing_torsion-a identified in C1d.